Mechatronics Examples For Teaching Modeling, Dynamics, and Control

by

Yi Xie

Submitted to the Department of Electrical Engineering and Computer Science
in partial fulfillment of the requirements for the degrees of

Bachelor of Science in Electrical Science and Engineering

and

Master of Engineering in Electrical Engineering and Computer Science

at the

MASSACHUSETTS INSTITUTE OF TECHNOLOGY

May 2003

Author . . . .
Department of Electrical Engineering and Computer Science
May 21, 2003

Certified by. . . . .
David L. Trumper
Associate Professor
Thesis Supervisor

Accepted by . . . .
Arthur C. Smith
Chairman, Department Committee on Graduate Students

Mechatronics Examples For Teaching Modeling, Dynamics, and Control

by

Yi Xie

Submitted to the Department of Electrical Engineering and Computer Science
on May 21, 2003, in partial fulfillment of the
requirements for the degrees of
Bachelor of Science in Electrical Science and Engineering
and
Master of Engineering in Electrical Engineering and Computer Science

Abstract

This thesis presents the development of a single-axis magnetic suspension. The intention is to use this system as a classroom demo for an introductory course on modeling, dynamics, and control. We solve this classic nonlinear controls problem with feedback linearization; the main advantage with this technique is operating point independency. However, it is highly sensitive to modeling errors and unpredicted plant behavior. We overcome these barriers by using a model based on both theory and experimentally determined behavior. This paper details the theory, modeling, and implementation, concluding with performance analysis.

Thesis Supervisor: David L. Trumper
Title: Associate Professor

Acknowledgments

There are a number of people I would like to thank for helping me through this project. First, I would like to thank Professor David Trumper. He continually pushed me to do better work and set a high standard. His expertise in both electrical and mechanical engineering has been an inspiration. In a short period of time, I have learned a great deal about engineering, teaching, and research from him. Although difficult at times, the experience has ultimately been a rewarding one.

My lab mates in the Precision Motion Control Laboratory have been a source of guidance. I want to thank Joe Cattell for helping me with adjusting to the research environment and getting up to speed. Katie Lillienkamp was always a source of assistance ranging from learning basic concepts to showing me where to find the parts I was looking for. It was a pleasure working with Xiaodong Lu, Vijay Shilpiekandula, and Justin Verdirame as teaching assistants. Discussions with them and the students in the class solidified my understanding of modeling, dynamics, and control, and made my graduate experience more enjoyable. In a lab full of mechanical engineers, Rick Montesante was always there to discuss circuits with me and help sort out my confusion. Our conversations always brought on a new understanding in my research. I also want thank Dave Otten for sharing his experiences and taking time to work through my problems. Martin Byl was also a tremendous source of knowledge, particularly with LaTex. Danny Hilton was an unexpected find as he started out as just one of the 2.003 students but ended up doing a lot of the machining and handiwork for me. I would not have finished on time without him. Last but not least, there was Maggie Beucler who made my life easier by helping to place orders, get reimbursements, and ease the process of anything logistical in nature.

Finally, I send out my dearest thanks to family and friends. Without them, I am not sure I would have made it through this year in one piece. They have been supportive through my ups and downs, and gave me the confidence I needed to continue. Undoubtedly, there were times of frustration, and it was to them that I looked for comfort. I am eternally grateful for the love and encouragement from my parents, Da Gang and Yao, and brothers, Li and Scott - particularly my older brother Li, who always put things in perspective for me when times got tough.

Contents

List of Figures

List of Tables

Chapter 1

Introduction

1.1 Background

This thesis presents the development of a single-axis magnetic suspension system for use as a classroom demonstration illustrating nonlinear control. It is based on a design originally developed by Professor David Trumper with his students at UNC Charlotte as documented in [10] and [11]. What at first glance appears to be a simple classroom demo, shown in Figure 1-1, actually involves many subtle complexities. Developing a working prototype requires command of a broad range of control techniques from modeling and analysis to design. Much research on control techniques has been tested on ball suspension systems. Namerikawa et al. evaluate the effectiveness of a generalized H_∞ control attenuating initial state uncertainties using a magnetic suspension system much like the one presented in this thesis [6]. Trumper et al. compared the performance of a nonlinear and linear controller in [10]. A good reference on magnetic suspension control techniques can be found in [9, chap. 3]. The techniques presented extend to larger systems used in robotics, aircraft, disk drives, and much more. Maglev trains and magnetic bearings are two of the most important related applications.

Maglev trains have received much attention in recent years. The first commercial maglev train made its appearance in China in December 2000. Both Japan and Germany are developing technologies that are in the testing stages. Much faster than

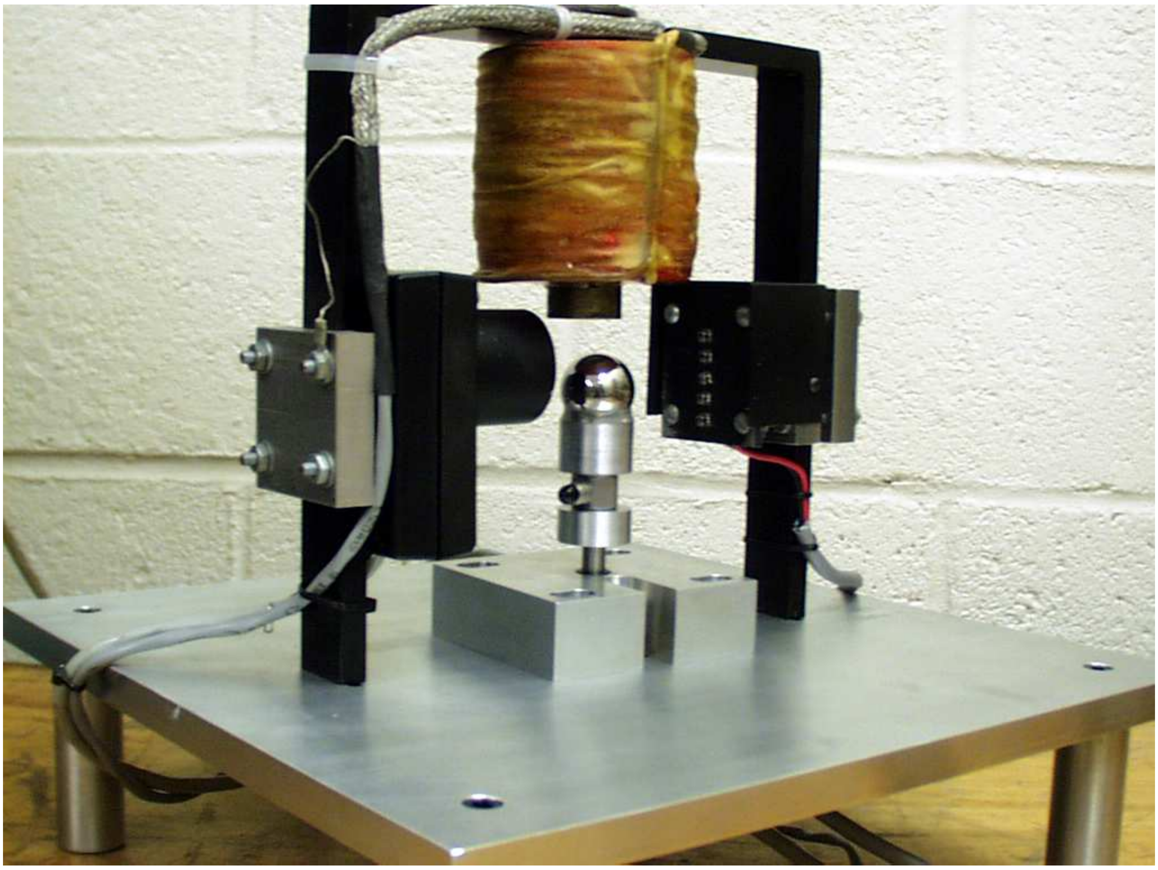

Figure 1-1: The maglev demo hardware.

conventional trains, maglev trains could offer an alternative to air travel. The trains float over guide rails virtually eliminating friction, which allows them to reach speeds of 350 mph or greater without the limitations of wheels. Such advantages could allow this technology to revolutionize transportation. This area of research has long been around but only recently have the costs become comparable to other technologies such that it is no longer cost prohibitive.

Magnetic bearings have a number of advantages over conventional roller or fluid bearings. High circumferential speeds at high loads make them ideal for use in rotating machinery. Electromagnets positioned about a magnetic rotor support the rotating shaft, thereby eliminating contact, wear, and the need for lubricants. The lack of friction means very little loss and virtually unlimited life expectancy. These factors permit operation in extreme environments such as high temperatures, low temperatures, and vacuum. They are used in high vacuum pumps, milling and grinding spindles, gyroscopes for space, and much more.

This thesis project demonstrates key issues by focusing on a single degree of freedom magnetic suspension system. It illustrates the issues associated with nonlinearity, instability, and robustness of design. Tradeoffs exist and we need to understand which are the important factors to be designing for, and where there is room for error. Some performance measures we will discuss are disturbance rejection, overshoot, damping, robustness to modeling error and unknown plant characteristics, and of course overall stability. Any study of control systems should start with these fundamentals. Students can learn a great deal from a relatively simple example, and such research forms a good basis for further work in mechatronics and controls.

1.2 Overview

The levitation system consists of a position sensor, actuator, and controller. Figure 1-2 shows a conceptual schematic of this system, and Figure 1-3 is a photograph of the actual hardware. The actuator provides the force necessary to counteract gravity and to stabilize the equilibrium. It is an electromagnet whose field strength depends on

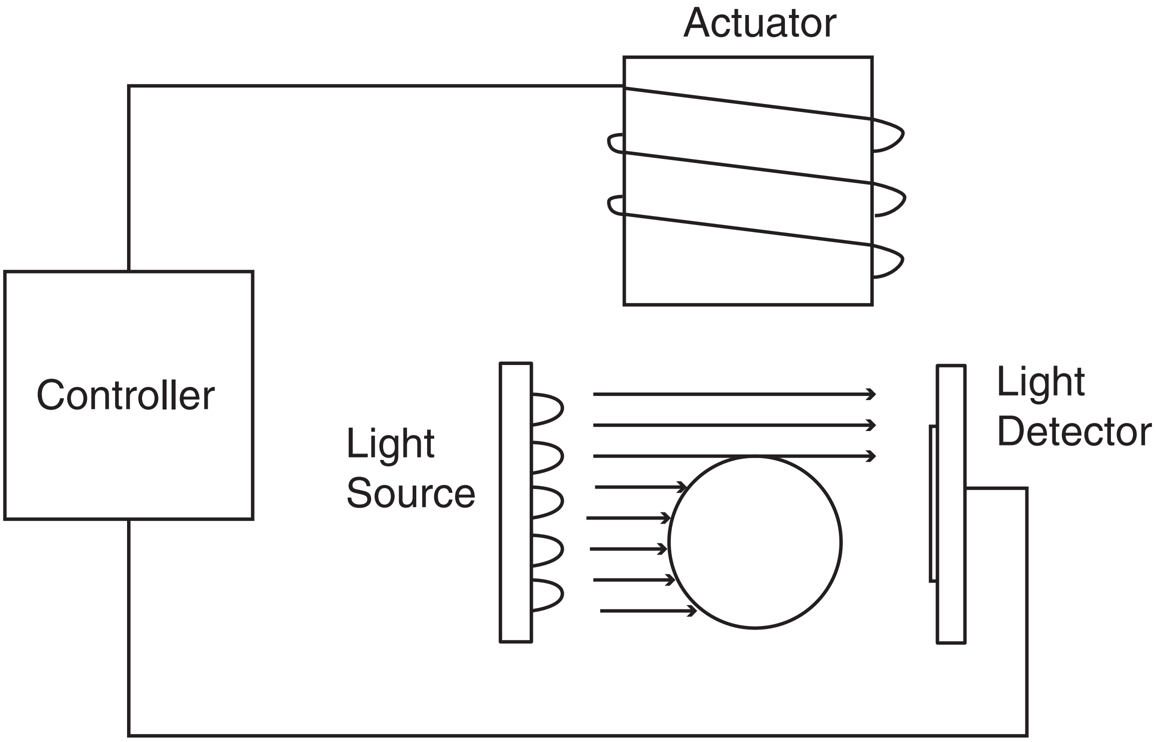

Figure 1-2: System schematic consisting of actuator, position sensor, and controller.

the amount of current flowing in the coil. We can thus control the magnetic force by adjusting this current. The actuator exerts force by pulling on and releasing the ball, giving us active control over the vertical axis. The equilibrium is only passively stabilized in the lateral directions via the field gradient. A suspension system also requires a mechanism for sensing the position of the object, a ball in this case. Here, we use an optical approach with a light source and corresponding sensor. As the ball moves up and down, the amount of light detected changes accordingly. The controller looks at the position of the ball and compares it to the reference input position, adjusting the force as needed. The relationship between force, current, and air gap is nonlinear. We use a micrometer fixture to measure this relationship as shown in the picture of Figure 1-4 and the layout of Figure 1-5. Traditionally, these equations are linearized about an operating point. Instead, we use feedback linearization, which overcomes the operating point dependency and allows the suspension to work over a wide range of air gaps. This thesis details the design and implementation of the the

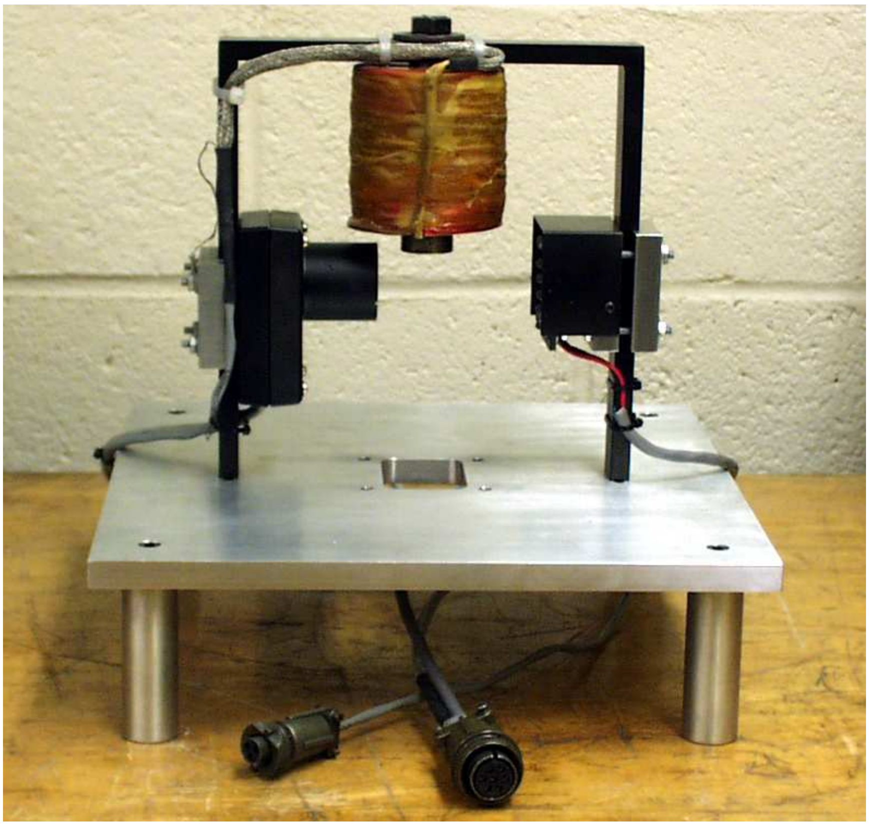

Figure 1-3: Photograph of physical structure. Controller not shown.

position sensor, actuator, controller, and associated interface electronics.

Aside from feedback linearization, there are other nonlinear control techniques worth mentioning but are beyond the scope of this paper. Adaptive gain scheduling is one such technique. Essentially, the system of interest is linearized about several operating points and a separate controller is designed for each. Then, a gain scheduler is designed to interpolate over the controllers. Kadmiry et al. use a fuzzy gain scheduling approach to helicopter control, stabilizing attitude angles (pitch, roll, yaw) over a large range [3]. Fuzzy gain scheduling falls in a large class of adaptive controllers where unpredictable environments and dynamics that are multi-variable and sometimes unknown require an adaptive solution. There is much interest in this area of controls and literature is abundant. Krupadanam et al. [4] and Corban et al. [1] offer alternative approaches to adaptive control.

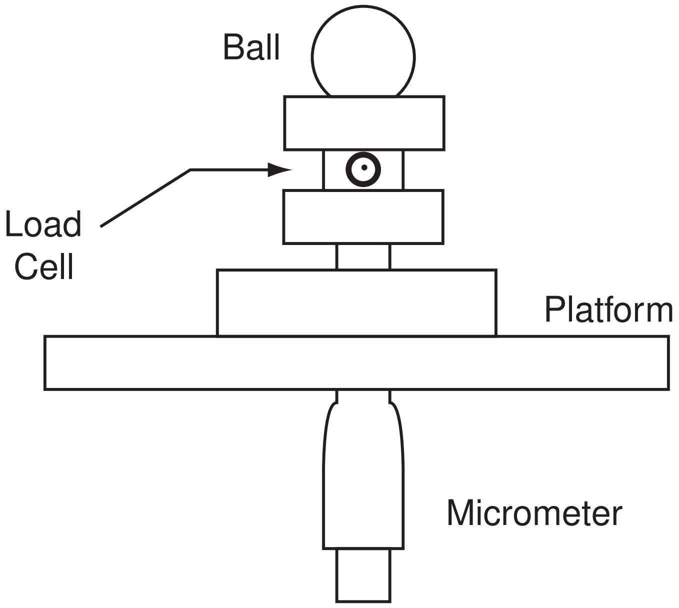

Figure 1-4: Drawing of the micrometer fixture.

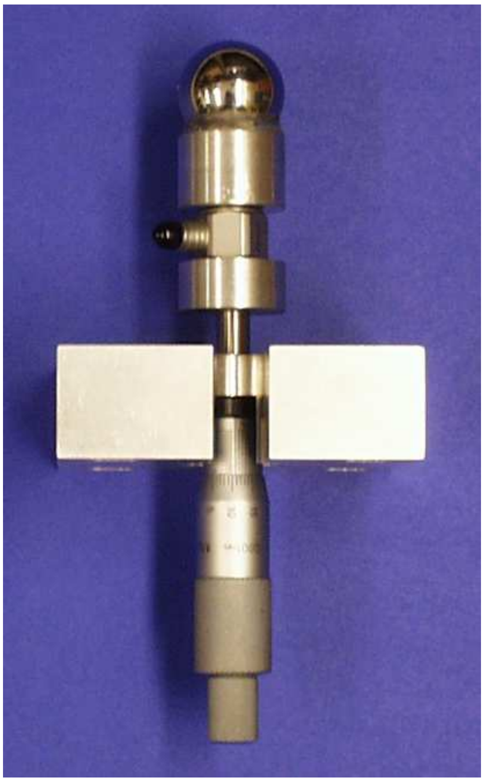

Figure 1-5: Photograph of the micrometer fixture.

1.3 Organization

In Chapter 2, we develop a method for creating a model, first measuring the force, current, and air gap relationship for this structure. We base our model on theory and then adjust it to fit experimental data. From there, Chapter 3 outlines the circuits used in this system. They consist of the linear amplifier, light source, and transresistance amplifier. Chapter 4 formalizes some nonlinear compensation techniques and details the controller used for this project. Chapter 5 summarizes the results and analyzes some performance measures. Finally, conclusions and suggestions for further work are discussed in Chapter 6.

Chapter 2

Circuit Implementation

2.1 Introduction

The magnetic suspension system is depicted schematically in Figure 2-1. It consists of a position sensor, linear amplifier, controller, and actuator coil. The position sensor uses an array of light emitting diodes as the light source and a photodiode array to detect the light. A steel ball is suspended between the light source and detector. The photodiode array produces a current proportional to the amount of light detected, which in turn depends upon the position of the steel ball. The transresistance amplifier converts the photodiode current into a voltage representative of position, which the computer processes. Completing the loop, the linear amplifier takes a voltage control signal from the computer and produces a proportional current of $0 - 2$ A to drive the coil. There are 2200 turns in the coil, wrapped on a 1" steel core. A photograph of the actuator is shown in Figure 2-2. The computer consists of a PC, dSPACE board, and associated software to implement the controller (see Appendix E for vendor details). The force measurement device is a micrometer attached to a load cell with a steel ball glued onto the top, depicted in Figure 2-3. A photograph of the micrometer is shown in Figure 2-4. We use the micrometer fixture for both position sensor calibration and force-current relationship measurements. Instead of implementing directly on a PC as was done in an earlier versions, this version uses the dSPACE board in conjunction with a PC running Matlab and Simulink software.

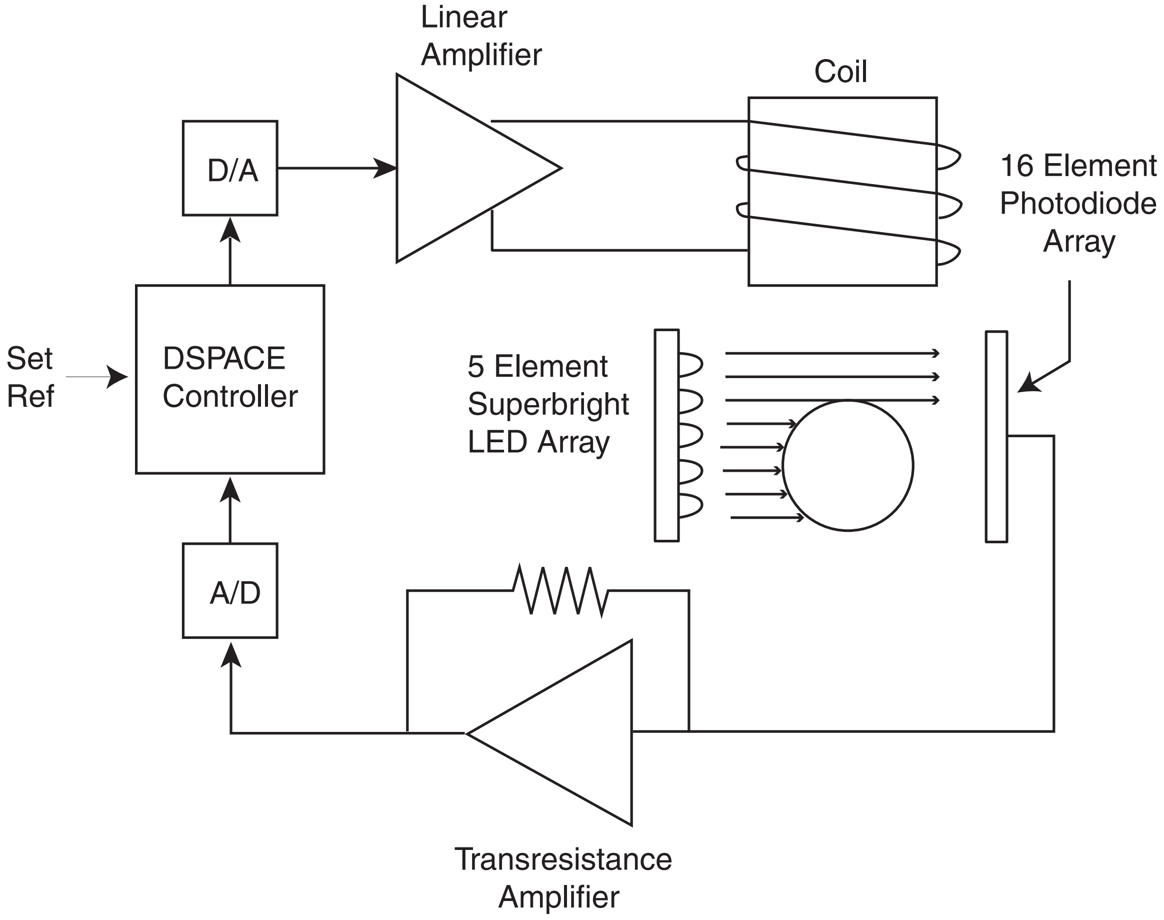

Figure 2-1: System control loop diagram.

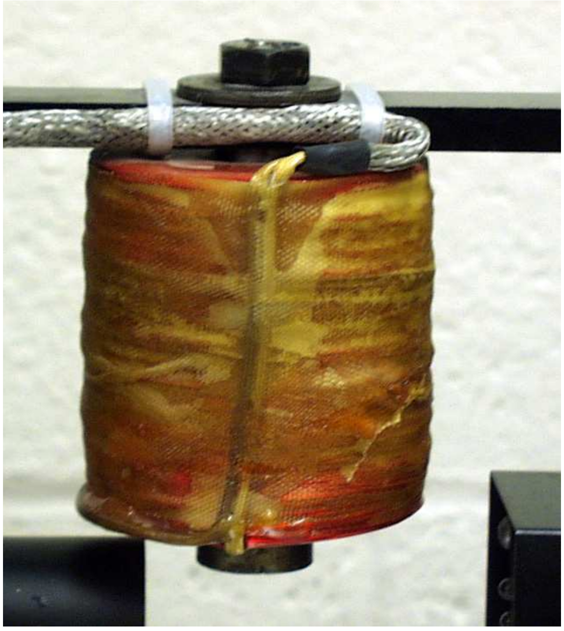

Figure 2-2: Actuator 2200 turn coil wrapped on a 1” steel core.

Simulink supports block diagrams, and associated software, converts them to code that is downloaded onto the dSPACE board. This approach is straightforward and easily supportable. Any changes to the controller are made directly to the block diagram and much easier to implement and debug than via direct programming.

2.2 Linear Amplifier

In the original design developed in [11], they used a switching amplifier of the hysteretic type. Switching amplifiers are usually used for their power efficiency: there is minimal static power consumption, and power is primarily lost in the switching. However, for a magnetic levitator used in a classroom demonstration, it is not necessary to use a switching amplifier: the switching adds complexity in the circuitry and causes undesired ripple in the output current as well as possible electrical interference with other subsystems. Finally, the single switch amplifier operated from a unipolar 40 V supply, and thus was incapable of supplying bipolar voltages to the coil, which resulted in a low negative slew rate. The maximum negative slew rate constrains

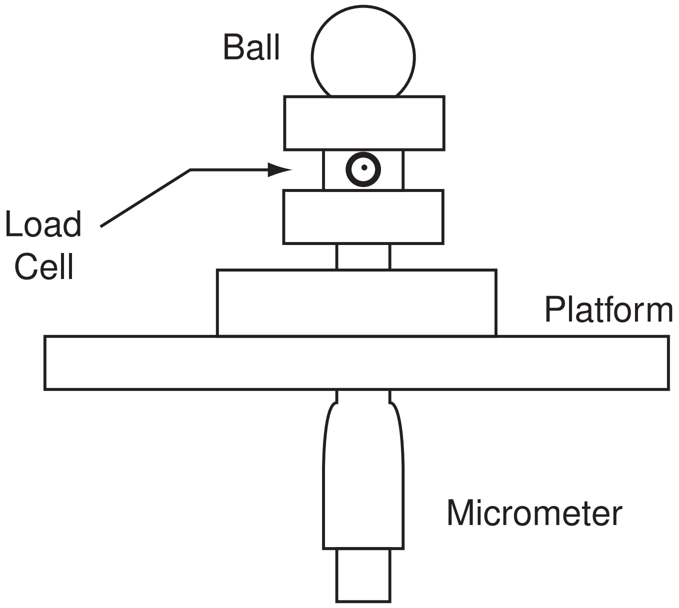

Figure 2-3: Drawing of the micrometer fixture.

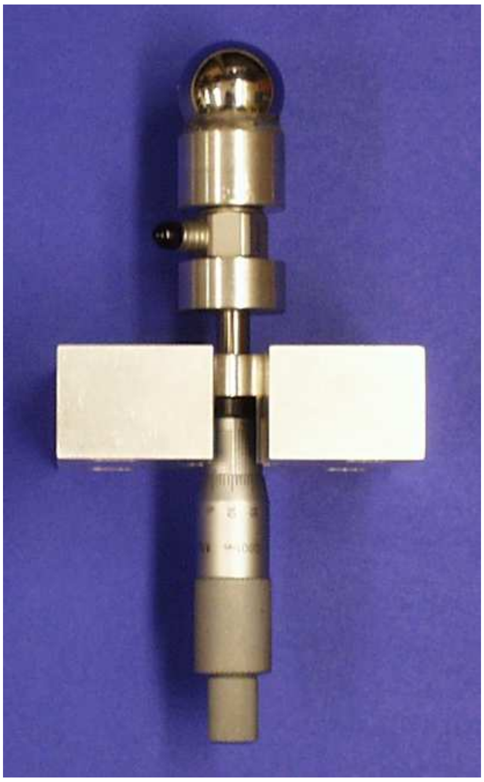

Figure 2-4: Photograph of the micrometer fixture.

the system particularly in the case where the steel ball is drawn close to the magnet. Only a small amount of current is needed near the pole face and therefore the current must be rapidly decreased or the ball will overshoot, leading to issues of instability in the loop. For good large-signal stability, we need bipolar voltage control, although the coil current is unipolar. Here, we will be using a linear amplifier to address these issues. This amplifier is based on a design developed by Prof. Trumper, and modified by Xiadong Lu, a Doctoral student in Prof. Trumper's lab.

The present design uses the linear amplifier shown in Figure 2-5. The amplifier is voltage controlled and this voltage gives the setpoint for the current in the inductor. The 1 Ω resistor works as a sense resistor and this voltage feeds back into the negative terminal of the operational amplifier. The op-amp adjusts the output voltage until the desired current is reached.

With the indicated components, this amplifier is capable of supplying +28 and −36 volts to the coil, which provides a sufficiently fast negative slew rate, set by the Zener diode breakdown voltage [12, p.200]. At the most basic level, inductors behave as

$$\frac{di_{coil}}{dt} = \frac{V}{L}. \tag{2.1}$$

The maximum negative slew rate is the fastest rate of change in the coil current. Therefore, with a fixed inductance, this slew rate is set by the maximum negative voltage across the coil, which is approximately the 36 V Zener breakdown voltage.

$$\frac{-di_{max}}{dt} = \frac{V_{zener}}{L} \tag{2.2}$$

The fly back circuitry is included to protect the electronics when the amplifier turns off. When the amplifier suddenly switches off, the drain voltage of the power FET could ramp up to very large values, potentially damaging the FET. To prevent this from happening, the Zener diode clamps the voltage, and current freewheels through the bipolar transistor and resistor circuitry. The drain voltage needs to rise above the 28 V for the current to start decreasing; this is apparent from equation (2.1). However, to protect the electronics we place a limit on how high this voltage can rise.

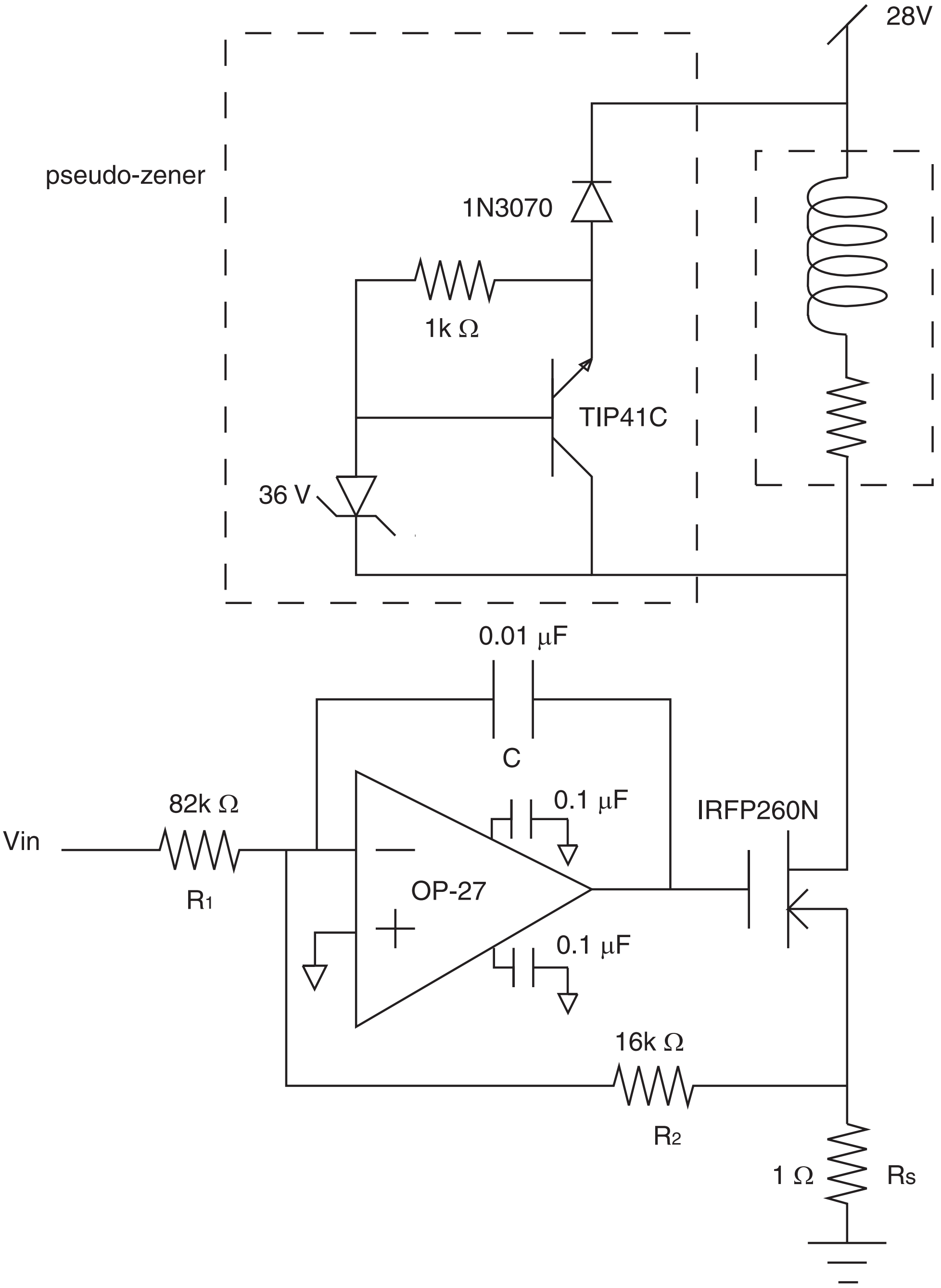

Figure 2-5: Linear amplifier circuit.

Once the drain voltage reaches 28 V + 36 V = 64 V, the zener diode breaks down and starts to conduct current in the reverse direction. Once this happens, the zener current turns on the power transistor, which then conducts the flyback current. The diode connected to the emitter and supply acts to prevent current flow through the fly back circuit during normal operation where the current should flow through the inductor path to ground. Otherwise, the power transistor base-emitter junction would break down; the reverse breakdown voltage at that junction is only about 6 V. The Zener voltage is chosen to be 28 V or higher, to avoid limiting of the +28/-36 V swing across the coil as previously mentioned.

Typically in a basic fly-back circuit, a diode is simply shunted across the inductor but this allows only 0.6 V drop. However, with the pseudo-Zener diode, we can have a maximum of +28/-36 V across the coil during stages of increasing/decreasing current. Thus, the performance improves on the negative slew rate over the switching amplifier design.

However, equation (2.1) and (2.2) do not take into account the coil resistance. We measured the coil resistance to be about 30 Ω. At best, the maximum positive voltage across the inductor is given by

$$V_L = V_{supply} - iR_L. \tag{2.3}$$

The OP-27 used in this design has a gain on the order of 10^6 (1.8 million) at low frequencies and a unity gain bandwidth of 10 MHz. This is far too much bandwidth for the application at hand; forcing crossover at 1 kHz, which sufficiently exceeds the closed loop bandwidth, stabilizes the loop. We also get better noise rejection by forcing a crossover at 1 kHz. The closed loop is modeled in Figure 2-6 where the gate to source gain is approximately 1, (i.e. the FET acts as a follower). We want the magnitude of the loop transmission to equal 1 at 1kHz, and the loop transmission is given by

$$L.T. = \frac{-1}{R_2Cs}. \tag{2.4}$$

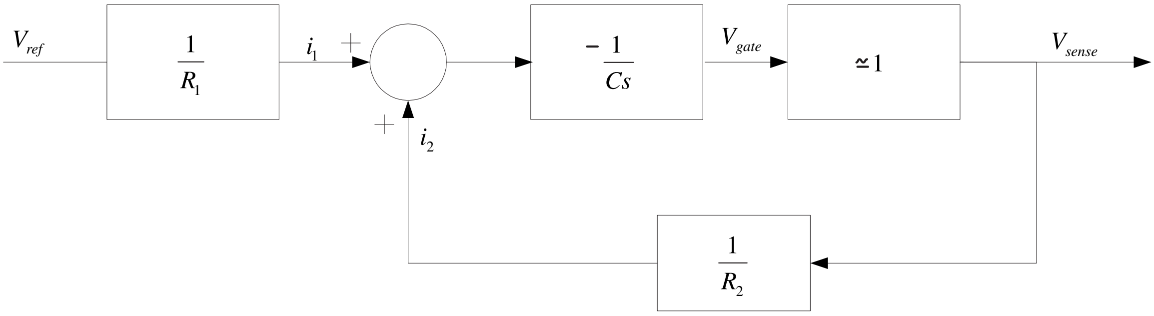

Figure 2-6: Block diagram for amplifier circuit.

We first choose a reasonable value for C - 0.01 μF. This then requires $R_2 = 16$ kΩ. The digital to analog converter in dSPACE outputs voltage in the range of ±10 V. Ideally, for the highest resolution the full range would be used to map to the current command. For simplicity, we only map the command to the positive side from 0-10 V. We found the maximum current needed is 2 A (more on current requirements in Chapter 4). Therefore, $0 - 10$ V maps to $0 - 2$ A or

$$\frac{V_{sense}}{V_{ref}} = \frac{1}{5}. \tag{2.5}$$

The resistor R_1 is thus constrained by the gain requirement at DC

$$\frac{V_{sense}}{V_{ref}} = \frac{R_2}{R_1(R_2Cs+1)} \Rightarrow D.C.gain = \frac{R_2}{R_1}, \tag{2.6}$$

which gives $R_1 = 5R_2 = 80$ kΩ. However, we encountered problems with stability using a gain of 1/5 in the amplifier, the reasons for which have yet to be worked out. The system appears to work fine with a unity gain in the amplifier so that is how it is currently implemented.

2.3 Position Sensor

We have designed the position sensor so that the amount of light detected by the sensor is proportional to the gap between the suspended steel ball and the magnetic coil. The ball will block some of the light from the light source, while some of the light will pass through. Ideally, when the gap is zero, no light passes into the detector because the ball has completely blocked the light coming from the source. On the receiving end, there is a red filter in front of the sensor to attenuate light coming from other sources, such as ambient lighting.

2.3.1 Light Source

Rather than using an incandescent source as in earlier implementations, light emitting diodes (LEDs) minimize ambient light interference and are more power efficient. The light source is a vertical array of 5 super bright light emitting diodes as shown in Figure 2-7. They emit light with a wavelength $\lambda = 628$ nm and output an intensity 8000 mcd (milliCandela) at 20 mA. MCD refers to the luminous intensity; 1 mcd produces 1 lumen per square meter at a 1-meter distance from the source. As a point of comparison, 1000 mcd produces roughly the same amount of light as a small 2-watt standard incandescent bulb. This construction, shown in Figure 2-7, provides a directed light source that produces a relatively linear function of gap length and shows repeatability.

The circuit representation of the light source is shown in Figure 2-8. Typical forward voltage drop across each diode is 2.2 V. The LEDs are rated for an absolute maximum peak forward current of 50 mA and maximum continuous forward current of 20 mA ($TA = 25°$ C). We chose $i = 15$ mA, which still produces a bright light source, while running the LEDs below their maximum rating. The resistor, R, sets the current in the LEDs. Assuming a 2.2 V drop for each LED, Kirchoff's voltage law yields the following equation:

$$15 \text{ V} = \text{iR} + 5(2.2 \text{ V}) \tag{2.7}$$

Solving for R with $i = 15$ mA, we get $R = 266\ \Omega$. The actual resistor used in the implementation is $R = 240\ \Omega$.

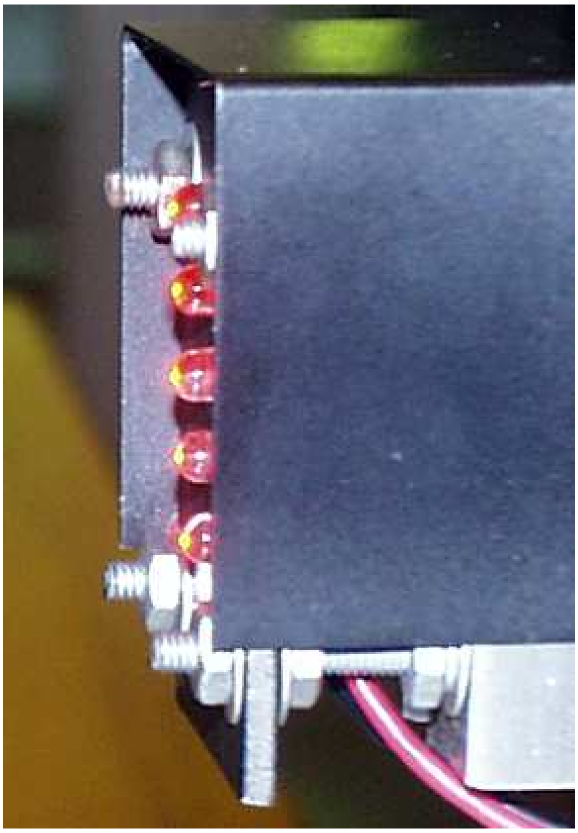

Figure 2-7: Light source.

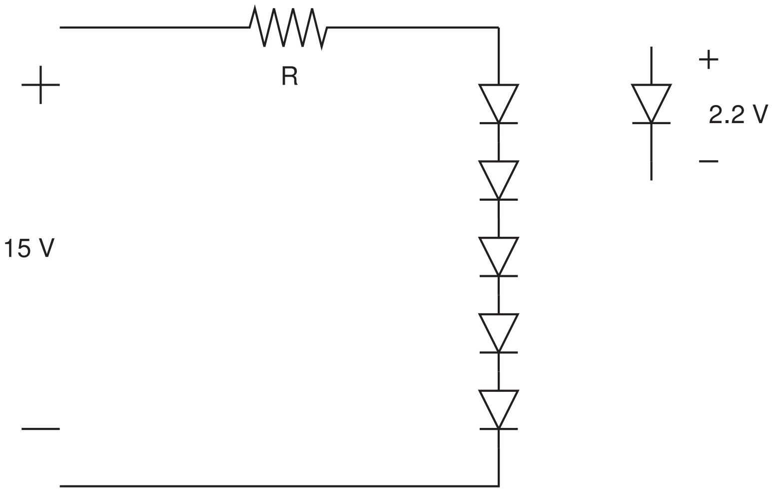

Figure 2-8: Circuit representation of light source.

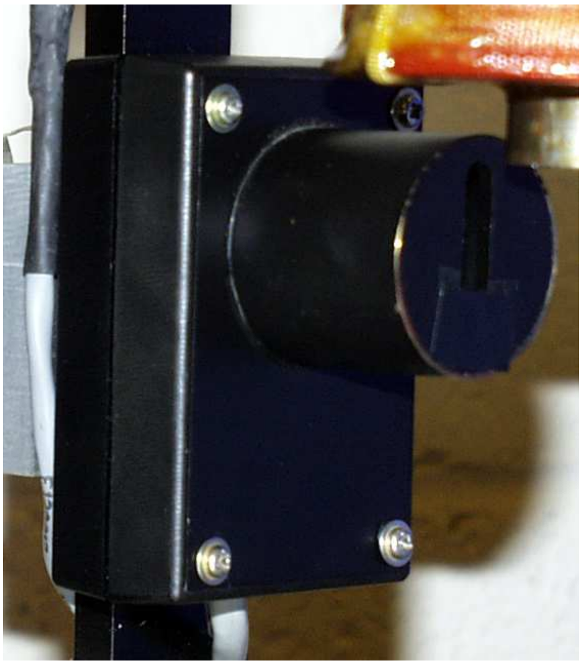

Figure 2-9: Light sensor with cover. The red filter is inside the cover.

2.3.2 Light Sensor

A sixteen-photodiode array manufactured by Hammamatsu senses the level of light that passes by the steel ball. There is an enclosure with a red filter in place directly over the array. We added another cover with a slit in it, allowing light to come in from only a small range of angles including the LED source (shown in Figure 2-9). This improves the stability of the position sensor by suppressing light from other sources. The slit can only be as long as the diameter of the ball because otherwise, light would pass through below the ball, giving a false reading in position. We assume any light passing through is passing above the ball, and that light is proportional to the gap length. In the best case, no current would flow from the photodiode array when the gap length is zero; however, stray ambient light and noise from the circuitry produces a small offset. The filter, cover, and slit are in place to reduce this offset.

We must convert current into a voltage for the photodiode-array to be useful because the computer requires a voltage input. To do this, we use a transresistance amplifier; the hardware implementation is shown in Figure 2-10 and the circuit dia-

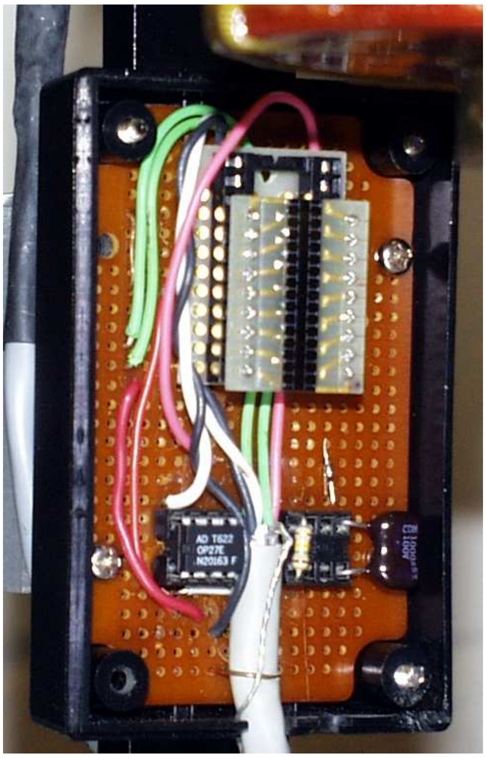

Figure 2-10: Light sensor circuit hardware.

gram in Figure 2-11. The current is summed from all 16 photodiodes at the virtual ground node of the transresistance amplifier. A resistor connected between the noninverting terminal and output terminal of the operational amplifier acts as a transducer to covert the current into a voltage through Ohm's Law (V = IR).

Again, the dSPACE converter, analog to digital this time, limits the range of meaningful input voltage, in the range of ±10 V. It is necessary to ensure the voltage readings from the light sensor remains in these limits, but also utilizes most of the available range. We experimentally found the maximum current reading from the photodiode, i.e. in the case where the ball is not suspended, $\mathrm{I}_{\mathrm{max}} = 6 \times 10^{-5}$ A . For the full 10 V swing, this would require $R = 166$ kΩ. To err on the safe side, we chose $R = 150$ kΩ.

A shunt capacitor C is added for low pass filtering, setting the bandwidth at 1 kHz. Solving for the impedance of the resistor/capacitor network gives the transfer

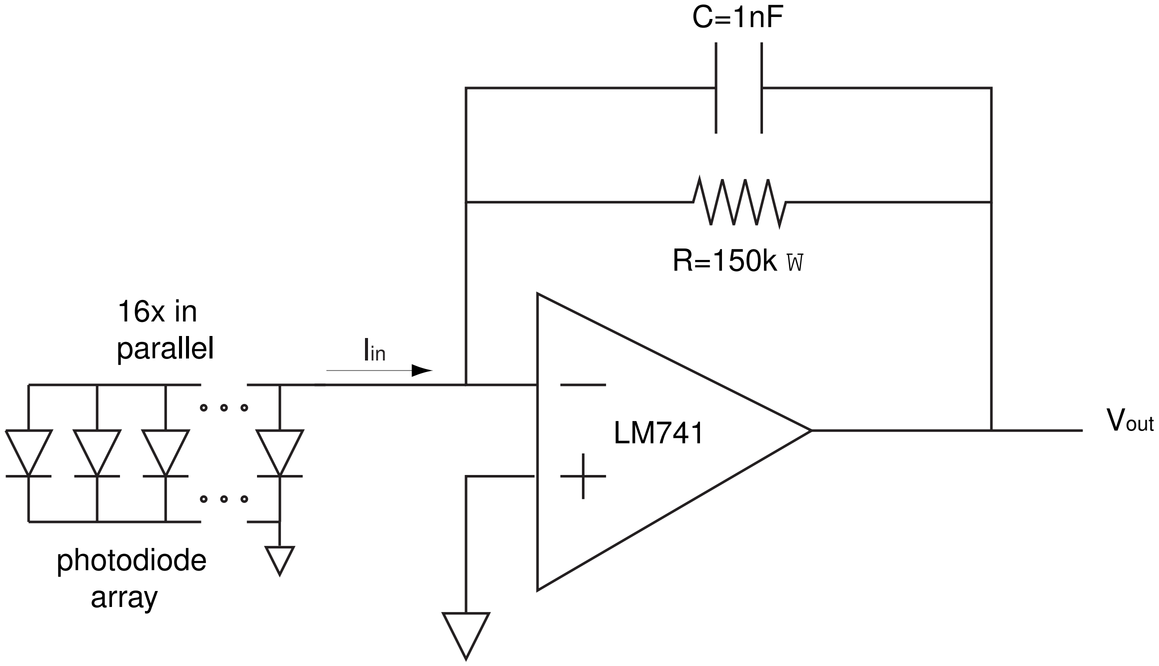

Figure 2-11: Transresistance amplifier circuit.

function of the circuit:

$$\frac{V}{I_{in}} = -Z = -(Cs + \frac{1}{R})^{-1} = \frac{-R}{RCs + 1}. \tag{2.8}$$

The DC gain is R and the -3 dB bandwidth is $\omega = \frac{1}{RC}$; this requires $C = 1$ nF.

We calibrated the sensor with a 1 μm resolution micrometer and steel ball fixture. Set at different gap lengths, we recorded the corresponding voltage reading from the transresistance amplifier. The plot of the data is in Figure 2-12. The sensor is sufficiently linear over the operating range - the change in voltage is essentially proportional by a constant to the change in gap length. The calibrated function is

$$V = -424x + 0.8, \tag{2.9}$$

where V is in volts and x is in meters. In the controller, we use this linearly interpolated function to represent position.

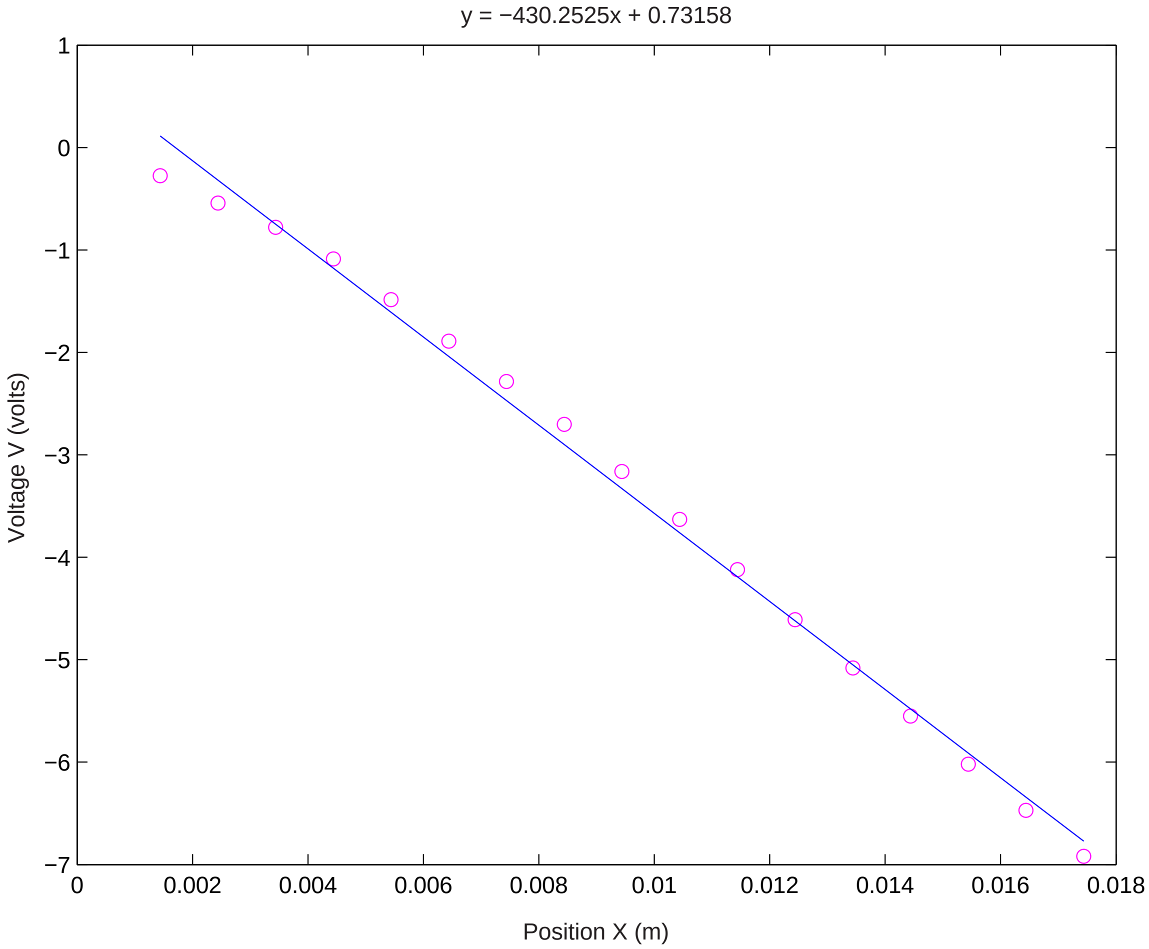

Figure 2-12: Calibration of position sensor - voltage vs. position. Data interpolated with a linear best-fit line.

Chapter 3

Force Measurement

3.1 Introduction

For feedback linearization to be successful, it is necessary to develop an accurate model of the system. The algebraic transformation makes this approach heavily dependent on careful modeling of all dynamics and minimizing errors in modeling. It is one of the drawbacks of this technique because there are situations where such modeling is not possible. We develop an approach to modeling based on a mix of theory and experimentally-determined results.

3.2 Theory

The physics of the setup is similar to that developed in [13, pgs.22-23, 84-86] except it is inverted such that gravity acts to open the air gap. The key equation to take from [13] is the force produced by the electromagnet

$$F = C\left(\frac{i}{x}\right)^2 . \tag{3.1}$$

Here, F (Newtons) is the force applied to the ball, x (m) is gap spacing between the pole of the electromagnet and the ball, and i (Amperes) is the current through the inductor. The gap length is increasing in the downward direction; therefore, a

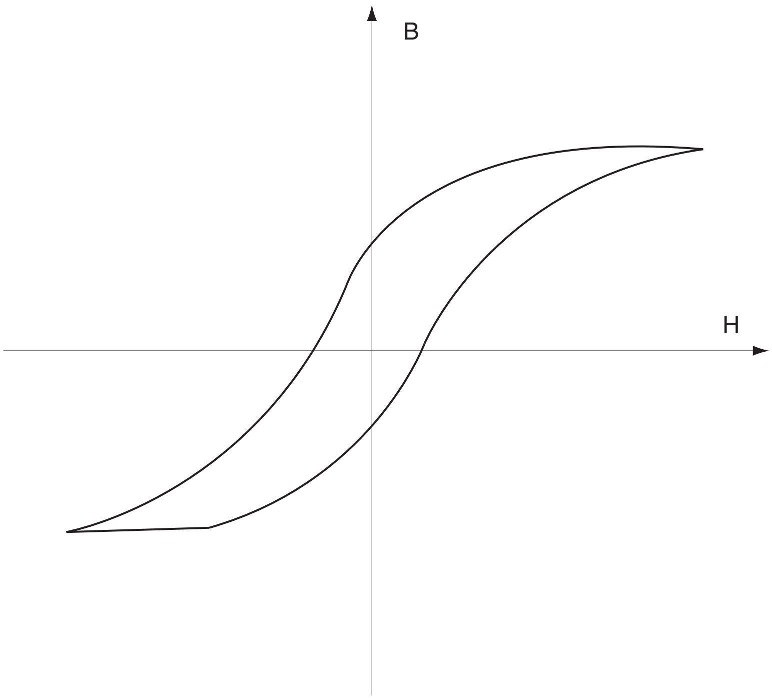

Figure 3-1: Hysteresis in B-H curve for a magnetic material.

large value of x places the ball far from the pole face. It is important to keep in mind equation (3.1) is a simplified approximation for our system, as it ignores many nonidealities. Later, we supplement the model with experimental data accounting for these differences. Specifically, the equation does not account for a number of effects including finite core reluctance, saturation of the core, magnetic hysteresis, and eddy currents in the core. We address each of these issues in turn.

The ideal case assumes the path of magnetic flux has infinite permeability everywhere except at the variable air gap. All the flux would then be concentrated in the air gap. Analyzing this as a magnetic circuit, the flux path would be the wire, coil ampere turns the voltage source, air gap the resistor, and flux the current. As the air gap closes, the resistance approaches zero. Therefore, the current goes to infinity, or analogously, the flux goes to infinity. In reality, just as there is parasitic resistance in a real wire, there is a finite reluctance in our magnetic path. The force on the ball is not infinite with zero gap space as (3.1) would suggest. We must account for this non-ideality, and we do so by adding a constant factor, x_0, to the gap length in the denominator. This results in a finite value as x approaches zero. We later determine this value experimentally.

Three additional characteristics of magnetic materials require attention: hysteresis, saturation, and finite conductivity. There is hysteresis in ferromagnetic materials that tend to stay magnetized even after the applied field has been turned off or reversed in direction. This produces a curve as shown in Figure 3-1. Depending on whether the current is increasing or decreasing, there is thus a different force value for a given current level. Therefore, the magnetic flux is dependent on both current and the prior history of magnetization. This can be a problem for systems where very precise values of magnetic flux are needed but is not necessarily troublesome in all situations. Later, we develop a model for linearization in our controller based on these force measurements; therefore, an acceptable representation of magnetic flux values must be developed. Fortunately, for this magnetic suspension the issue is resolved to an acceptable degree simply by taking the arithmetic mean of the hysteretic curve. We split the curves into 2 and average the values point by point. The result is a monotonic, averaged function relating the force and current. In Figure 3-2 this function is the dashed line. Heuristically, this turned out to be a sufficient solution. The force is still smoothly controllable, despite the hysteresis, unlike Coulomb friction where there are sudden changes in value. Choosing a magnetically softer core material would also reduce this problem.

Saturation occurs in all iron-core electromagnets. The flux density levels off for increasing amounts of field intensity. Essentially, when a small amount of force is applied, the domains in the magnetic material easily align to increase the flux density. However, as more flux is crammed into the cross-sectional area, there are fewer and fewer domains available. At this point, it will take more force to produce the same amount of flux density. This saturation accounts for a large part for the terms we will add in the transformation equation from force to current. For our electromagnet, due to saturation, equation (3.1) is only a reasonable fit for currents $i \leq 0.4$ A.

Finally, we address the effects of eddy currents in the core. The solid core has a conductivity σ and permeability μ. For the frequency of magnetic field oscillation ω,

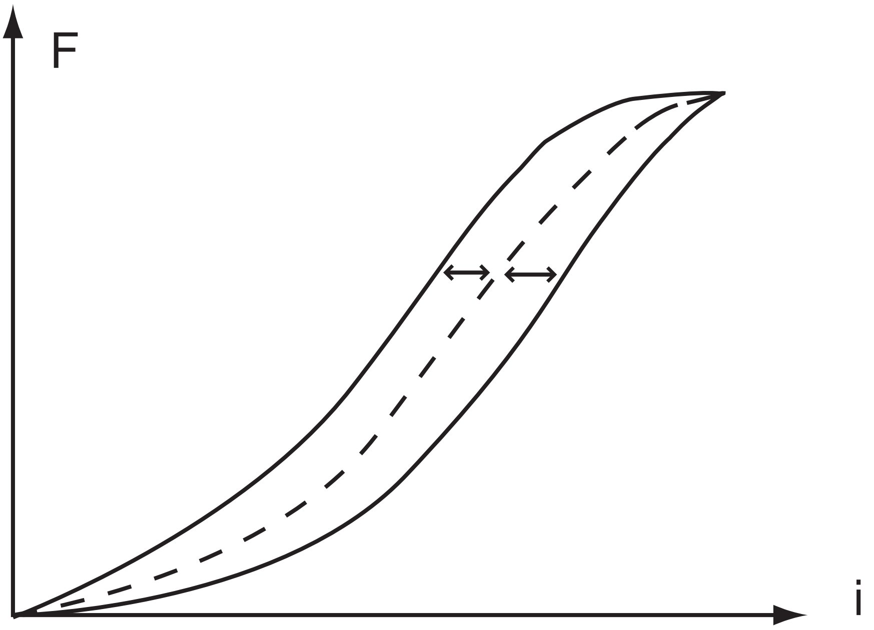

Figure 3-2: Point by point average of force curve to produce a single-valued function.

the skin depth is

$$\delta = \sqrt{\frac{2}{\omega\mu\sigma}}. \tag{3.2}$$

With $\sigma = 0$, the skin depth is infinite and we have the same field flux throughout the core at every frequency of field oscillation. However, with a finite σ, the field begins to drop off spatially within the core with the form

$$H_z = ReH_z(x)e^{j\omega t}. \tag{3.3}$$

where z is in the horizontal axis and $H_z(x) = Ce^{\frac{-x}{\delta}}$. Due to the finite conductivity, eddy currents flow within the magnetic material and essentially block out the external H-field. As the frequency of field oscillation increases, more of the field is blocked out, and the amount of field diffusion into the material decreases. A more detailed discussion on skip depth and eddy currents is given in [2, p. 442]. For our purposes, the effect of eddy currents manifests as a fall off in actuator force as a function of frequency (with an attendant negative phase shift), as the core is less effective at higher frequencies.

3.3 Methodology

We proceed by developing experiments to determine C and x_0 in the model:

$$F = C\left(\frac{i}{x + x_0}\right)^2 + \text{additional terms.} \tag{3.4}$$

The constant C is dependent on material properties and physical structure. Finally, we included additional terms to account for saturation and approximations in geometry to fit the experimental data to be discussed later.

We used a preamplifier, micrometer fixture with load cell, linear amplifier, and dSPACE to carry out the experiments. Figure 3-3 shows the arrangement (preamp not shown). Figure 3-4 is a photograph of the micrometer fixture in place. The preamplifier is a dual-mode amplifier, model 504E from Kistler. It is used for signal conditioning, operating in the charge mode. The preamplifier takes a charge reading from the load cell and converts this to a pound per volt measurement. We extracted the resulting data through dSPACE, and this was passed into the computer for further processing.

The dynamics of the linear amplifier are fast enough that it is essentially an ideal current source. The amplifier takes a voltage command that maps voltage to current via feedback from a sense resistor. The piezoelectric load cell is only sensitive to dynamic changes in force. Therefore, a static current command that produces a static force would eventually produce a zero force reading from the load cell, which is not the desired result. Consequently, the electromagnetic current is cycled from 0 to 1 A with a sinusoidal time dependence. We measured the output of the load cell at 200 points per cycle with a sinusoidal frequency 1 Hz, which is sufficiently slow to view as static. This produces points at different current levels all along the sine wave. We repeated this process at several gap lengths over the operating range giving us data on the force, air gap, and current from which the constants may be determined.

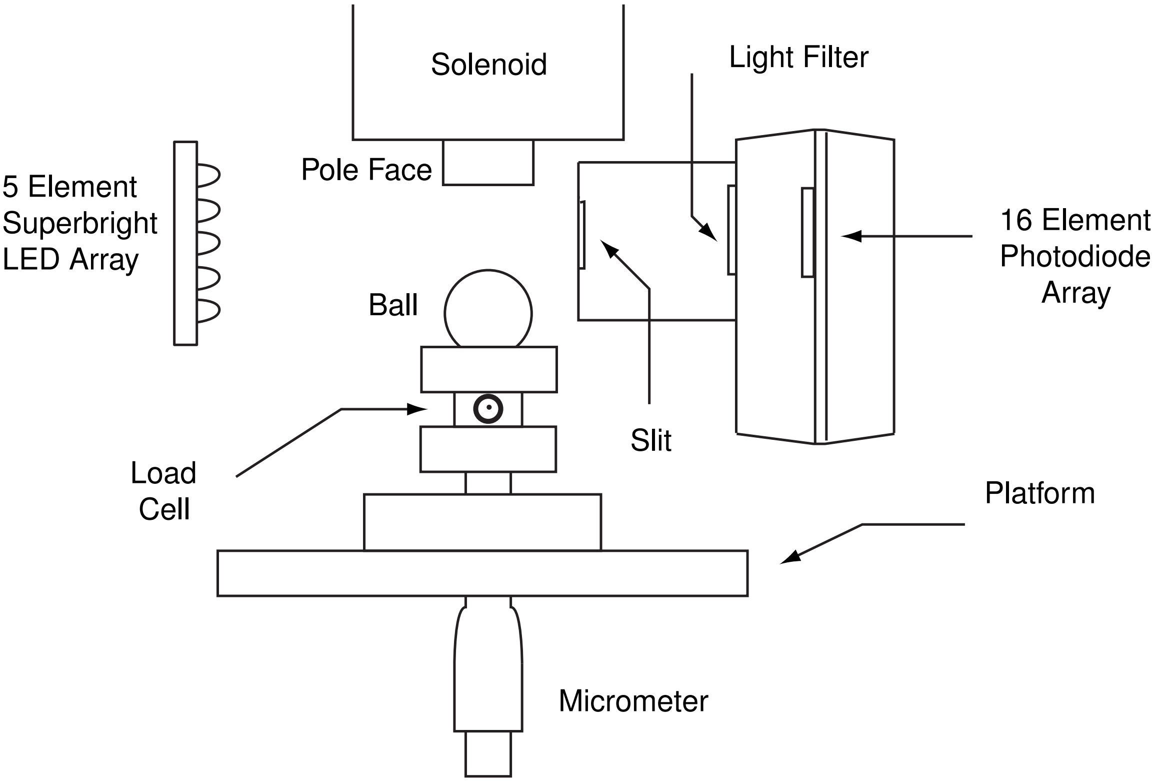

Figure 3-3: Setup with micrometer for force measurement.

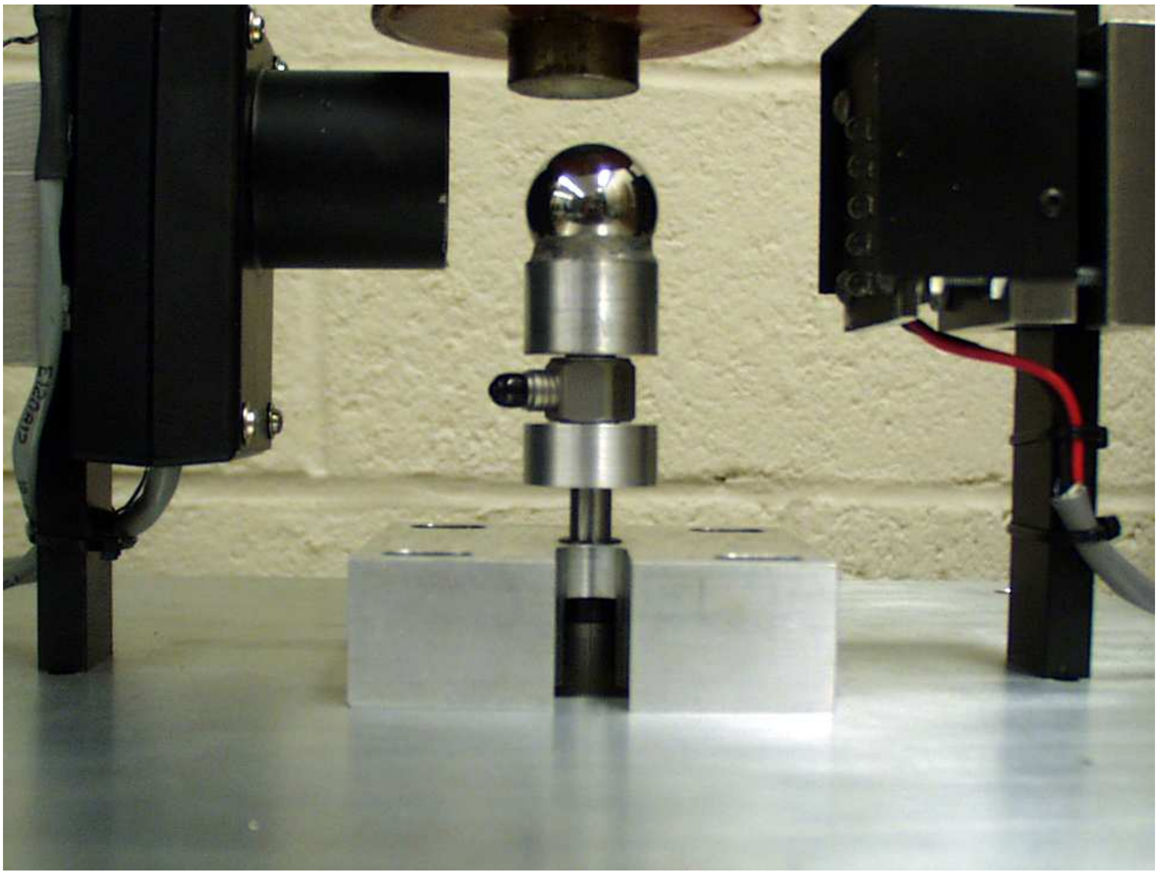

Figure 3-4: Micrometer fixture in place as a force measurement device.

3.4 Data Analysis

Using ControlDesk, a dSPACE software tool, we recorded measurements and saved the data in a format readable by Matlab. The files were then imported into Matlab for post-experimental processing. The data were in separate files associating to a given gap length, and within each file is recorded a force vs. current relationship. Ultimately, we would like to have a matrix with force, current, and air gap, each as a separate column vector in a matrix.

The first step was to extract the 2 variables, force and current, and then tag each data pair with its associated gap length. Therefore, within a file each data pair will have the same value in the third column of the matrix.

$$\begin{bmatrix} f_1 & i_1 & x_1 \\ f_2 & i_2 & x_1 \\ f_3 & i_3 & x_1 \\ . & . & . \\ . & . & . \end{bmatrix} \tag{3.5}$$

We create a matrix like the one above for each file. Finally, the matrices are appended together. This makes it possible to examine the relationships of the 3 variables in any permutation (see Appendix D for Matlab code).

Equation (3.1) would result if the iron core had infinite permeability or zero reluctance. However, the permeability is finite and that means some of the reluctance is in the core. Due to the finite permeability, a term x_0 is added to the equation (3.4). This is determined by plotting a family of force curves with current as a function of gap spacing (see Figure 3-5). In the ideal zero reluctance case, the curves would intersect at $x = 0$. However, for the measured data they intersect at $x = -0.0025$ m. Solving for the current as a function of x, we see where the curve intersects the horizontal axis is $x = -x_0$, or $x_0 = 0.0025$ m, which is modeled as

$$i = \sqrt{\frac{F}{C}}(x + x_0). \tag{3.6}$$

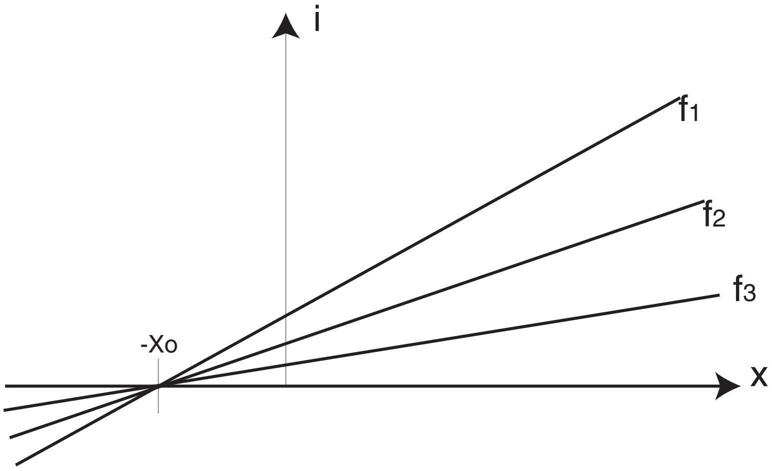

Figure 3-5: Predicted shape of current vs. position curves with several different forces.

The variable F changes the slope of the curve and x_0 is the offset in x. At every value of F, the curves should all intersect at x_0. The experimental data is plotted in Figure 3-6, and we see it closely matches the predicted results.

The constant C has units of $\frac{\mathrm{Nm}^2}{\mathrm{A}^2}$ and is dependent on the geometry of the setup, and materials. Here, we determine it experimentally. Earlier work assumed this value to be a constant. We found that the constant is more closely a linear function of x. Including this in our transformation adds accuracy to our modeling. Plotting force versus current, we see that for a constant force, there are current values associated with each gap length. Solving for C gives:

$$C = F\frac{(x + x_0)^2}{i^2} \tag{3.7}$$

A plot of C vs. x at different force values is shown in Figure 3-7. The linearly interpolated function gives

$$C = -0.003x + 6.5 \times 10^{-4} \tag{3.8}$$

where C is in Nm^2/A^2 and x in mm.

Finally, additional terms are needed in the transformation as the actual data does not represent a square root fit throughout. The first part of the curve is roughly a

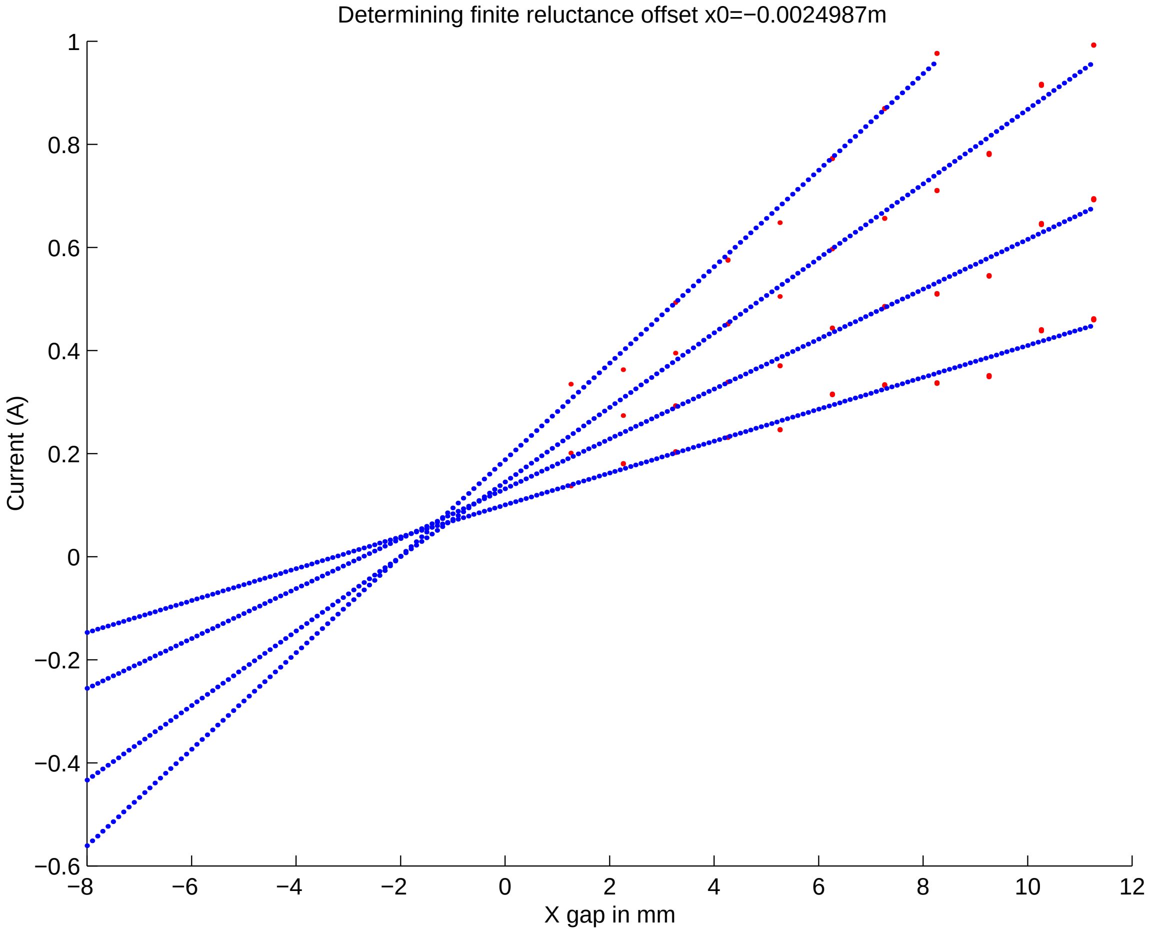

Figure 3-6: Actual of current vs. position curves with several different forces.

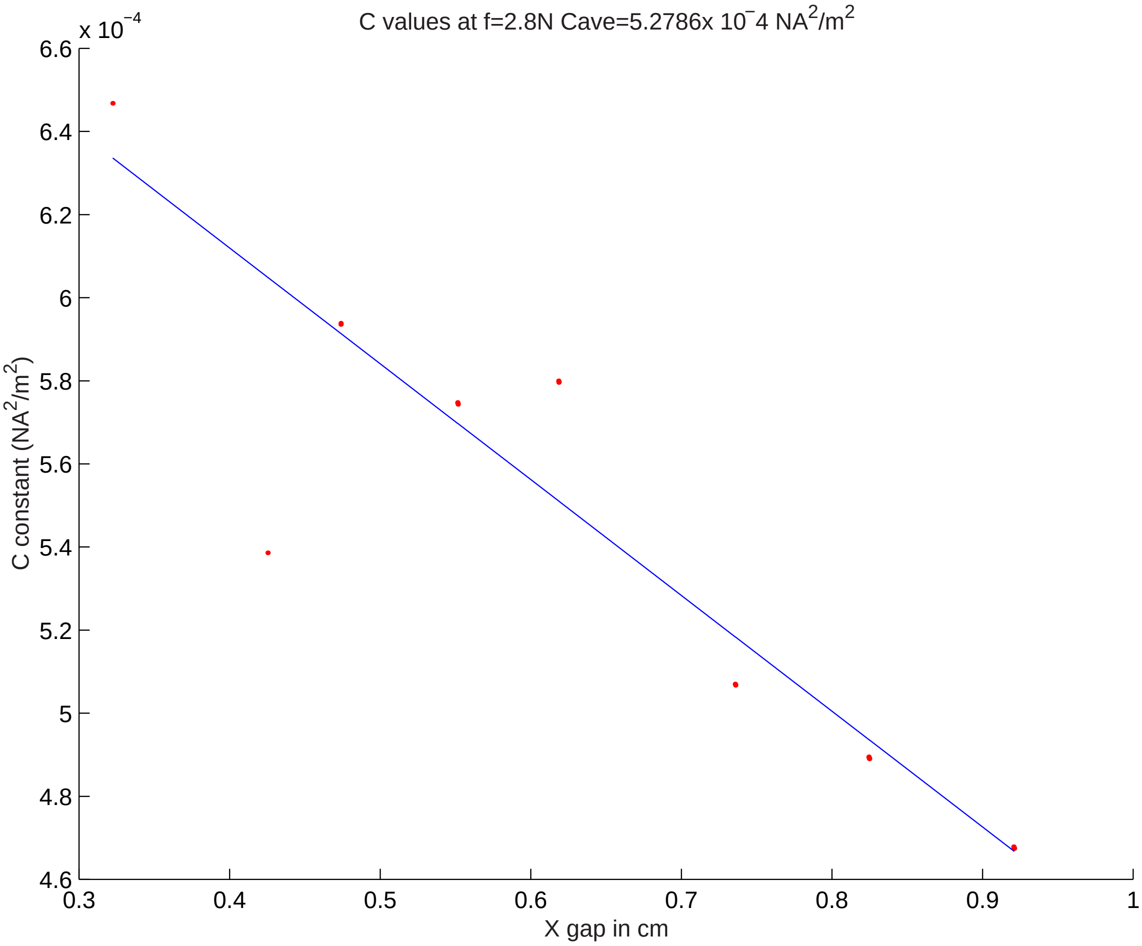

Figure 3-7: Plot of values of C as a function of air gap at different force values.

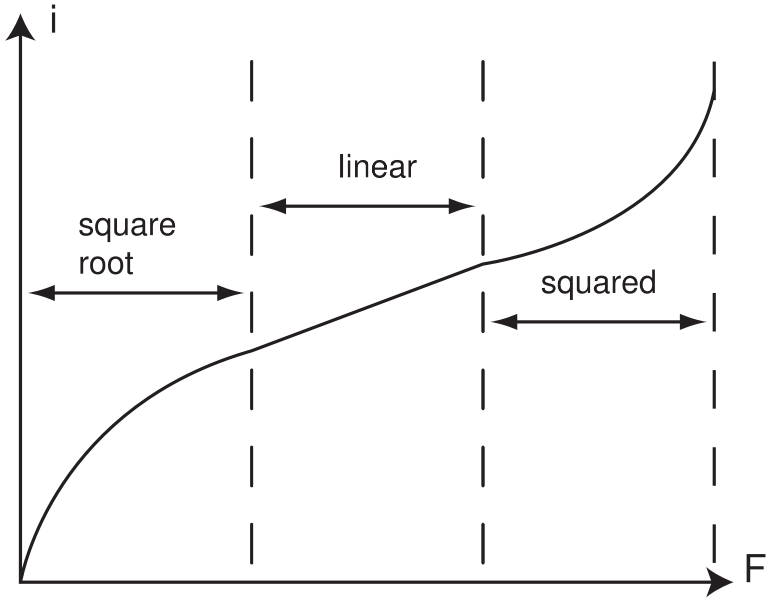

Figure 3-8: Empirically fitting current equation to experimental data.

square root function but this is only valid until about $i = 0.4$ A. Saturation takes over beyond this point; we see a flattening out and eventual curve up. In prior experimentation with work done in [11], the equation empirically fit was:

$$i = (x + 0.0025)\sqrt{\frac{F}{C}} + (0.0195e^{\frac{x-0.002}{0.006}} - 2.5(x - 0.01))F + 400(x - 0.002)^2F^2. \quad (3.9)$$

We can analyze the curve in 3 segments: a square root portion, linear, and squared (see Figure 3-8). Then, we fit region each region separately through trial and error. The result for the present work is

$$i = (x + x_0)\sqrt{\frac{F}{C}} + (0.0195e^{\frac{x-0.002}{0.006}} - 3.5(x - 0.007))F + 450(x - 0.0014)^2F^2. \quad (3.10)$$

where F is in Newtons, i Amperes, x meters, and $C = -0.003x + 6.5 \times 10^{-4}\ Nm^2/A^2$. The equation is only valid for $x \geq 0.002$ m. The resulting curve fit is shown in Figures 3-9, 3-10, and 3-11 for different gap lengths. The points represent the experimental data and the curve is that produced by our current equation (3.10). Appendix D includes the code used to generate these plots. From the figures, we see the equation works well over a wide range of gap lengths.

The development of an accurate force, current, and gap spacing is very important to the control of this system with a feedback linearization approach. We started with theory as a guide and then experimentally determined the unmodeled components of the force relationship.

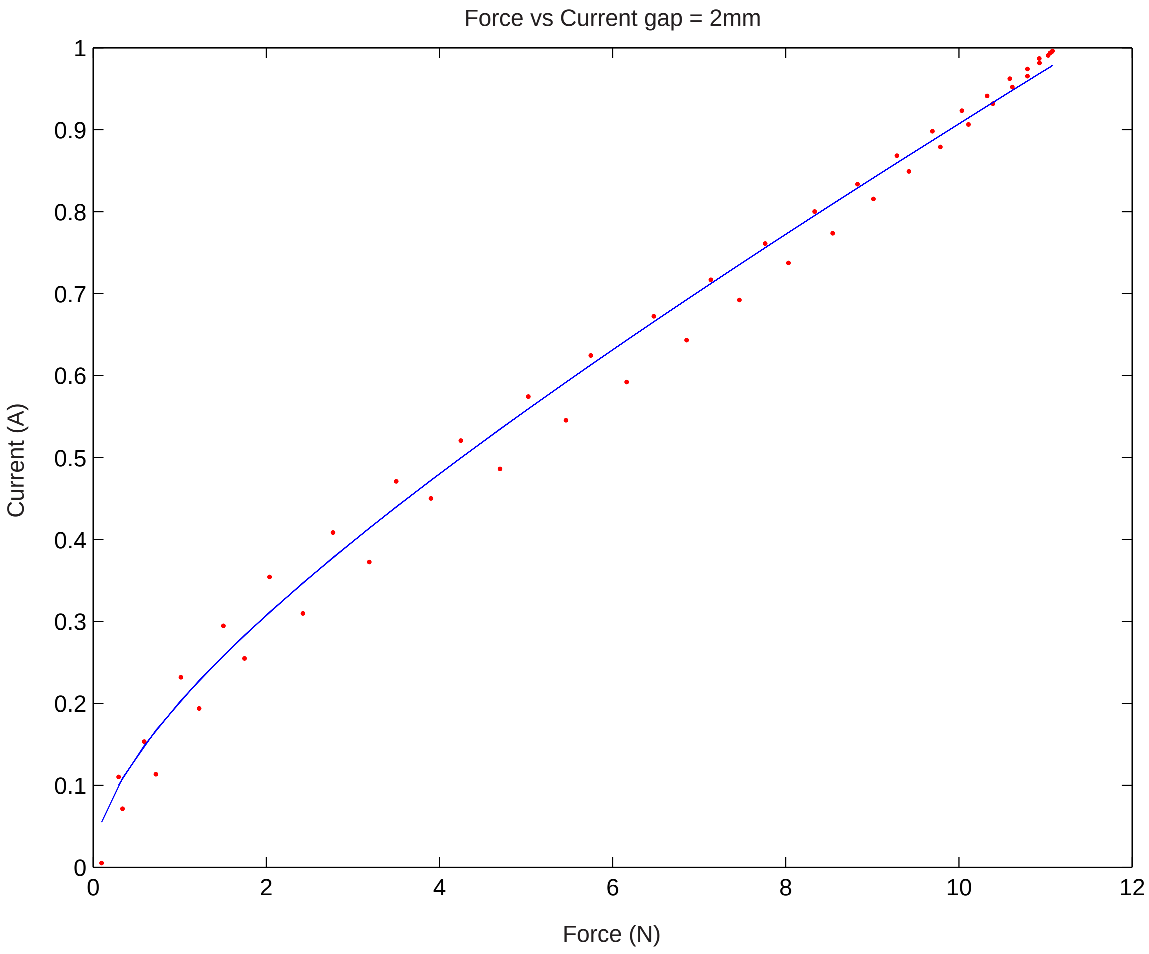

Figure 3-9: Air gap at 2mm - fitted and actual current vs. force.

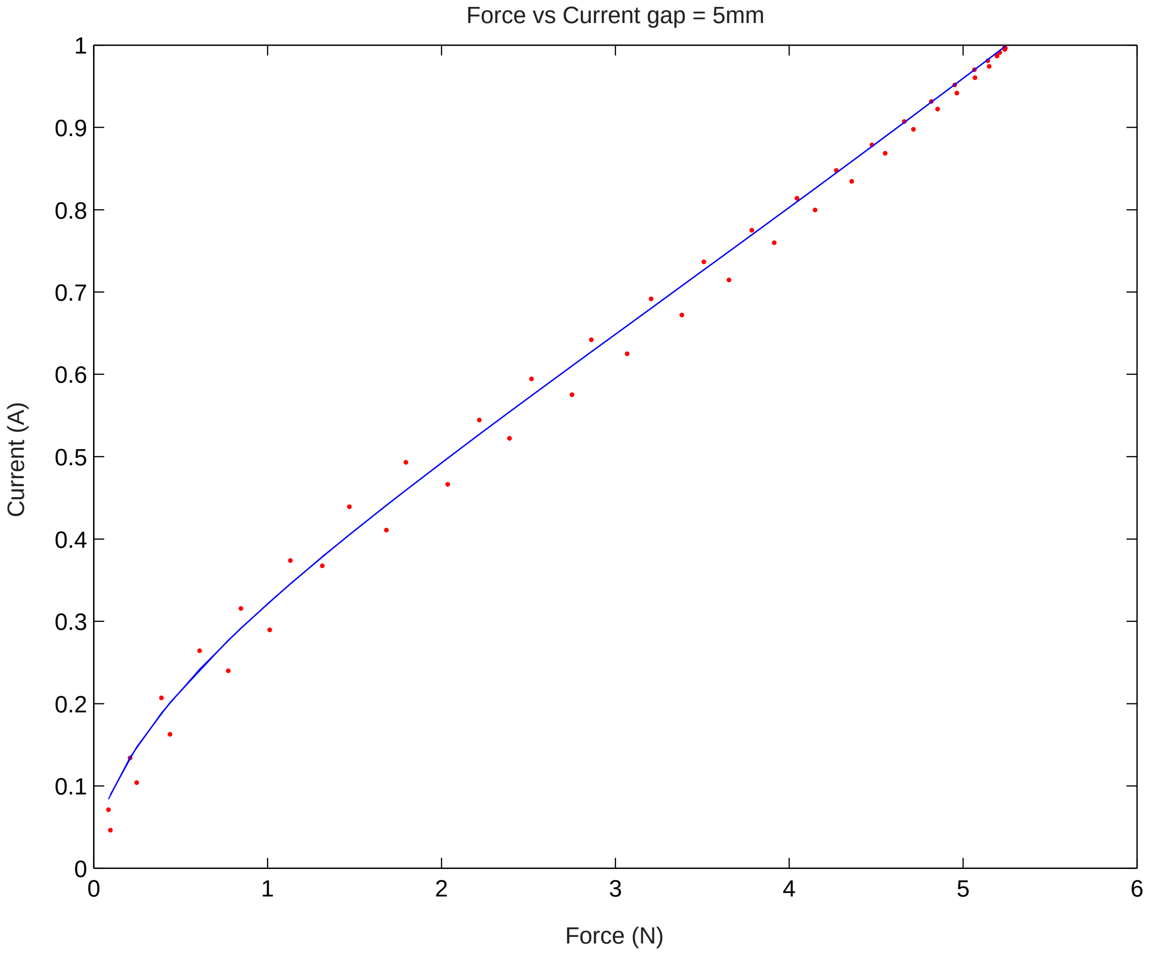

Figure 3-10: Air gap at 5mm - fitted and actual current vs. force.

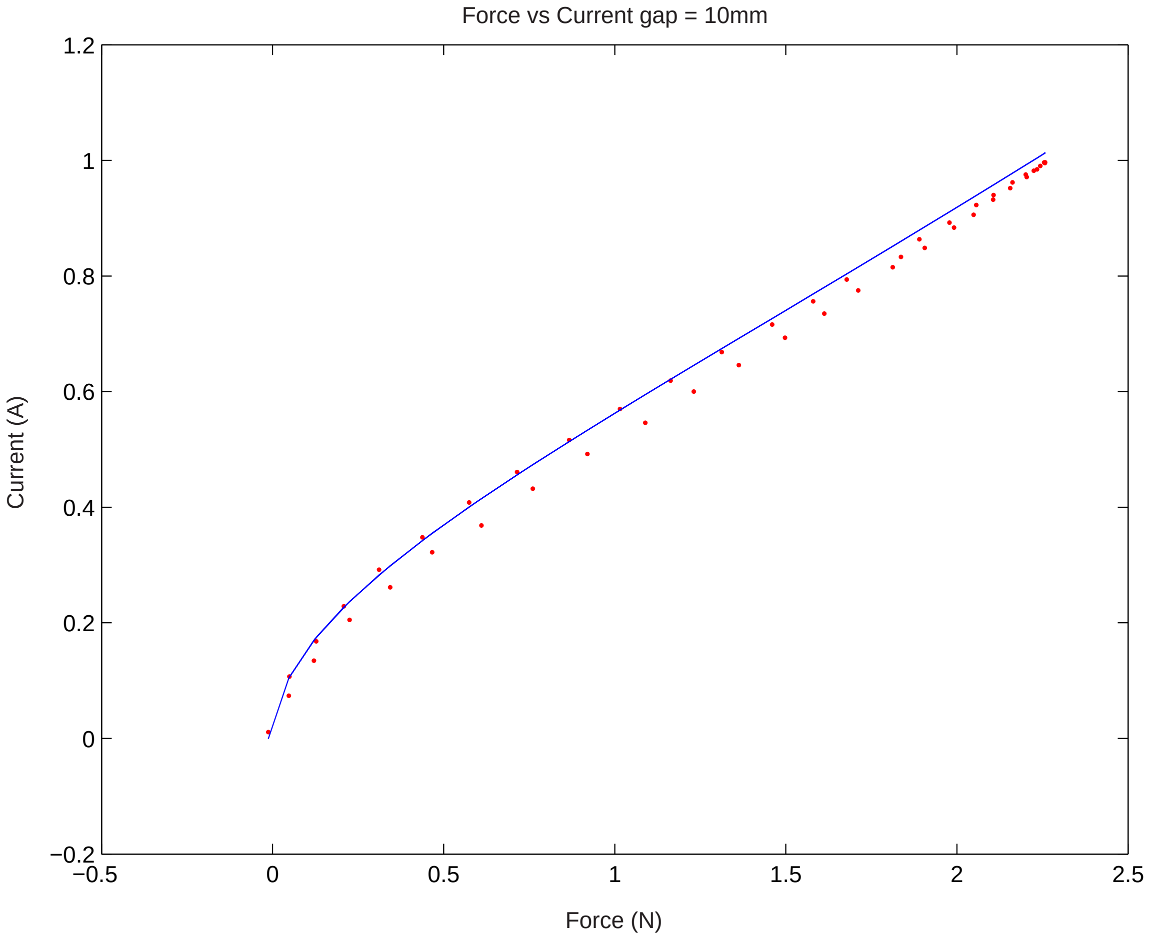

Figure 3-11: Air gap at 10mm - fitted and actual current vs. force.

Chapter 4

Nonlinear Control Theory

4.1 Linearization

If you hold a ball up and let go, it falls because of gravity. It is necessary to cancel this downward force with the force produced by the actuator, the electromagnet. The suspension of a ball with an electromagnet is difficult because it is open-loop unstable and there is a nonlinear relationship between force, current, and air gap between the pole of the electromagnet and ball. With a fixed field strength, the ball “feels” it more the closer it gets to the magnet. Equilibrium is reached when the magnetic force balances the gravitational force. The instability arises because a slight deviation from this equilibrium drives the ball further from the equilibrium point. We traditionally solve this nonlinear controls problem by linearizing about an operating point and then proceeding with the usual control techniques for linear systems. The idea is to approximate the system behavior over a limited range. Here, we present this approach as a point of comparison and to show the inherent open-loop instability of the system. The second half of the chapter is devoted to the alternative method via feedback linearization. The controller implemented for this project uses feedback linearization to allow operation over a wide range of air gaps.

Using Newtonian mechanics, we write the force equations on the ball based on

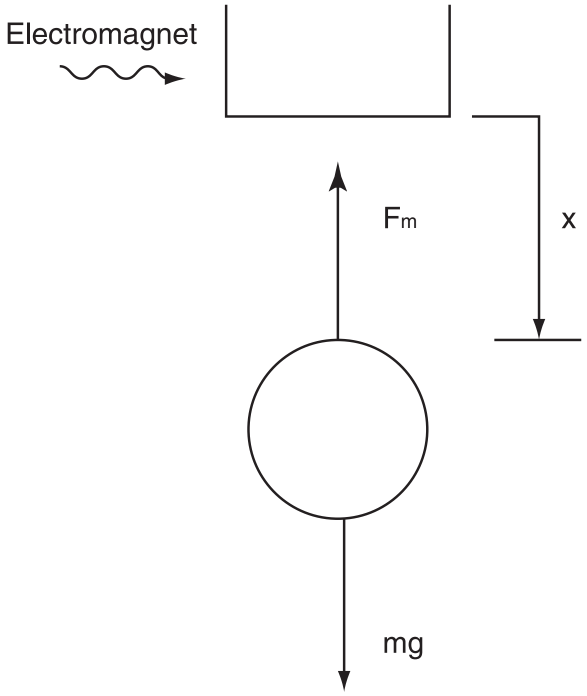

Figure 4-1: Free-body diagram showing forces acting on the ball.

the free-body diagram in Figure 4-1 with the downward direction positive.

$$m\ddot{x} = mg - F_m \tag{4.1}$$

The physics of the setup is similar to that developed in [9, chap. 3] and in [13, pgs.22-23, 84-86]. The key equation to take from [13] is the force on the ball produced by the electromagnet, which is modeled as

$$F_m = C\left(\frac{i}{x}\right)^2. \tag{4.2}$$

Here x is the distance from the pole face to the ball, as shown in Figure 4-1. Substituting into equation (4.1) gives

$$m\ddot{x} = mg - C\left(\frac{i}{x}\right)^2. \tag{4.3}$$

Our goal is to derive a differential equation with x as the output variable and i as the input variable and linearize this equation based on a tangential approximation. Since the force is dependent on both current and air gap, we must linearize about two variables.

$$\begin{aligned} i &= \bar{i} + \tilde{i} \\ x &= \bar{x} + \tilde{x} \end{aligned} \tag{4.4}$$

The bar ¯ notation represents the equilibrium operating point and tilde ˜ represents small deviations from this equilibrium. The linearized equation for the force is based on a Taylor series expansion, and because this is a 1st order approximation, we drop the higher order terms to give

$$F_m = C\left(\frac{\bar{i}}{\bar{x}}\right)^2 + \frac{\partial F_m}{\partial x}|\tilde{x} + \frac{\partial F_m}{\partial i}|\tilde{i} + \text{higher order terms.} \tag{4.5}$$

Solving the partial differentials we get

$$\begin{aligned} \frac{\partial F_m}{\partial x}| &= -2C\frac{\bar{i}^2}{\bar{x}^3}\tilde{x} \equiv -k_1\tilde{x} \\ \frac{\partial F_m}{\partial i}| &= 2C\frac{\bar{i}}{\bar{x}^2}\tilde{i} \equiv k_2\tilde{i}. \end{aligned} \tag{4.6}$$

The equilibrium point is where $m\ddot{x} = 0$. Therefore,

$$mg - C\left(\frac{\bar{i}}{\bar{x}}\right)^2 = 0$$

or

$$mg = C\left(\frac{\bar{i}}{\bar{x}}\right)^2. \tag{4.7}$$

Substituting (4.7) into (4.6) and then (4.6) into (4.1), we arrive at

$$m\ddot{x} = mg - C\left(\frac{\bar{i}}{\bar{x}}\right)^2 + k_1\tilde{x} - k_2\tilde{i}. \tag{4.8}$$

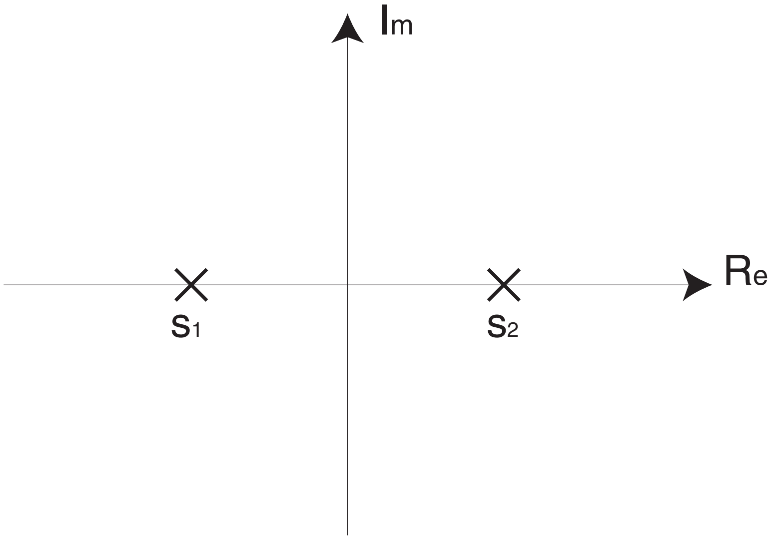

Figure 4-2: Pole zero plot of linearized system.

Using (4.8) and rearranging, our final linearized equation is

$$m\ddot{x} - k_1\tilde{x} = -k_2\tilde{i}. \tag{4.9}$$

Since $k_1 > 0$, the poles of the system are

$$\begin{aligned} s_1 &= -\sqrt{\frac{k_1}{m}} \\ s_2 &= +\sqrt{\frac{k_1}{m}}. \end{aligned} \tag{4.10}$$

Notice there is a right half plane pole, which in the linear model represents the open-loop instability of the system. Figure 4-2 shows the pole-zero plot in the complex plane. Clearly, compensation efforts have to focus on moving the right-half plane pole into the stable left-half plane region. A lead compensator along with sufficiently high gain will pull the pole over into the left-half plane. Details of lead compensation are discussed in Section 4.2.

The drawback of this approach is that it is only valid for small deviations around an operating point. It is however, simple and straightforward to implement, and leads to natural representation in state-space form, which allows easy computation. In the

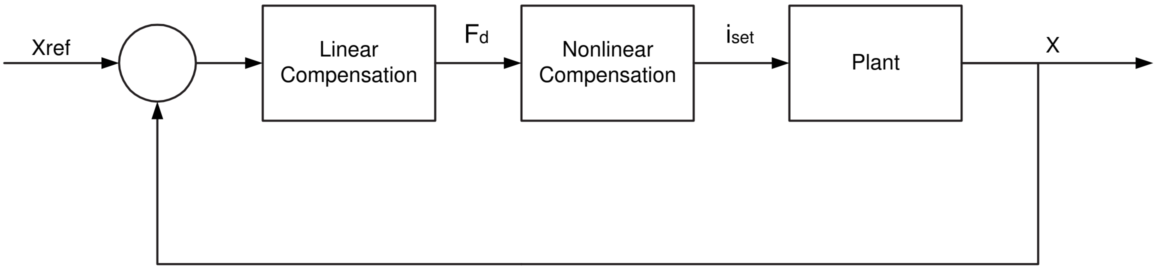

Figure 4-3: Block diagram of system showing nonlinear and linear compensation.

next section we consider another method that overcomes the limitations of traditional linearization of the plant model.

4.2 Feedback Linearization

The fundamental idea behind feedback linearization is to perform a nonlinear transformation under which the system is mapped to a linear system. A general viewpoint on the issues of nonlinear control is given in [7] and [8]. The application of such techniques to magnetic suspensions is discussed in [10] and [11]. The transformation is intended to be valid over the entire operating range. We then design a controller using the usual linear feedback techniques. Here, software carries out the nonlinear transformation. It is possible to implement the operation in analog hardware but nonlinear operations in such hardware are more difficult to implement.

In its most basic form, the closed loop system has 3 main elements: the linear compensation, nonlinear compensation, and plant. Figure 4-3 is a conceptual block diagram representation of this system. The force exhibits a nonlinear relationship with the current and the function of the nonlinear block is to make the non-linearity look linear over all operating points. Traditional linear compensation techniques are then valid to stabilize and enhance performance in the rest of the loop.

We drive the actuator in this system with a current drive amplifier so as to eliminate inductance and back emf from the dynamics, and so we perform the transformation on this variable. Solving for the current from (4.6) gives

$$i_{set} = x\sqrt{\frac{F_d}{C}}. \tag{4.11}$$

The current command to the power amplifier varies given a desired force and position measurement. Based on this algebraic operation to the extent that the model (4.2) is accurate, the suspension is globally linearized. The inputs to the nonlinear compensation block are the desired force F_d and the measured position x. The combination of the nonlinear block and plant now looks linear to the linear compensation block. The job of the linear block is to specify the variable F_d based on the difference between the reference and measured position. The nonlinear block takes F_d as an input and outputs the corresponding set point current to produce the desired force on the ball. If everything works correctly, the nonlinear compensator block and plant together have the transfer function

$$\frac{X(s)}{F(s)} = \frac{1}{ms^2}, \tag{4.12}$$

where $m = 0.067$ kg. The resulting block diagram is shown in Figure 4-4. The minus sign under the square root in the transformation results from the definition of x as the air gap, and since the magnet force points in the $-x$ direction. Therefore, a $-F_d$ would drive the coil with positive current (the current drive has inverting gain), pulling the ball up, and decreasing x. The algebraic operation is in software, the current drive in hardware, and finally there is the suspension itself: collectively they are modeled by (4.12).

The linearized system from F_d to x has two poles at the origin making it marginally stable. In actuality, the poles may be slightly offset from the origin set apart in the direction of where the poles are is shown in Figure 4-2. The more accurate the transformation, the closer the poles are to overlaying on the origin. Assuming our modeling is precise, we must now address the issue of stability by designing the controller to move these poles off the origin fully into the left-half plane.

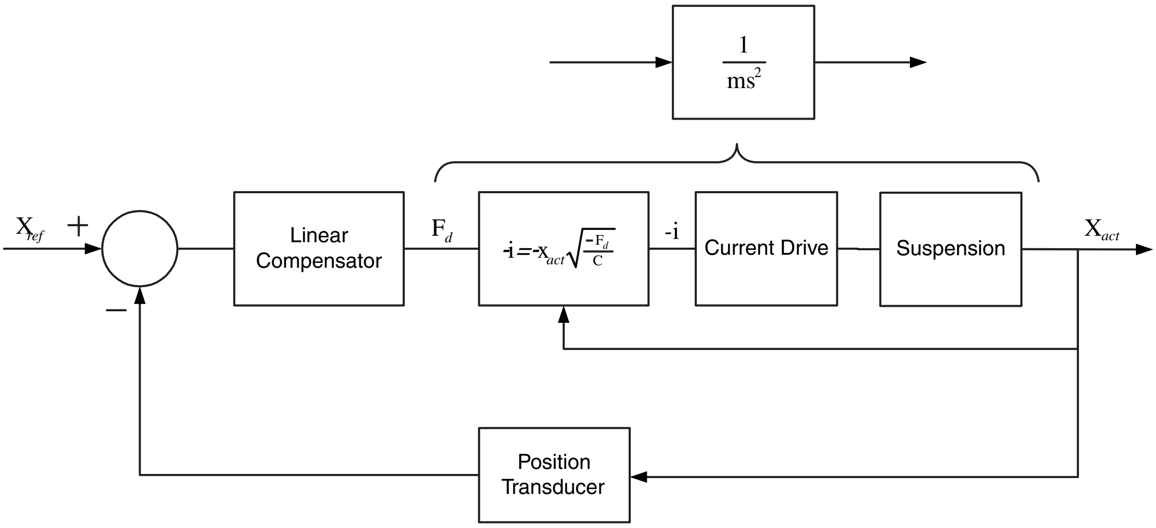

Figure 4-4: Block diagram showing nonlinear transformation.

A lead compensator has the form

$$G_c(s) = K(\alpha\tau s + 1). \tag{4.13}$$

The uncompensated plant has zero phase margin (phase is $-180°$ for all frequencies). Lead compensation adds phase in the neighborhood of the crossover frequency by taking advantage of the fact that by the time phase has increased by 45°, magnitude has only increased by $\sqrt{2}$ (see Figure 4-5). The network has a low frequency zero followed by a higher frequency pole. Therefore, when the phase from the zero starts to take effect the magnitude has not yet begun to rise significantly, and it is possible to leave the crossover frequency unchanged.

However, we use a more practical lead compensator with the form

$$G_c(s) = K\frac{\alpha\tau s + 1}{\tau s + 1}. \tag{4.14}$$

We must have the pole in addition to the zero because the zero alone gives infinite gain as $\omega \to \infty$, which is not realizable nor is it desirable for noise reasons. Typically, we set $\alpha = 10$ meaning the pole/zero pair is a decade apart in frequency, and place the crossover frequency at the geometric mean of the pole/zero pair for maximum

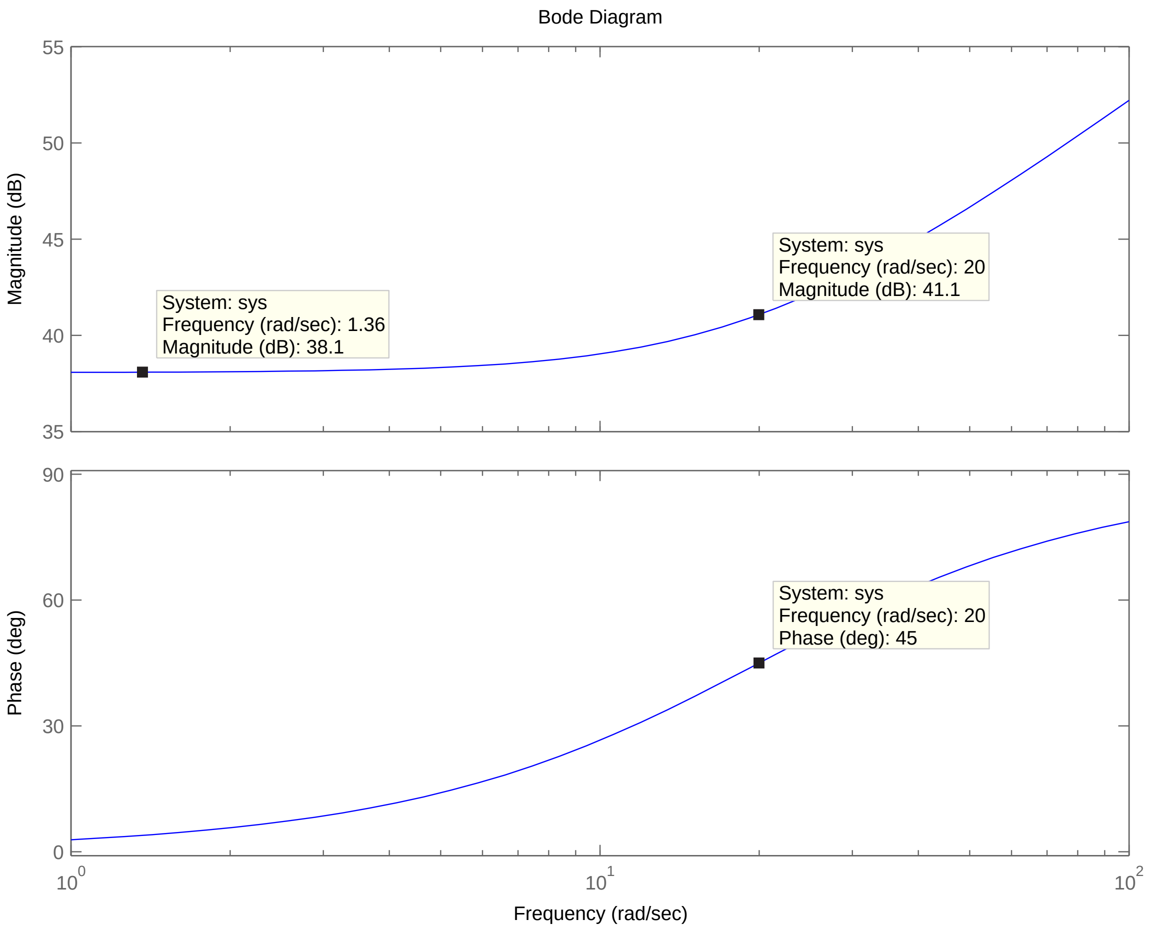

Figure 4-5: Bode plot of transfer function $G_c(s) = K(\alpha\tau s + 1)$ with $K = 80$, $\alpha = 10$, and $\tau = 0.005$. This shows the phase has already increased by 45° while magnitude has only increased by $\sqrt{2}$. However, this transfer function is not realizable and a pole must be added to level off the gain at higher frequencies.

phase improvement. The maximum phase is given by

$$\phi_m = \sin^{-1}\frac{\alpha - 1}{\alpha + 1}. \tag{4.15}$$

The Bode plot of a practical lead compensator is shown in Figure 4-6.

The lead compensator will move the poles into the left-half plane but we must properly choose the parameters to achieve desired performance. For a first cut design we chose a conservative 10 Hz. Assuming we have done the feedback linearization accurately, the transfer function of the compensated plant is given by (4.12) and the

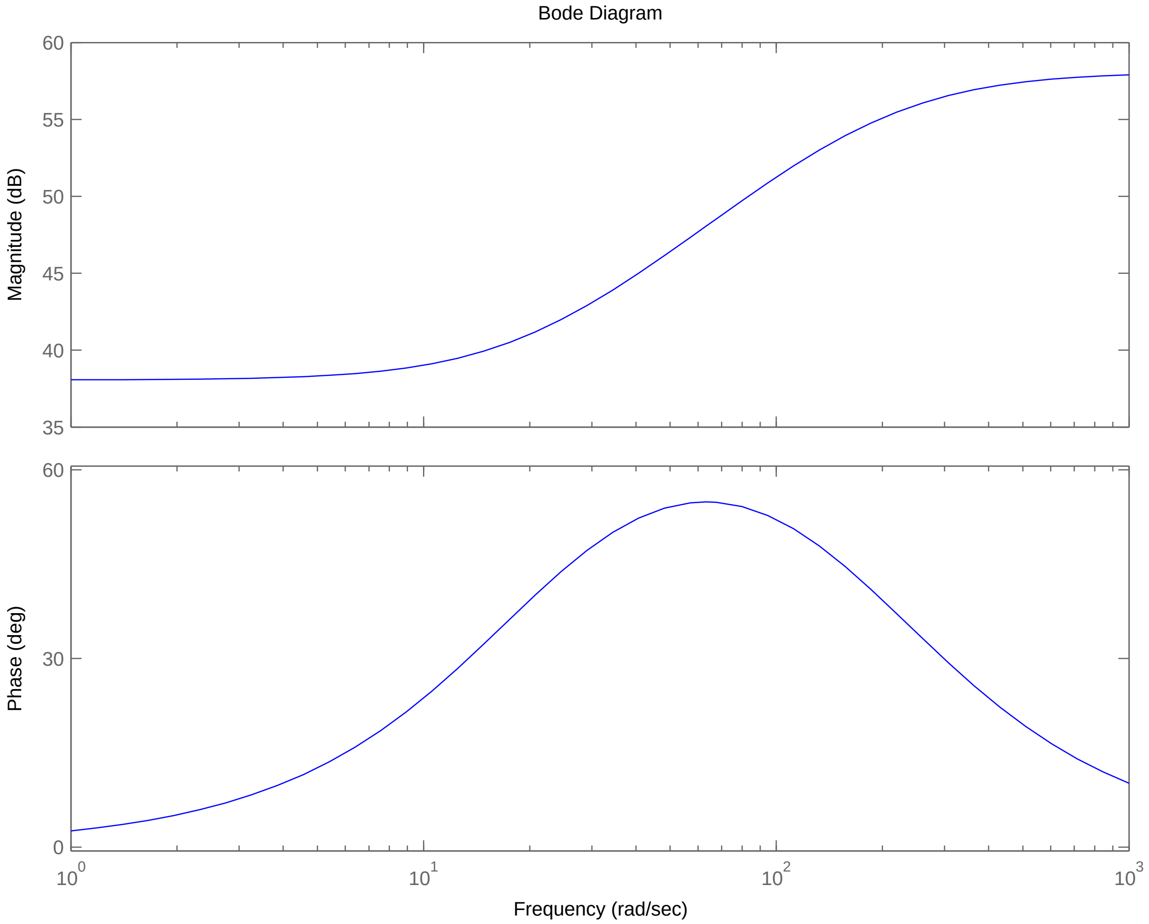

Figure 4-6: Bode plot of transfer function $G_c(s) = K\frac{\alpha\tau s+1}{\tau s+1}$, a practicial lead network with maximum phase at the geometric mean of the pole and zero pair ($K = 80, \alpha = 10$, and $\tau = 0.005$ sec). The bottom plot shows the characteristic phase “bump” of a lead compensator.

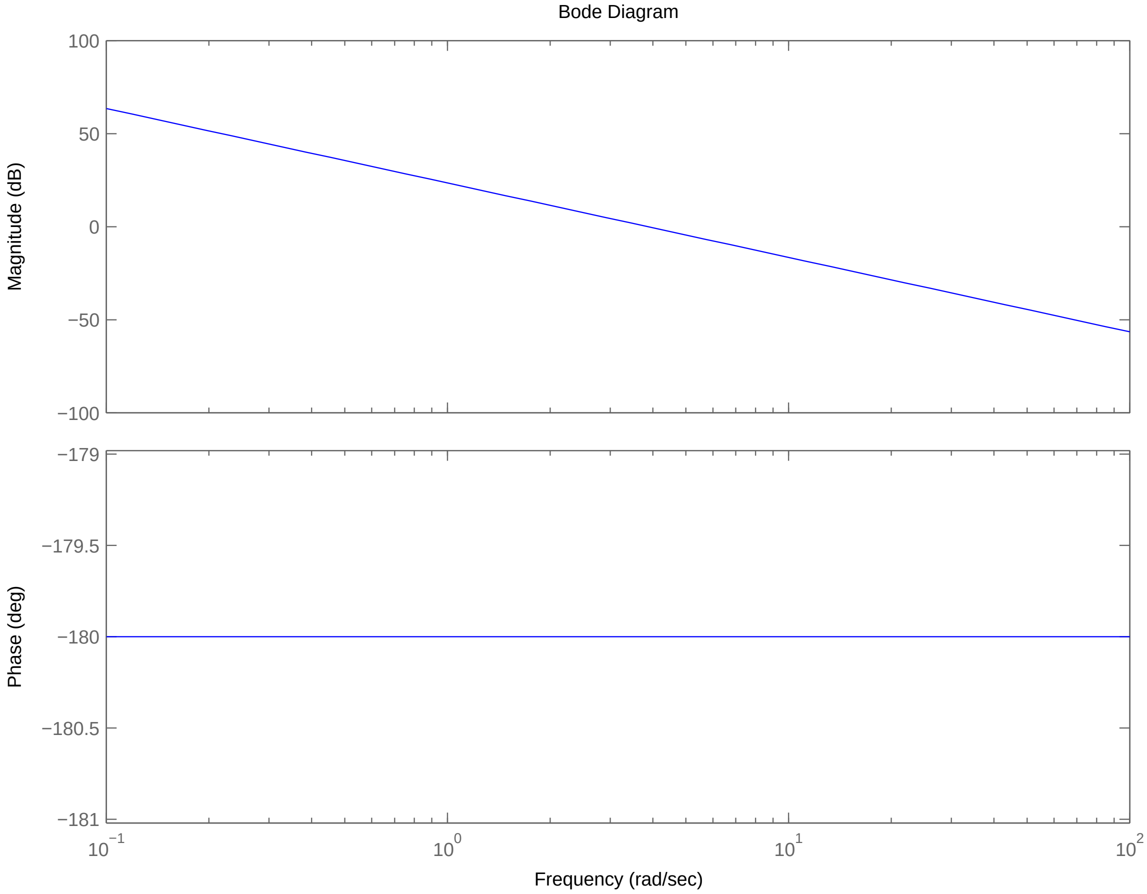

Figure 4-7: Bode plot of the theoretical linearized plant transfer function $\frac{X(s)}{F(s)} = \frac{1}{ms^2}$.

Bode plot is in Figure 4-7. The plot shows us at 10 Hz there is a gain of about -48 dB or 4×10^{-3}.

To find the loop transmission, we break the loop at any point and multiply all the blocks in the loop.

$$L.T. = K \frac{\alpha \tau s + 1}{ms^2(\tau s + 1)} \tag{4.16}$$

We want the loop transmission magnitude to equal 1 at the 10 Hz to obtain the desired bandwidth, and at least 45° of phase margin for good stability ($\phi > -135°$ at 10 Hz). To achieve this, we need the compensator to have a gain of 4×10^{-3} and $+45°$ phase at the loop transmission crossover $f_c = 10$ Hz frequency or $\omega_c = 62.8$ rad/s. Figure 4-8 depicts this scenario in block diagram form.

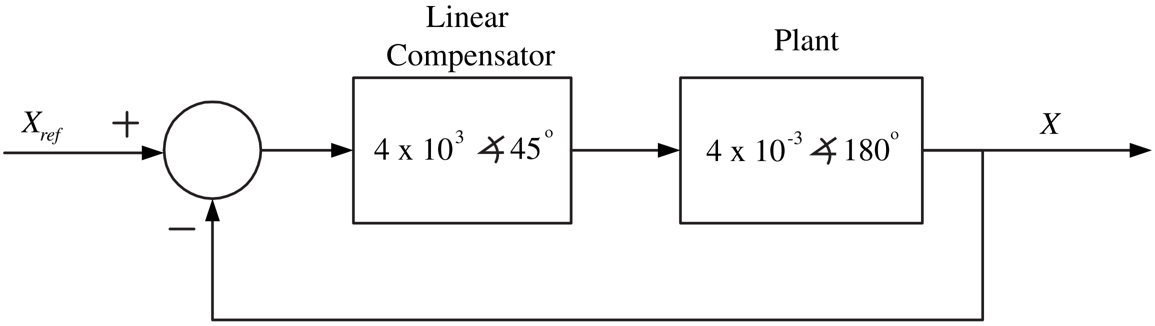

Figure 4-8: Desired compensator characteristics and plant characteristics.

From equation (4.10) the pole and zero are located at

$$z = \frac{-1}{\alpha\tau};\ p = \frac{-1}{\tau}. \tag{4.17}$$

The geometric mean of the breakpoint frequencies due to the pole and zero is therefore at $\omega = \frac{1}{\sqrt{\alpha\tau}}$. Maximum positive phase occurs at the geometric mean of the pole-zero pair break frequencies so that is where the crossover frequency should be placed,

$$\omega_c = \frac{1}{\sqrt{\alpha\tau}} = 62.8 \text{ rad/s}. \tag{4.18}$$

Given $\alpha = 10$ we thus find $\tau = 5 \times 10^{-3}$ sec. The final unknown parameter is the proportional gain K. As mentioned before, the loop transmission should be unity at the crossover frequency. Pictorially, Figure 4-9 shows the magnitude of the lead compensator is equal to $K\sqrt{\alpha}$ at $\omega = \omega_c$. Therefore, to set unity magnitude

$$\frac{K\sqrt{\alpha}}{m\omega^2} = \frac{K\sqrt{10}}{4 \times 10^{-3}} = 1, \tag{4.19}$$

and thus

$$K = 83. \tag{4.20}$$

The theoretical loop transmission and closed-loop Bode plots are shown in Figures 4-10 and 4-11 for this particular choice of parameters. There is ample phase

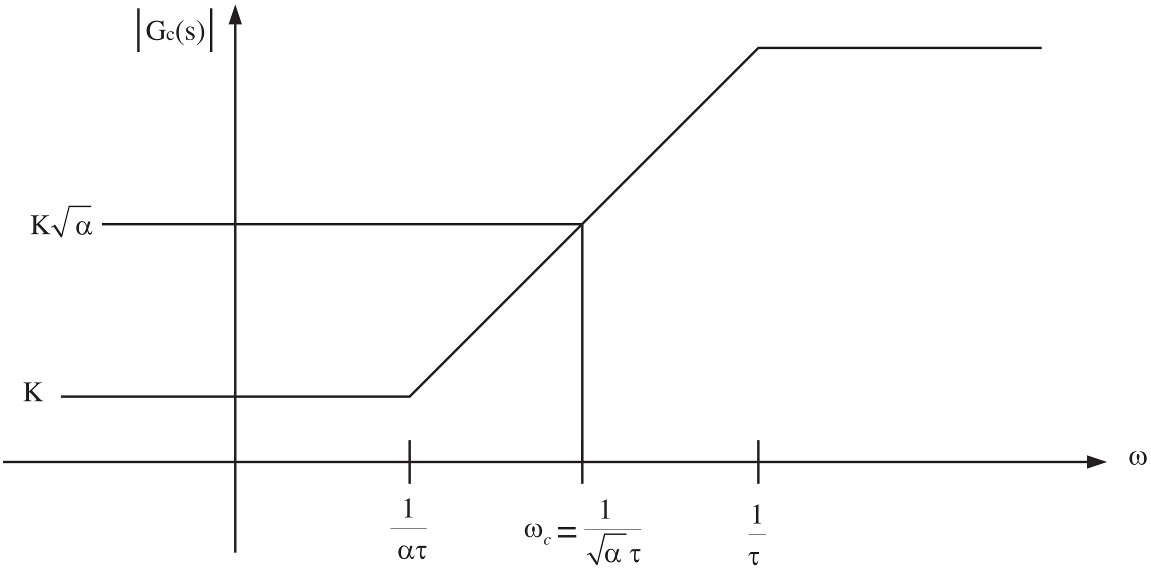

Figure 4-9: Lead compensator magnitude plot in terms of the parameters K, α, and τ. G_c is the compensator from equation (4.14).

margin, $\phi = 54.9°$ at crossover, which exceeds our spec. Looking at the step response, Figure 4-12, the system is well damped, with a settling time of $t_{settle} = 5$ ms, but does overshoot. The overshoot is due to the presence of a closed-loop zero. In the next chapter, we look at putting the lead compensator in the feedback path to move the closed-loop zero far enough out on the s-plane such that its effects are negligible.

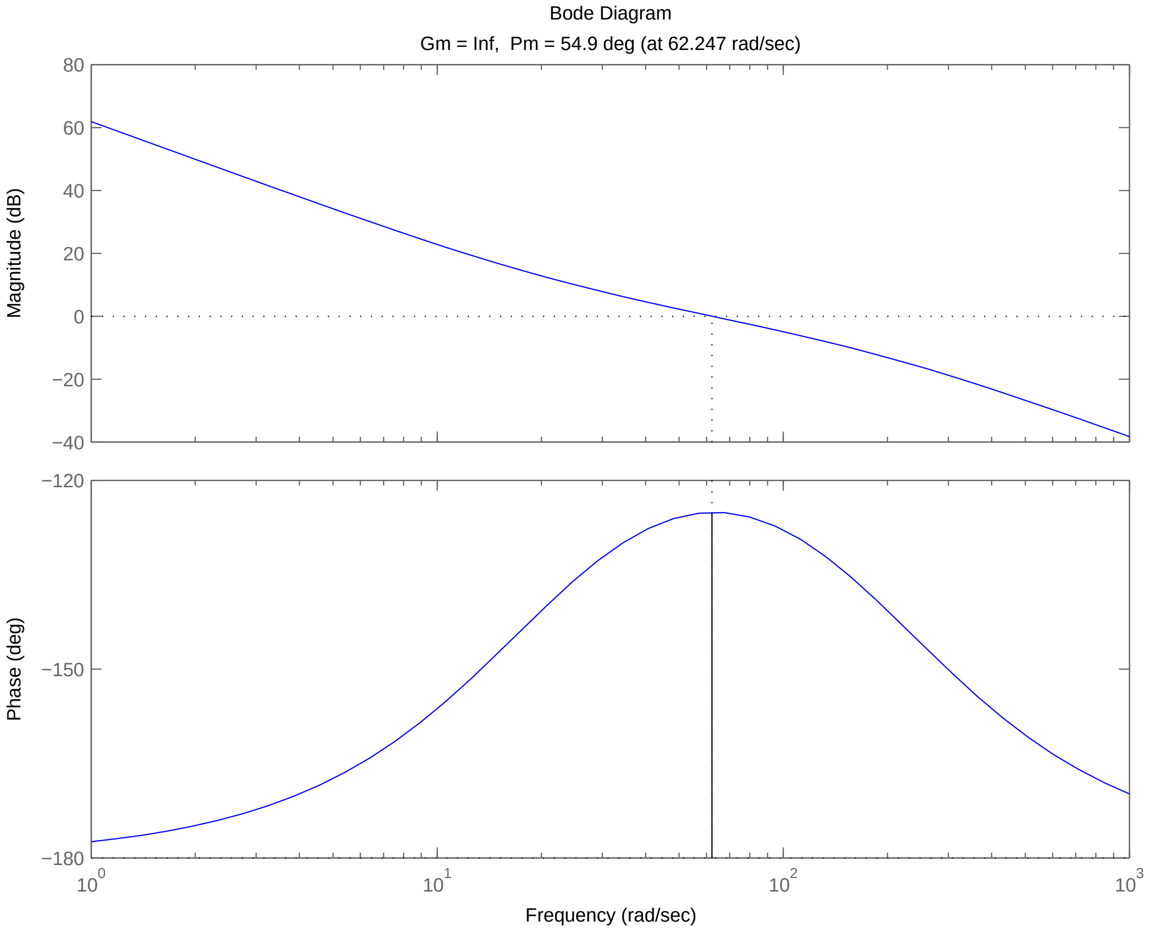

Figure 4-10: Bode plot of loop transmission with a crossover frequency $f_c = 10$ Hz using the model given by (4.14) with $K = 83$, $\alpha = 10$, and $\tau = 0.005$.

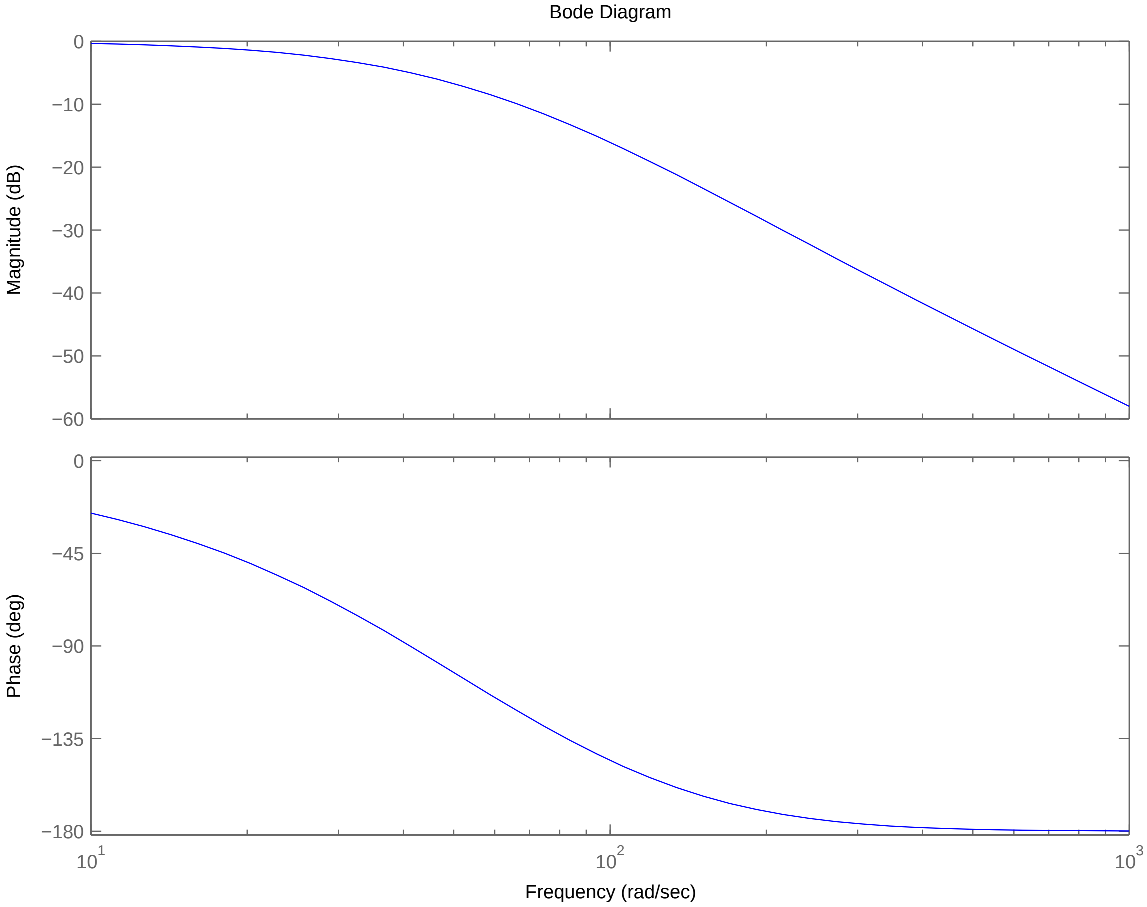

Figure 4-11: Closed loop Bode plot of system with lead compensation in the forward path using the model given by (4.14) with $K = 83$, $\alpha = 10$, and $\tau = 0.005$.

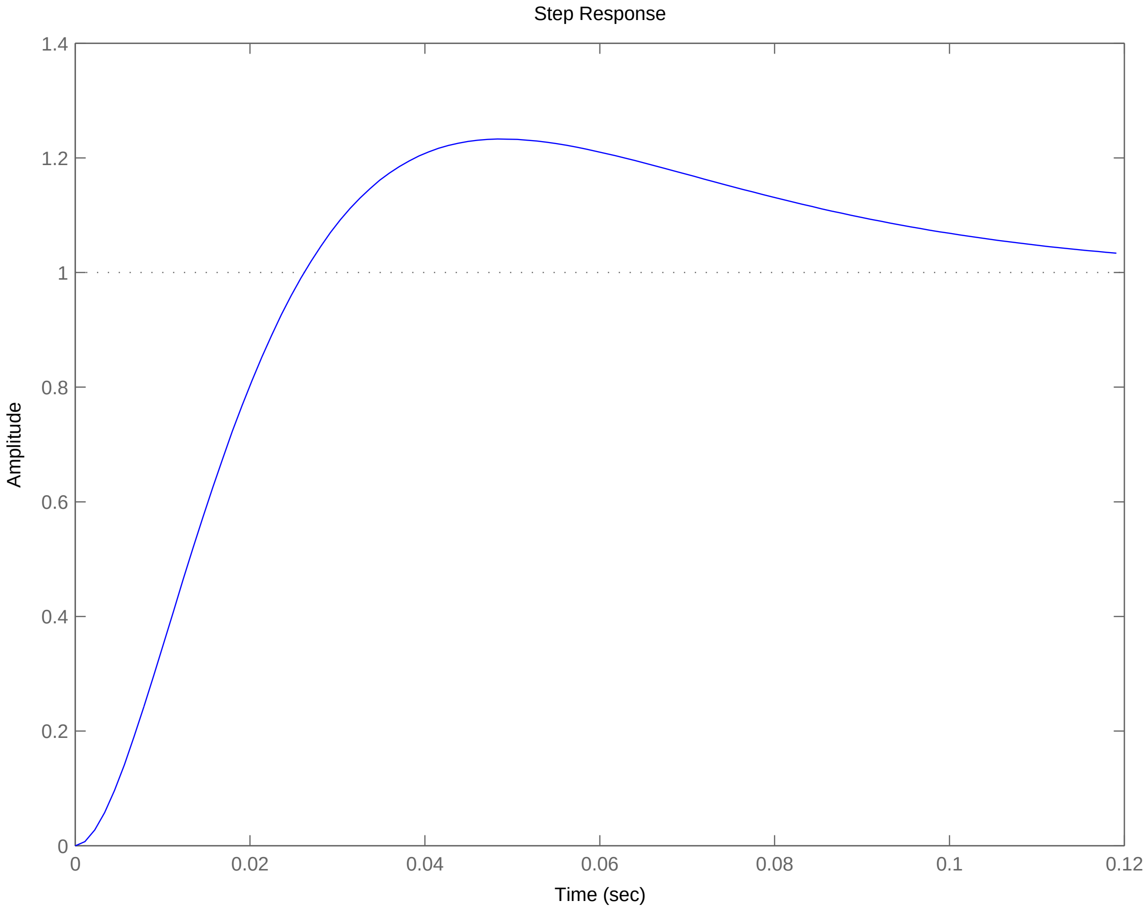

Figure 4-12: Closed loop step response with lead compensation in the forward path using the model given by (4.14) with $K = 83$, $\alpha = 10$, and $\tau = 0.005$.

Chapter 5

Design Issues and Results

5.1 Implemented Loop

The final design loop is shown in Figure 5-1. Notice we add the gravitational force to the control force in order to offset gravity. The addition reduces the steady-state error. In an open-loop approach, the weight of the ball is the desired force the electromagnet must produce to counterbalance. We subtract because the desired force is in the negative direction, which makes the value under the square root in the nonlinear transformation real. Continuing around the loop, there is the nonlinear transformation followed by the digital to analog converter that is part of the dSPACE board. In the nonlinear transformation block, we take the negative of the current command to offset the negative gain from the current drive. In the feedback path there is a position transducer to convert the measured voltage from the transresistance amplifier to a position reading, which is compared to the input reference. The lead compensator is in the feedback path rather than the forward path to deal with the overshoot due to the closed-loop zero. We explore this latter design choice in the following section.

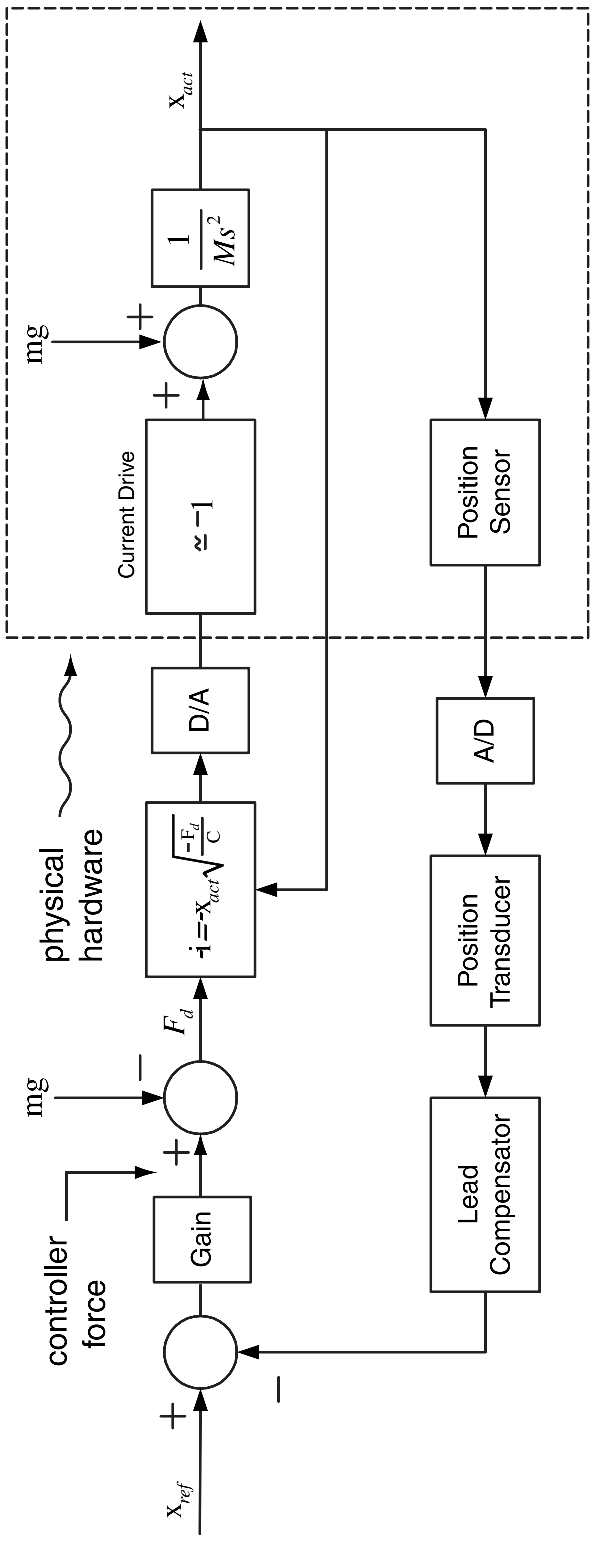

Figure 5-1: Block diagram of the closed loop design.

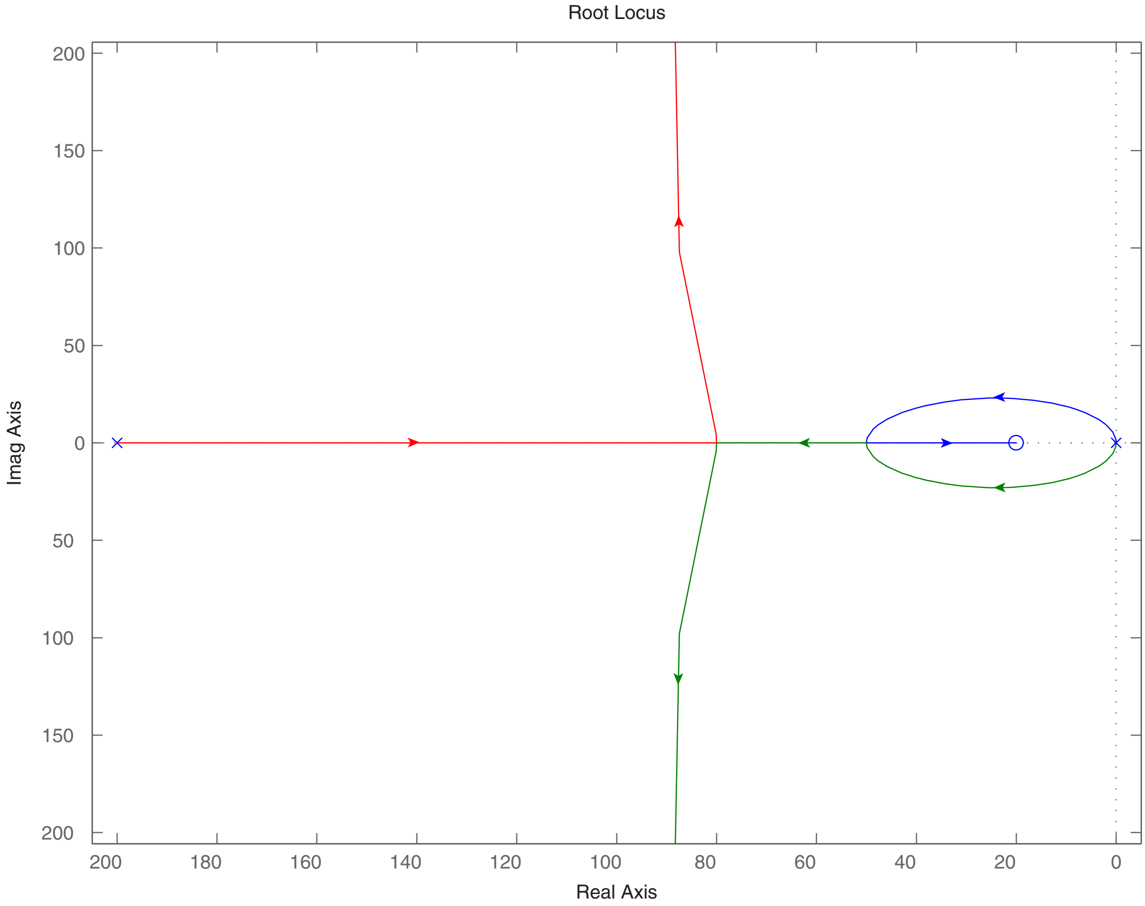

Figure 5-2: Root locus plot of suspension system with lead compensation.

5.2 Lead Compensator in the Feedback Path

As mentioned in Chapter 4, there is overshoot seen in the step response. This overshoot is due to a closed-loop zero. Looking at the root locus plot in Figure 5-2, we see as the gain increases, the two poles at the origin leave the real axis, circle around the zero, reunite on the real axis, and then split again. One of the poles moves towards the zero from the lead compensator. With $K = 83$ for the 10Hz bandwidth, Figure 5-3 shows the close loop pole locations. The zero causes the overshoot as seen in Figure 4-12 in the step response. One way to deal with this problem is to put the lead network in the feedback path rather than the forward path. Putting the compensator in the feedback path does not change the loop transmission. However, poles in the feedback path become zeros in the closed loop system. This is desirable because the lead compensator pole is at a higher frequency than the zero; thus, the closed-loop zero is now at 200 rad/s, the dynamics of which are fast enough to ignore. The resulting step response is shown in Figure 5-5. The response is now well damped, and there is no overshoot.

Recall the placement of the compensator pole was determined in part by α. With $\alpha = 10$, we have maximum positive phase. However, by moving the pole out to a higher frequency, and thereby giving up some phase margin, the closed-loop dynamics speed up. Therefore, we give up some phase margin as a tradeoff for a faster rise time. By a root-locus argument, as the closed-loop zero moves farther to the left on the s-plane, the poles will move accordingly with increasing open-loop gain.

5.3 Layout Issues

The suspension system in its final form has three main physical components: the computer (we use a laptop for portability) and accompanying dSPACE boxes, the power supply and circuitry box, and the suspension structure itself. Figure 5-6 is a photograph of the all the hardware required for this demo.

Figure 5-7 shows the interior of the finished power supply and circuitry box. The

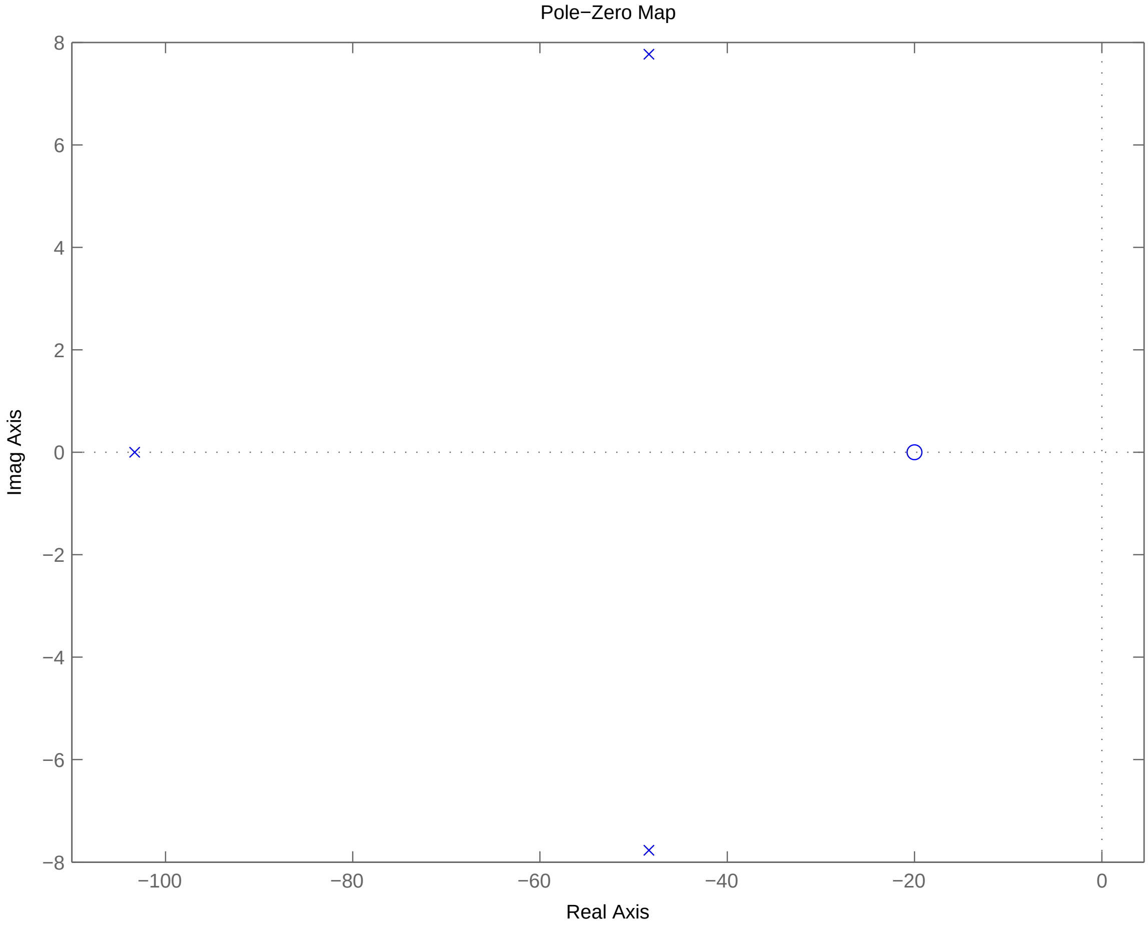

Figure 5-3: Pole-zero plot with lead compensator in the forward path. There is a low frequency zero that effects the dynamics causing an overshoot in the step response.

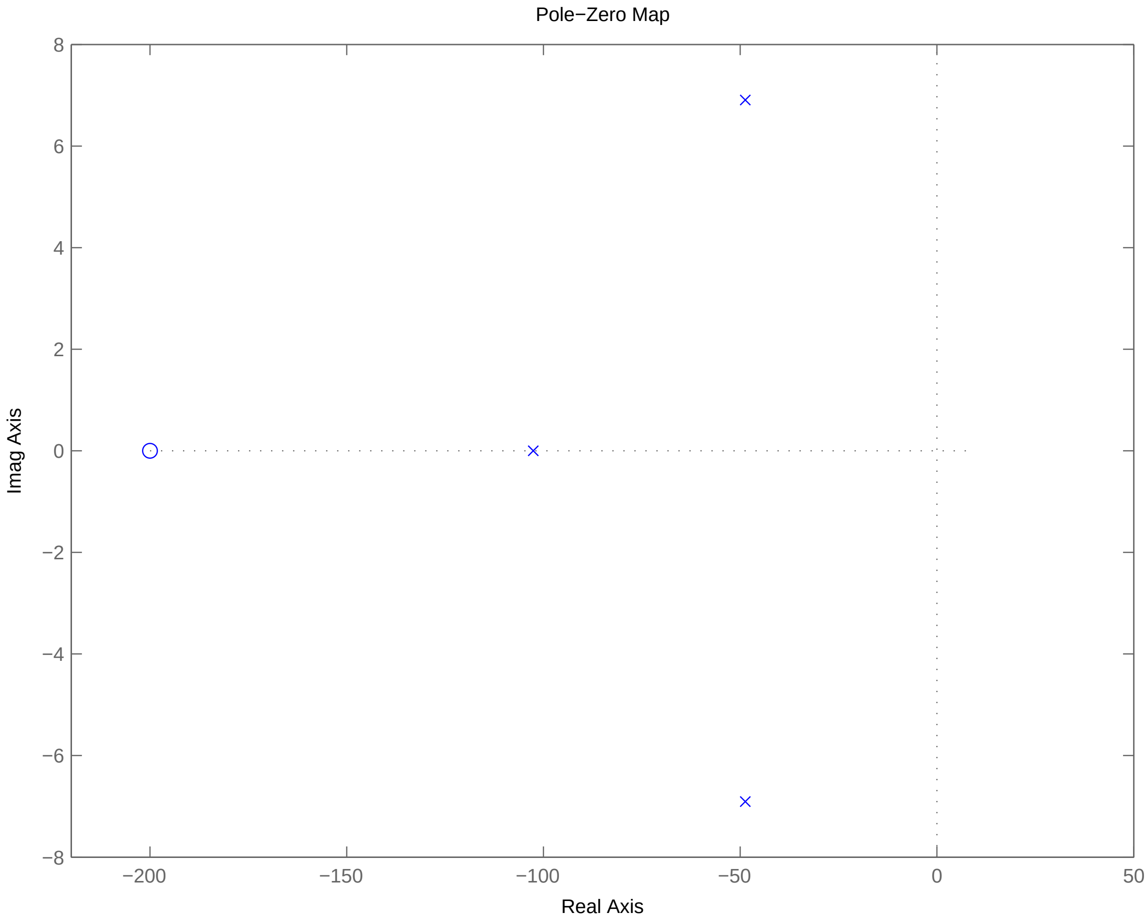

Figure 5-4: Pole-zero plot with lead compensator in the feedback path. Placing the compensator in the feedback path moves the zero to −200 rad/s, the location of the open loop compensator pole. With the zero at this frequency, the dynamics are dominated by the low frequency poles.

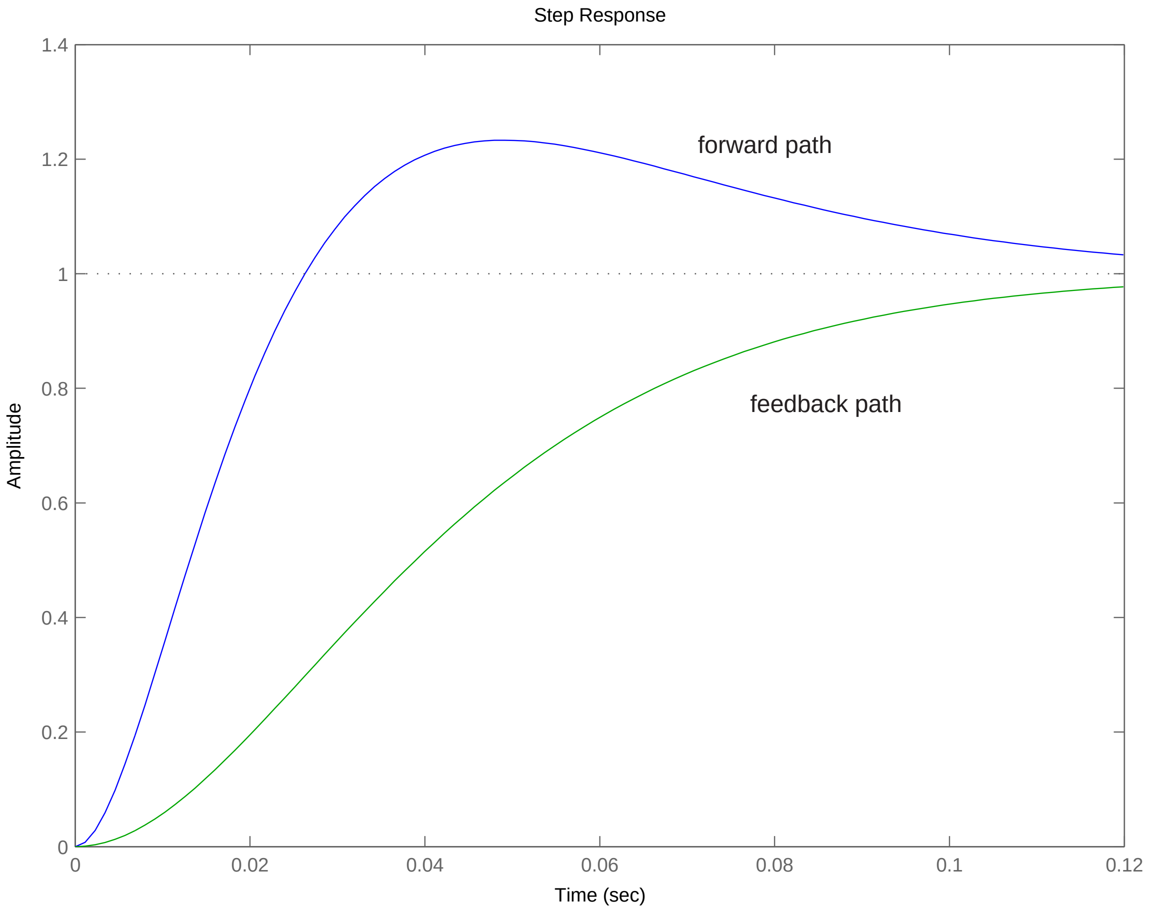

Figure 5-5: Step response of closed loop system with compensator in the feedback path. The step response with the compensator in the forward path is overlayed for comparison. The rise time is faster with the compensator in the forward path but has overshoot. Settling time is about the same for both.

Figure 5-6: Hardware for maglev demo.

inside of the box contains the power supplies, linear amplifier, a storage area for extra parts, and a connector strip. Appendix B details the design layout for the box. Also, see Appendix E for a list of vendors and parts. For the 28 V supply we use a switching supply to accommodate the higher current levels. The switching supply has lower power dissipation than an equivalent linear supply. For the ±15 V, a linear supply is sufficient; currents are on the order of 15 mA so even with static loss, power consumption is not significant.

In the front of the box are two receptacles that connect to the position sensor and inductor coil - they are of different sizes so the connections are unique. The rear of the box has a power cord that plugs into a 120 VAC wall socket. In addition, there are two BNC connections, one to the dSPACE box V_{in1}, with the sensor signal and one from the box V_{out1}, with the command to the amplifier.

One issue that needs attention pertaining to practical implementation is the layout

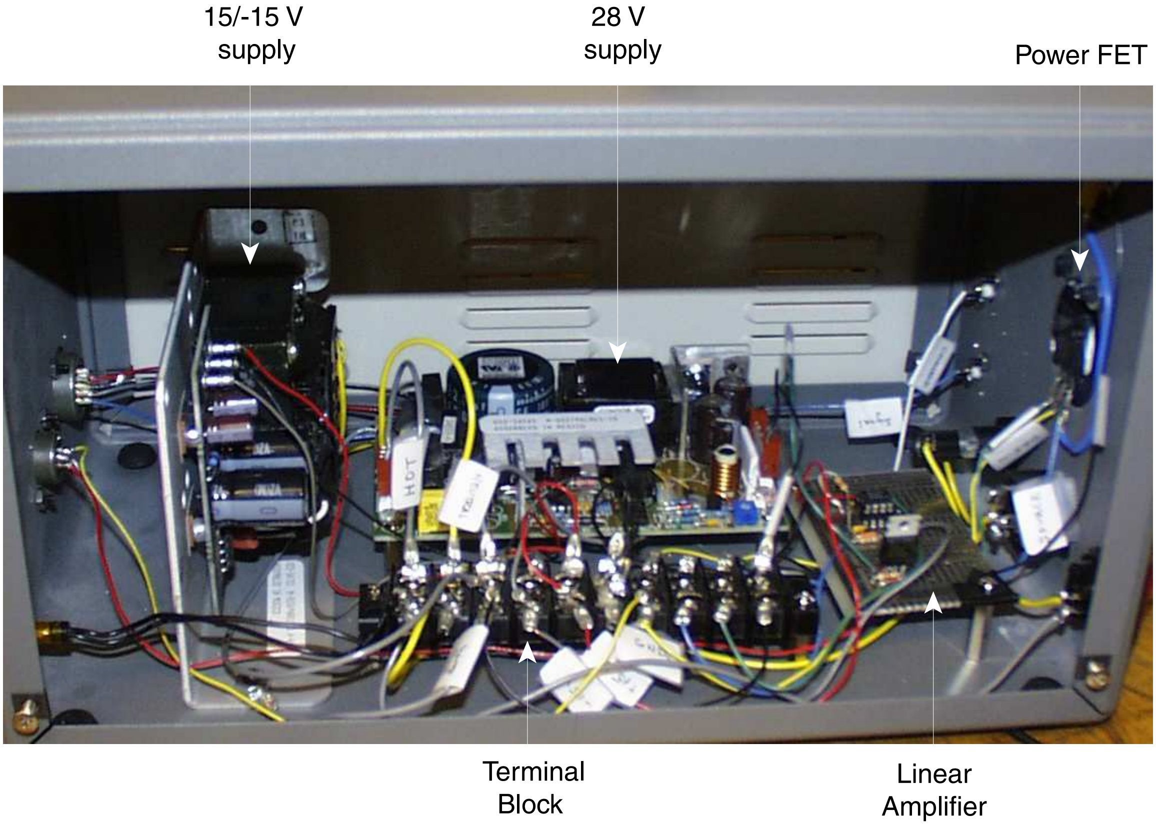

Figure 5-7: Interior of power supply and circuitry box.

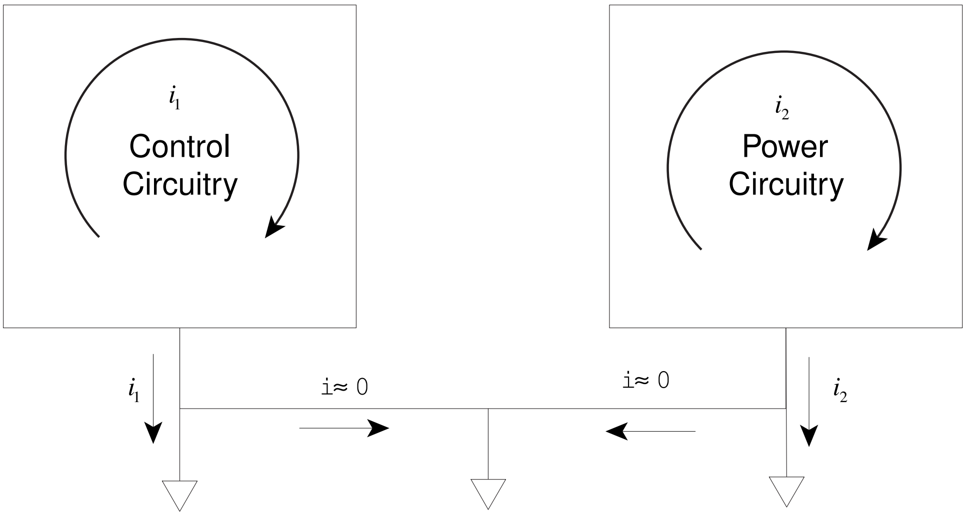

Figure 5-8: Separation of control and power circuitry.

of the linear amplifier. The position sensor circuitry is on the physical structure itself and only the linear amplifier is off board. Therefore, we need not consider the interactions between the position sensor circuitry and amplifier. The amplifier circuitry can be thought of in two parts: the control and power circuitry. Essentially the concern is interference from high gains and currents in the power circuitry. The power circuitry is the path through which the actuator current flows, currents on the order of 250-750 mA steady state. There is also a large voltage gain from the gate to drain of the power FET.

To deal with this, we want to physically separate these two portions of the circuit, providing a local ground for each, and at one and only one point, connect those local grounds. The idea is for currents to flow within each subsection and return through its own local ground; the two circuits are virtually isolated. There is one earth ground and that reference comes from the wall socket. We pick one point to bring in earth ground and that is where we also tie together the two local grounds. This minimizes flow of currents between circuits and the resulting interference. The scenario is depicted in Figure 5-8. In the same vein, an extra ground wire was allocated from the transresistance amplifier: one ground wire is for the return current while the other serves as the reference for the position voltage measurement.

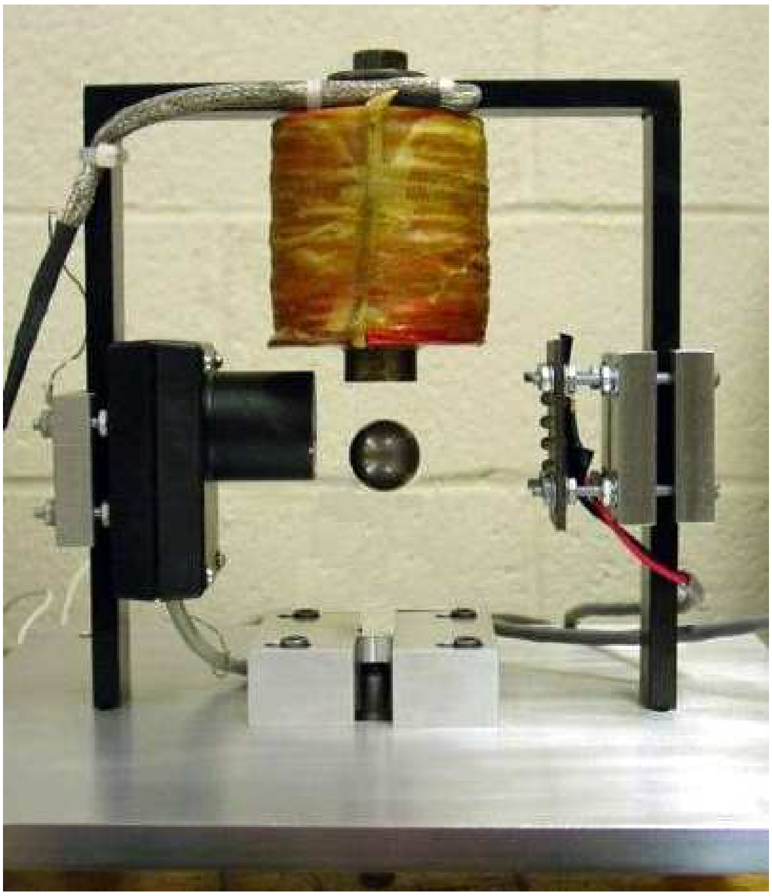

Figure 5-9: Photograph of ball in suspension.

5.4 Bandwidth Considerations

At a bandwidth of 10 Hz, the suspension system clearly works. Figures 5-9 and 5-10 are photographs of the ball successfully suspended. We measure the loop transmission using a Dynamic Signal Analyzer tool developed by Katie Lilienkamp [5] (see Appendix C for usage). Comparing Figure 5-11 to Figure 4-10 (page 65), we see the experimental loop transmission closely follows the predicted. The actual loop crossover is about 8 Hz, just short of the 10 Hz desired crossover. The lower magnitude is most likely due to the eddy currents in the core as detailed in Chapter 3, Section 3.2. The phase plot illustrates the characteristic phase bump from the lead compensator but again, there is additional negative phase due to the eddy currents.

At low frequencies, the magnitude levels off because the plant poles are not di-

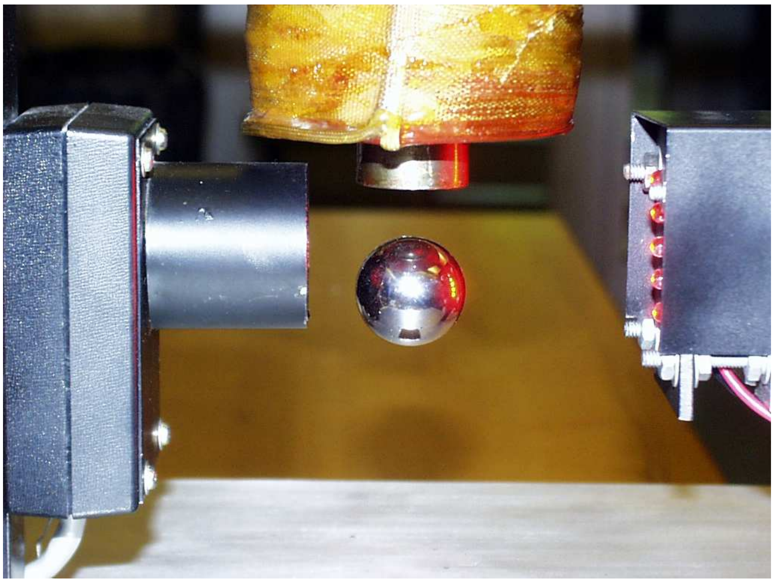

Figure 5-10: Photograph of ball in suspension.

rectly aligned at the origin. A perfect nonlinear transformation would put the poles at the origin yielding a larger gain at DC. From Figure 5-12 we see the magnitude is flat up to 1 Hz and has a resonant peak around 3 Hz, exhibiting a mechanical "spring" behavior. Thereafter, the slope falls off at approximately -20 dB as predicted, exhibiting "mass" behavior. This suggests the poles are complex, aligning on the jw axis, which explains the resonance and corresponding drop off in phase, as well as the lower DC gain. With more tweaking of the nonlinear transformation, the plant transfer function would more closely resemble the predicted function. Beyond the resonance, the experimental magnitude has the same slope as the predicted, but is offset by a factor. This lower magnitude is most likely explained by eddy currents in the core where there is a fall off in actuator force with increasing frequency.

However, we would like to explore the advantages, limitations, and tradeoffs of having a higher bandwidth. Based on the method of lead compensator design explored in Chapter 2, we design the loop bandwidth to whatever specification is required. Table 5.1 shows the parameters needed for loop crossover frequencies at 10 Hz, 30 Hz, and 100 Hz.

In the real world, systems are low pass in nature and gain drops off at higher

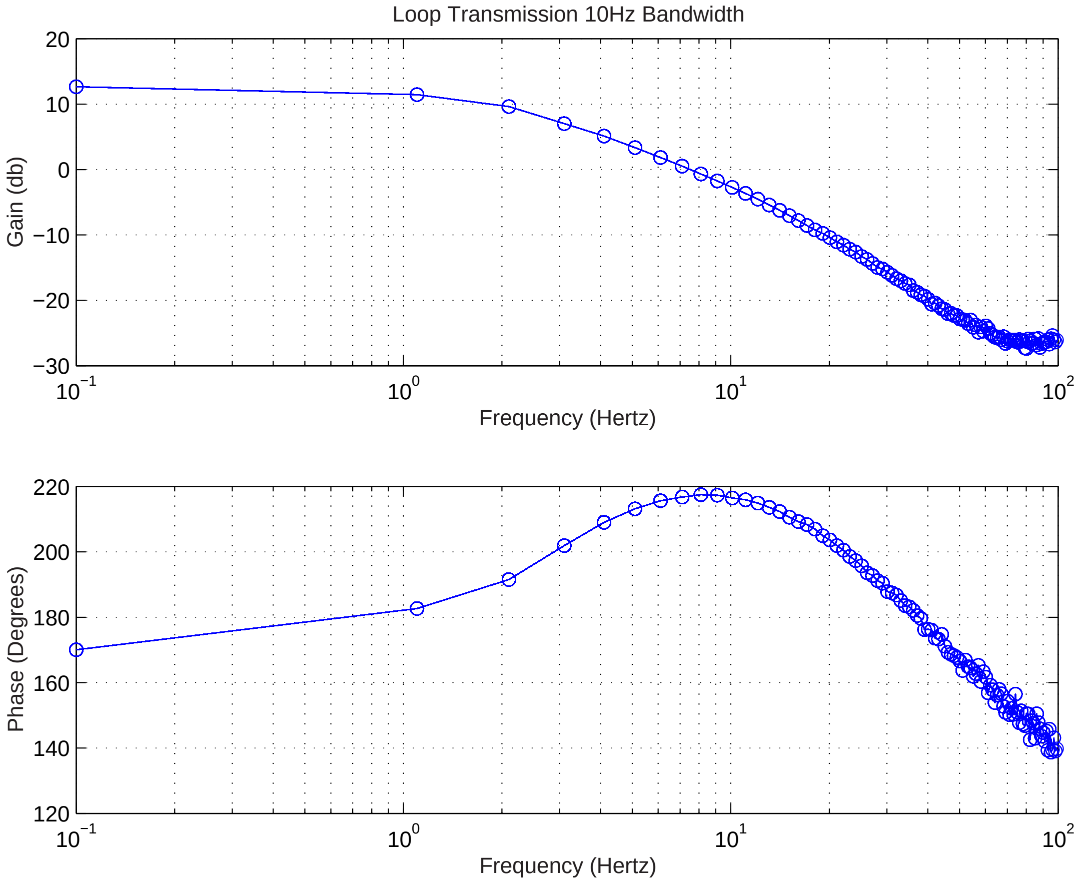

Figure 5-11: Experimental loop transmission designed for 10 Hz bandwidth. Actual crossover is at about 8 Hz. The DSA tool used to generate this plot actually plots the negative loop transmission, which explains the phase offset by 180°.

frequencies due to parasitics. Plus, higher order dynamics come into play. We do not model these in the plant transfer function but they are there and place one limit on the bandwidth of the system. If we design for bandwidths in the neighborhood of the unmodeled dynamics, the added phase due to those parasitics could cause the system to go unstable.

Another constraint on bandwidth is noise. A lead compensator has a gain amplification of ten (with $\alpha = 10$) at high frequencies relative to low frequencies . That means the compensator amplifies any high frequency noise coming from the position sensor before comparing it to the reference. The error signal could potentially be swamped by noise; the signal is then amplified by the gain. With large enough gains,

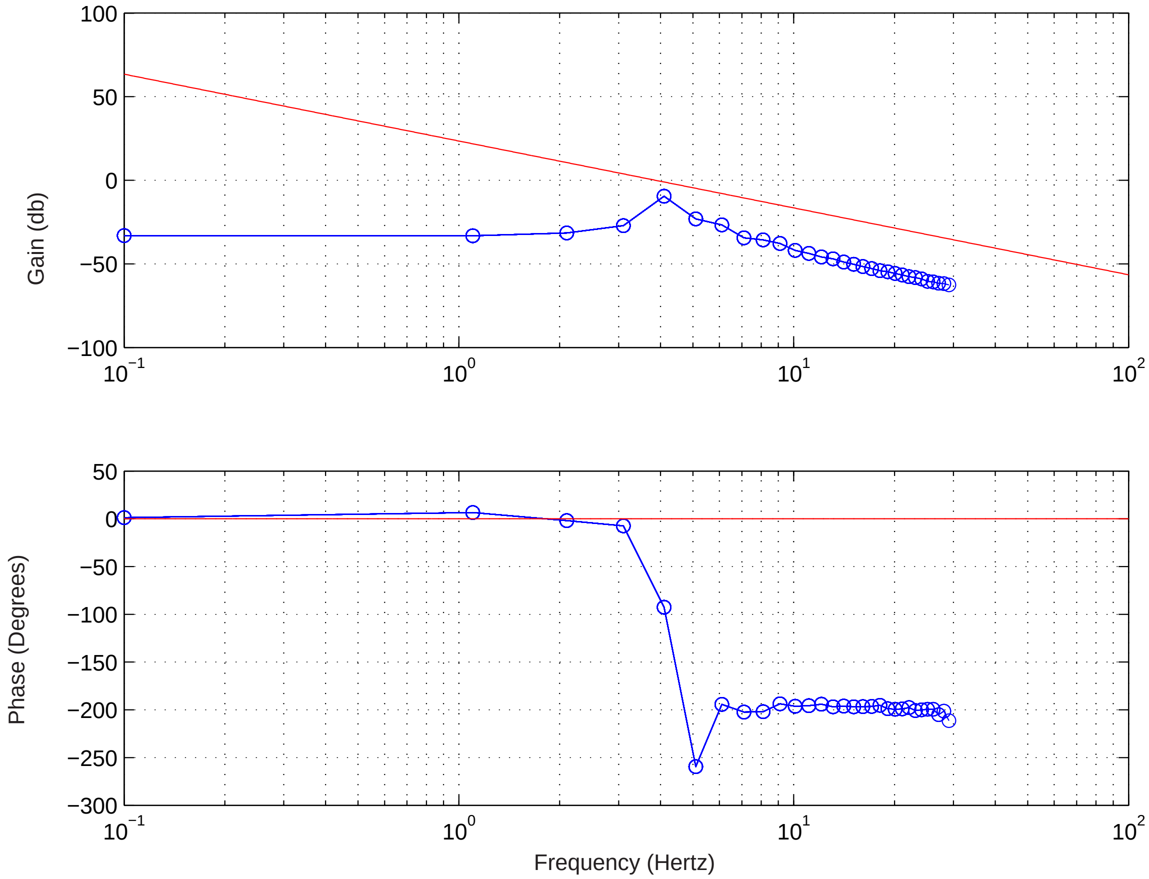

Figure 5-12: Experimental plant transfer function. The circles with an interpolated line represent data points, and the single solid line is the theoretical transfer function. The DSA tool used to generate the plot actually plots the negative of the plant transfer function, which is why the phase is offset by 180°.

this becomes a problem. One solution would be to add a couple of higher frequency poles to kill off the noise. In a future implementation, this would be a good addition. Considering the poles would have to be placed well above the original compensator pole, the crossover frequency would obviously have to be well below these poles and that places an additional constraint on the bandwidth.

In light of these barriers, why would we want more bandwidth? The step responses in Figure 5-13 show the rise time for three different bandwidth designs. The rise time is faster with higher bandwidths. This is desirable in some systems but it is not as important for this system. Risking instability for faster rise time is not a good tradeoff to make here. However, the real benefit comes with disturbance rejection

f_c	ω_c	K	τ
10 Hz	63 rad/s	83	5 ms
30 Hz	126 rad/s	333	2.5 ms
100 Hz	628 rad/s	8319	0.5 ms

Table 5.1: Parameters for designing a controller at different bandwidths at 10Hz, 30Hz, and 100Hz.

and that is important. Essentially, the higher gain and bandwidth means the system reacts faster to disturbances. The rise time and disturbance rejection go hand in hand because both are due to a higher gain.

In an analysis of the position to disturbance force transfer function, we see the rejection improves with larger gains.

$$\frac{X(s)}{F_d(s)} = \frac{ms^2(\tau s + 1)}{ms^2 + K(\alpha\tau s + 1)}$$

By the final value theorem, $x(\infty)$ due to a unit step in disturbance is

$$x(\infty) = \frac{1}{K}. \tag{5.1}$$

The gain term appears in the denominator so for larger gains, the output due to disturbance force becomes a smaller fraction. Intuitively, this makes sense because the error signal is multiplied by the gain but the disturbance is not. Therefore, the output due to the reference is large in comparison to that due to the disturbance, and this difference grows with larger gains. Mechanically, a larger K value is equivalent to making the system stiffer. Figure 5-14 shows two traces, 10 Hz and 30 Hz crossover designs, of the output due to a step in disturbance force. The disturbance force contributes a much larger portion to the output in the 10 Hz bandwidth design as shown by the larger step in response. By inspection, the 30 Hz design has about 4 times better rejection, which verifies (5.1) with $K = 83$ and $K = 333$ for the 10 Hz and 30 Hz bandwidth designs respectively.

Therefore, we win in terms of better rejection of disturbances at higher bandwidths, but at the risk of unmodeled characteristics causing problems. The lesson

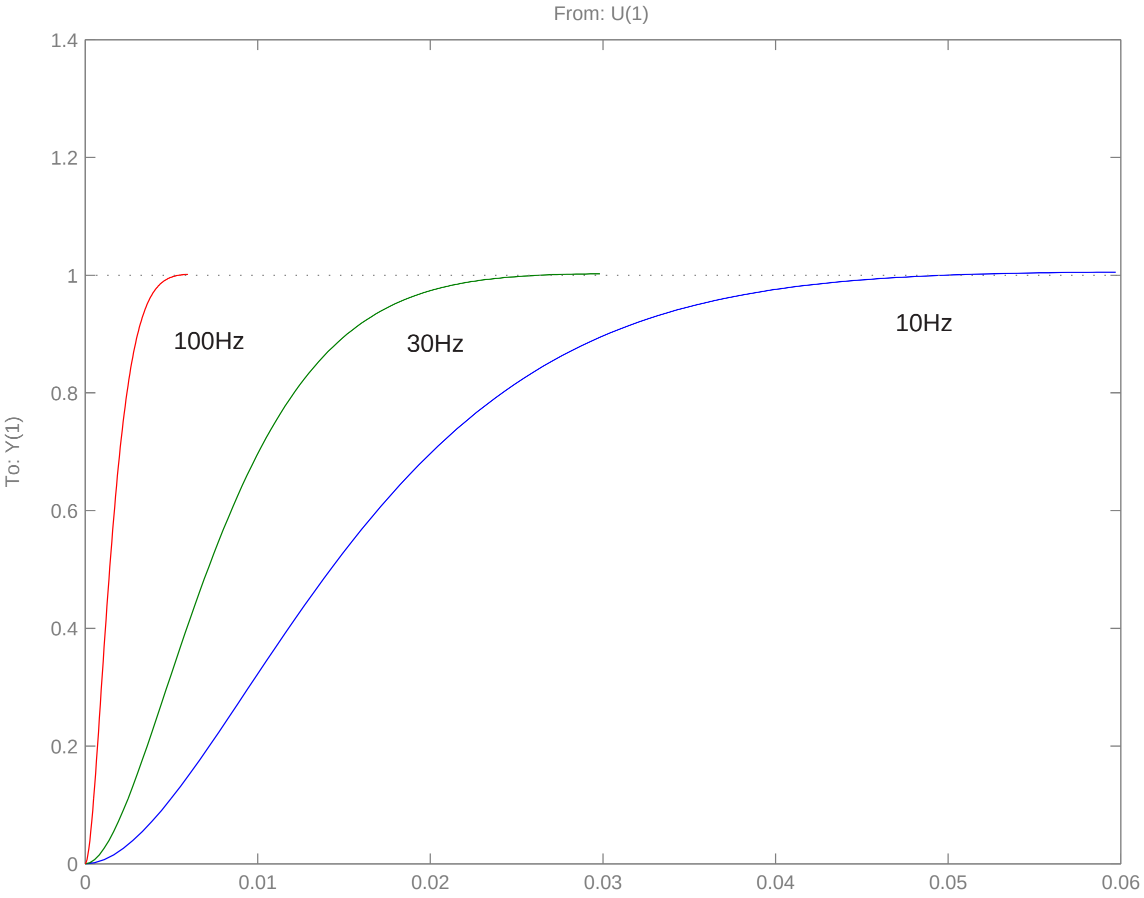

Figure 5-13: Theoretical step responses for 10, 30, and 100 Hz bandwidth designs.

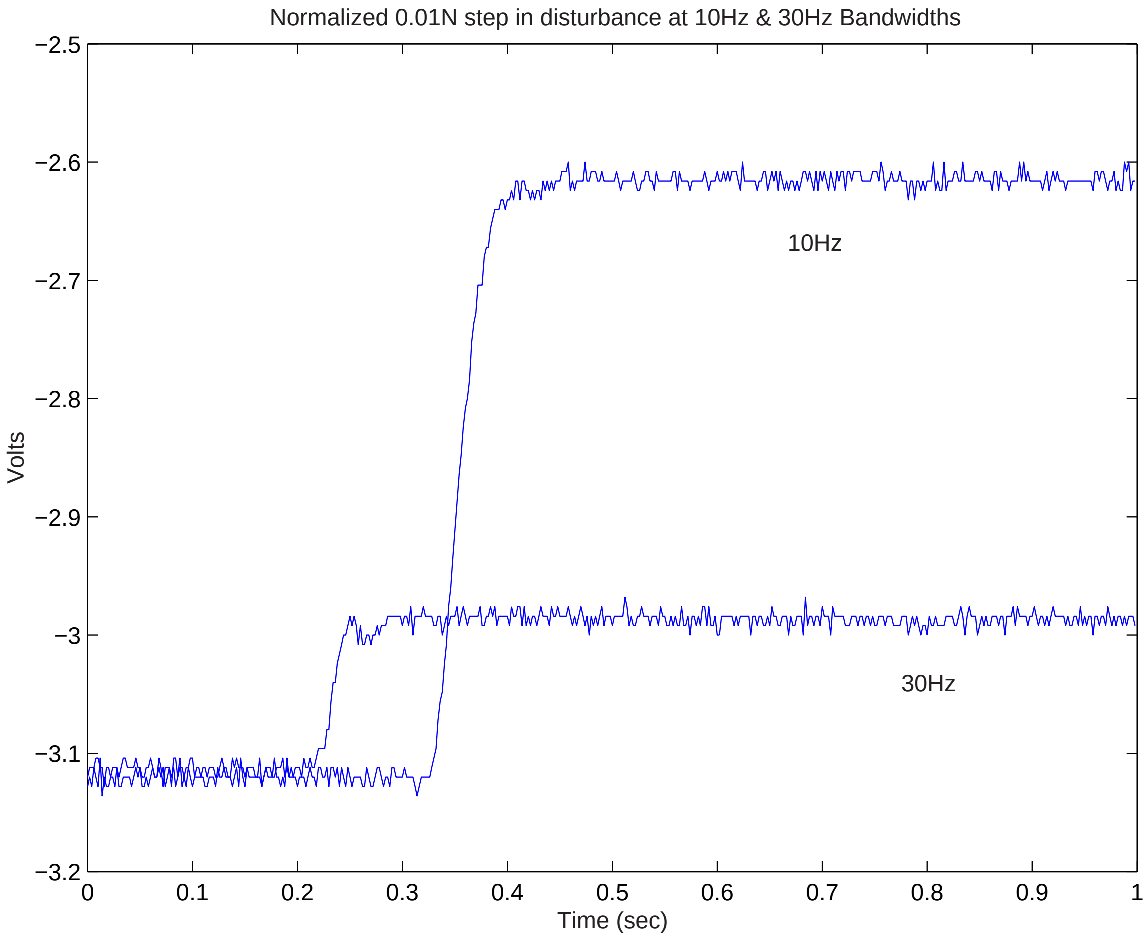

Figure 5-14: Experimental step responses to a 0.01 N disturbance force at a 10 mm air gap. The higher bandwidth 30 Hz crossover signal shows better disturbance rejection.

here is never to design for more bandwidth than you need.

5.5 Air Gap Variations

The main reason for using feedback linearization is for the ability to operate over a larger range of air gaps. For systems where there are large deviations, this is highly desirable. Figure 5-15 shows the step response at 4 different air gaps: 18 mm, 15 mm, 11 mm, and 7 mm. The experiment was set up with 1 mm step inputs drawing the ball towards the actuator, thereby closing the air gap. The trace represents the actual uncompensated position as measured by the transresistance amplifier. Figure 5-16 shows the coil current as measured by the sense resistor. The shape of the step response is uniform at the different air gaps, illustrating the effectiveness of feedback linearization to extend operation to a wider range.

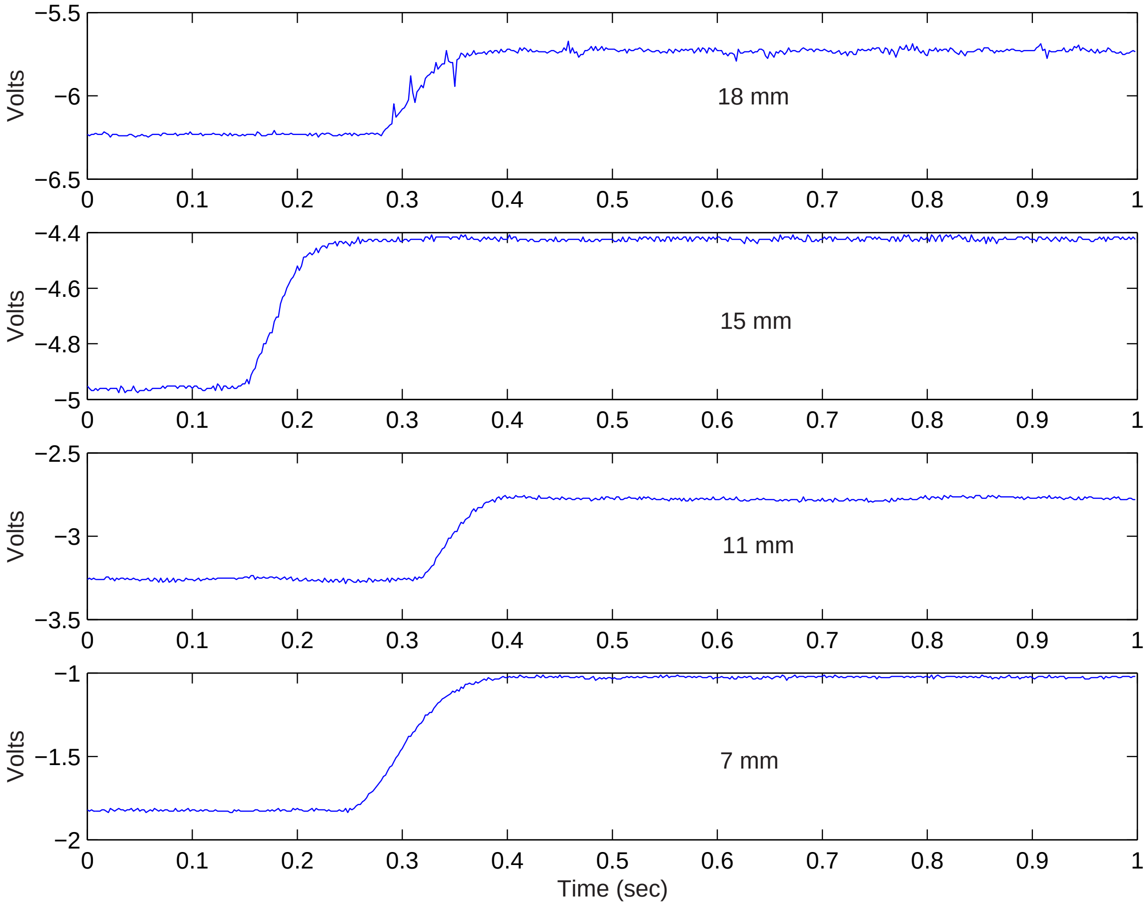

Figure 5-15: Position responses (voltage measurement from position sensor) to a 1 mm step at air gaps 18 mm, 15 mm, 11 mm, and 7 mm.

5.6 Light Source Dependency

We noticed some undesired behavior associated with the light source, the first being lateral oscillations of the ball position. There is a locus of points where the photodiode array will sense the same amount of light because the ball is spherical: the light blocked by the ball is a circular area where more light pass through on the sides than over the top of the ball. If the suspended object were a cylinder or cube, where its

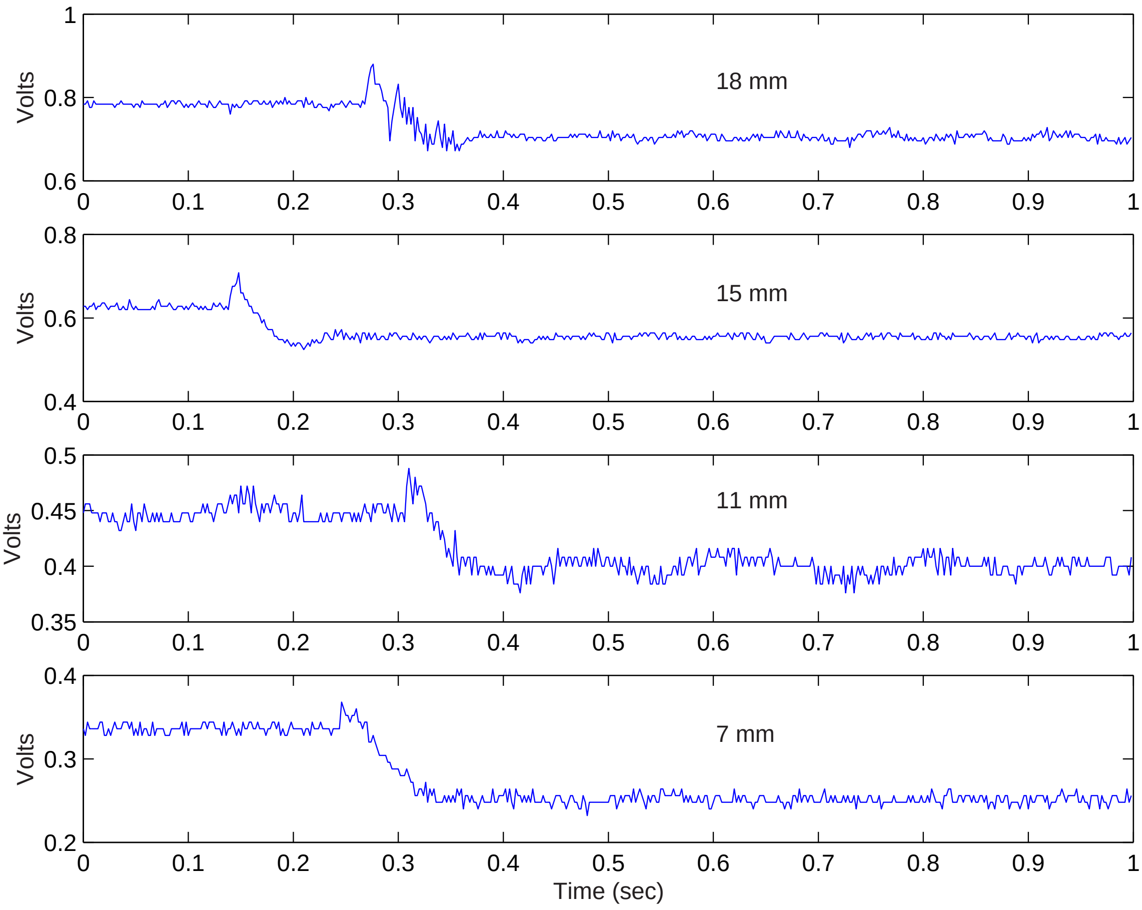

Figure 5-16: Coil current, as measured by the sense resistor, with a 1 mm step input at air gaps 18 mm, 15 mm, 11 mm, and 7 mm.

top edge is a straight line, this effect would be less noticeable. The light sensed by the photodiode array would be more uniform with position.

Furthermore, the moment of inertia of a sphere is symmetrical in all six degrees of freedom. We hypothesized that a column-shaped object, with a larger moment of inertia in the vertical axis, would have better stability along that axis. We glued a ball onto a hollow pipe to use as the suspension object. Figure 5-17 shows a photo of this experiment. However, the vertical stability did not show marked improvement. One reason could be in the construction of the object: the asymmetry in mass due to the glue distribution is enough to cause the object to swing back and forth.

Finally, the position measurement has a first order dependency on the intensity of the light source. The position sensor is calibrated to a particular light intensity

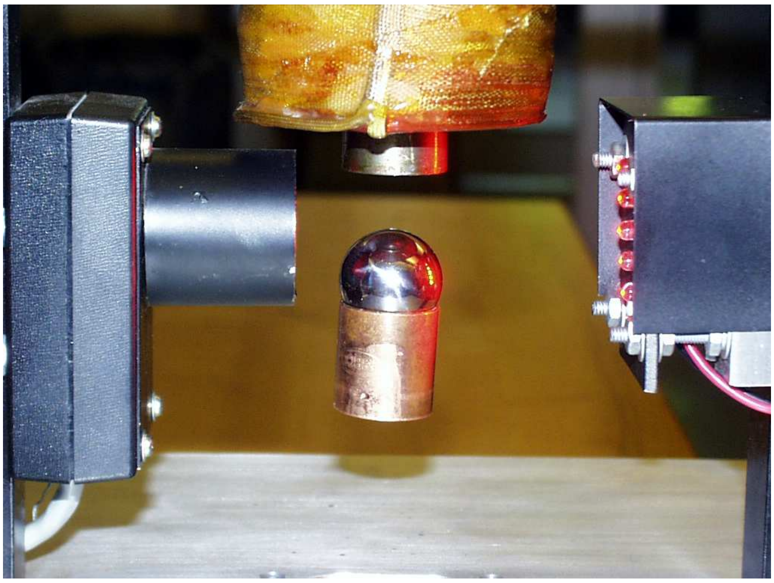

Figure 5-17: Photograph of ball glued to column in suspension.

and that function would no longer be valid with large deviations. Intensity variations occur with changes in the power supply voltage. Recall the light source circuit: the amount of current flowing through the light-emitting diodes is directly dependent on the power supply voltage. Tolerances in the power supply would cause position measurement errors. A better position sensor would base its measurement on the location of illumination rather than the intensity of the light source.

Chapter 6

Conclusions

6.1 Summary

This thesis presented the design and implementation of a magnetic suspension. The single-axis suspension system is composed of a position sensor, steel ball, magnetic coil, linear amplifier, and controller. This classroom demo is an example of a classic nonlinear controls problem, its development illustrating modeling, dynamics, and control. We demonstrated the effectiveness of using feedback linearization as a means of nonlinear control independent of operating point. This is particularly important in systems where large deviations are expected. However, the system is highly sensitive to modeling errors. Prior implementations used a switching amplifier; however, we found a linear amplifier to be sufficient and appropriate because it avoids the noise generation problems of switched amplifiers. Furthermore, an improvement was made by using super bright LEDs. The intense, directed light allowed for more accurate position measurements.

6.2 Suggested Further Work

As outlined in previous research [11], inconsistencies in the light source cause problems in the nonlinear compensation. Low frequency noise due to a drifty transresistance amplifier and stray ambient light is likely the main problem. The use of synchronous modulation is a possible solution. As an area for future work, the modulation could be roughly implemented as follows: the light source is switched on and off at a high frequency and then synchronous detection is used to sense light only at the switched frequency, rejecting ambient and other low frequency offsets. When the light source is switched, the signal is modulated up in the spectrum. The detector receives this modulated signal along with low frequency noise. The signal along with the noise is modulated again at the same frequency so that a scaled copy of the desired signal is centered at its original frequency, while the low frequency noise has been modulated up. Passing this through a low pass filter gives the desired information. The switched frequency has to be fast enough to avoid overlapping with the low frequency noise and to allow sufficiently high control bandwidth.

In addition, it would be desirable to remove the position sensor's dependency on absolute intensity as mentioned in Chapter 5. The luminosity of the light source is dependent on the supply voltage to first order; therefore, slight deviations in the supply voltages effect the calibration of the position sensor. An alternative would be a sensor that bases position measurement on location of light rather than its intensity.

Finally, real-world systems need to be robust to modeling errors and process variations. One problem with feedback linearization is that it is highly dependent on an accurate model and predictable dynamics. Further work in this area would of valuable interest for nonlinear controls.

Appendix A

Users Guide

One design goal is to make this demo as simple and intuitive as possible from a user's perspective. The following provides instructions on how to get the suspension system up and running. The "box" from hereon refers to the box containing the power supplies, circuits, etc.

1. Connect the ribbon cable from the dSPACE board to the laptop. Make sure the dongle is connected to the parallel port of the laptop. dSPACE will not run without the dongle.

2. Connect BNC cables to the dSPACE input/output box with the corresponding receptacles in the back of the box.

3. Connect the cables from the coil, light source, and light sensor to the front of the box. Plug the power cord into wall socket.

4. Start Matlab and Simulink. Open the maglev.mdl model and do a build (Ctrl+B). The build should be done in the same directory as the maglev.mdl file.

Push the power button on the back of the box when the demo is ready to run. Suspend the ball by slowly putting it between the light source and sensor, bringing it up from the bottom.

Appendix B

Box Layout

Below is the physical layout of the power supply and circuitry box. We tried to make the layout efficient and functional. Aside from the heat sink on the back, only the necessary connectors are exposed. The storage container built into the box is for extra parts. In the back of the box are the BNC connections to the dSPACE I/O box. The labels for the BNC connections correspond to the labels on the I/O box (i.e. hook $\mathrm{V_{in1}}$ to $\mathrm{V_{in1}}$).

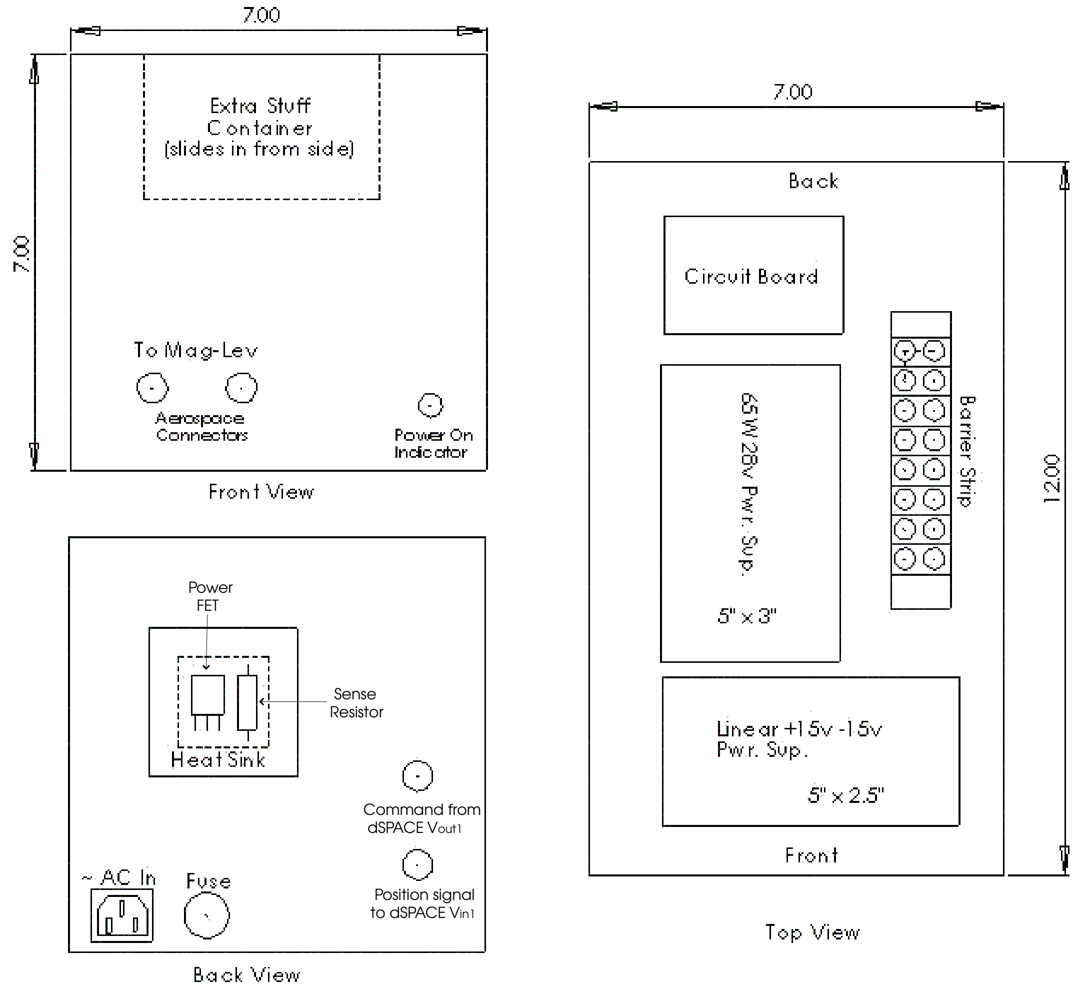

Figure B-1: Design layout of power supply and circuitry box. Drawing courtesy of Danny Hilton.

Appendix C

Simulink Models

The following Simulink models were used in testing the suspension system. The first model is used to suspend the ball. The second, uses the Dynamic Signal Analyzer tool developed by Katie Lilienkamp to find the loop transmission frequency analysis. The "SineOut" signal is a sine wave that drives the system over a range of frequencies specified by running the `dsa_1102` script. The "channel1" and "channel2" inputs are the loop transmission input and output points. In this case, we break the loop at the error signal and the compensated position signal. See [5] for more details on the Dynamic Signal Analyzer tool.

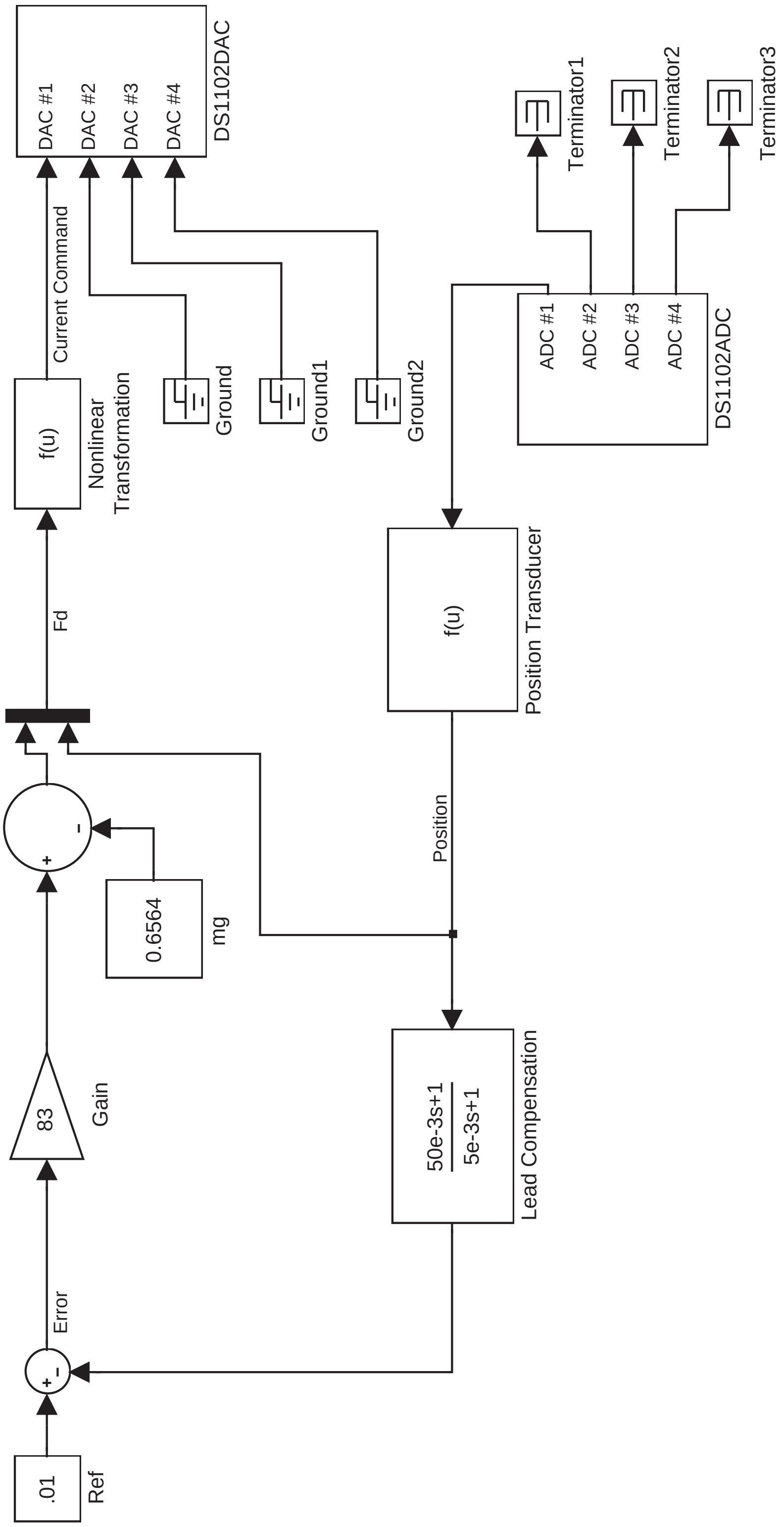

Figure C-1: Simulink model for the magnetic suspension system.

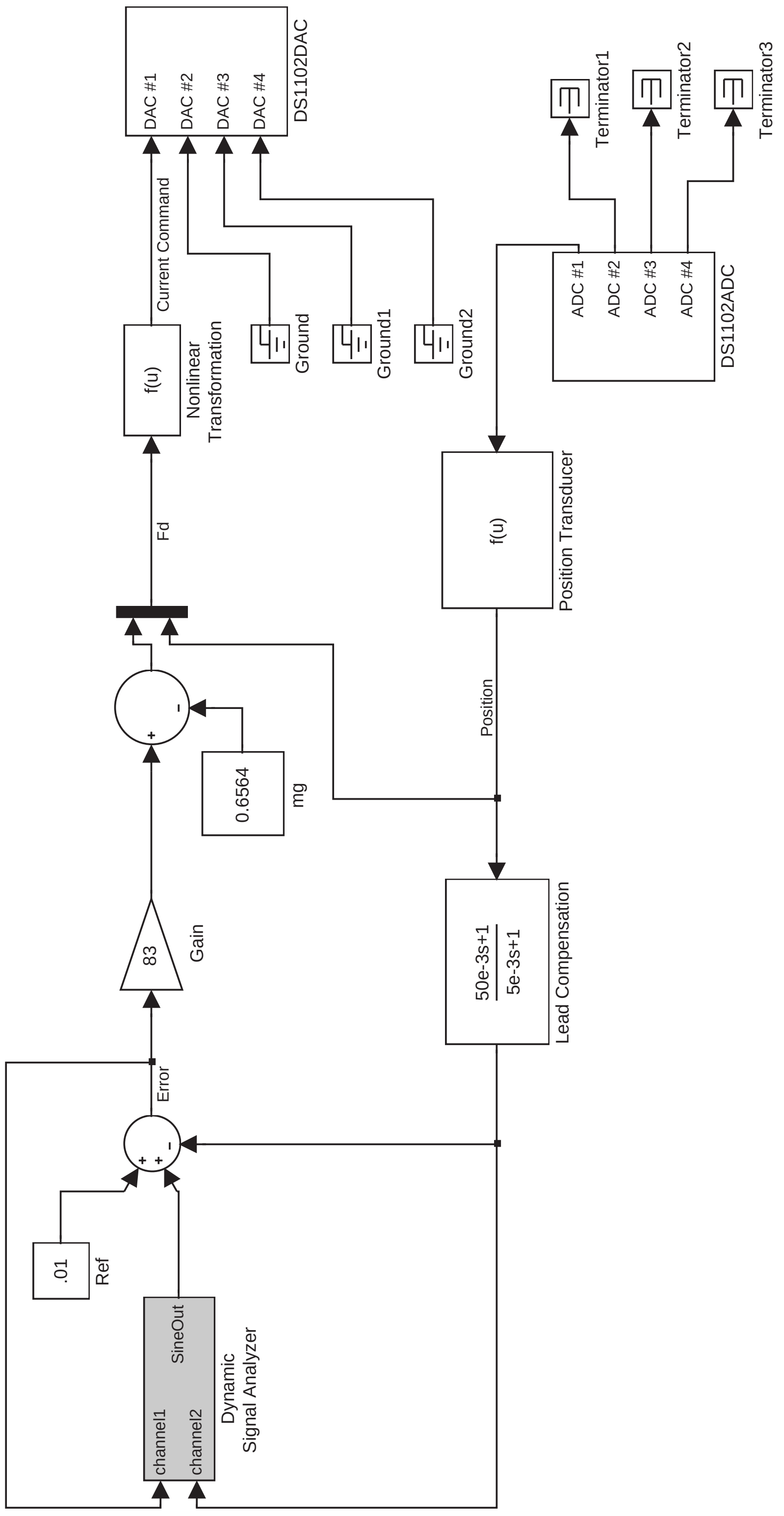

Figure C-2: Simulink model for determining loop transmission frequency analysis.

Appendix D

Matlab Code

D.1 Base Code

This is the base code for `family_force_final.m`, `x0_mean_final.m` and `C_constant_final.m` . . . all of those files should start with this code.

```
clear all;
hold on;
%load data and use best
temp = -1; for count=1:11;
   temp = temp + 1;
   name = ([num2str(count), 'mm']); %%name file to import
   %%files are named by the gap length in mm so we just iterate
   %%through them all

   load(name);
   lgth = 24;    %% number of data points
   first = 1+ lgth*(temp);
   last = 24 + lgth*(temp);

   i= trace_y(1,1:49);  %%load current and force data points
   f = trace_y(2,1:49);  %% 'trace_y' is the var loaded from file

   f1 = f(1:24);%%1st part of curve - increasing in value
   %%2nd part of curve - flipped so it is also increasing in value
   f2 = fliplr(f(26:49));
   %f3 = f(101:151)        %%other points you can look at
   %f4 = fliplr(f(151:201));

   xt = i(1:24);  %%%current is on the x-axis
```

```
   fmean = mean([f1;f2]);  %%take the average of the 2 curves
   Xaverage(first: last) = xt; %%stores average of all the curves
   %%[i.e. the points in each file added onto the vector
   Yaverage(first: last) = fmean;

   %%sorts & calculates the interpolated values of all the curves
   A =[xt;fmean]';
   A =sortrows(A, 1);%makes sure pts are monotonically increasing
   %%important for interp1 function
   ft = 1+ 10001*temp; %%number of points in interpolated function
   lt = 10001 + 10001*temp;

   xx(ft:lt) =0:0.0001:1; %%first column is the current
   yy(ft:lt) = interp1(A(:,1), A(:,2), xx(ft:lt));
                          %%2nd column is the force, interpolated
   x(ft:lt) = count*ones(1,10001);
                          %%3rd column formed by the air gap value
end
```

D.2 Family of Force Curves

File: `family_force_final.m`
Code plots the family of force curves at different air gaps uses a mean average fit for the hysteresis curves

```
%%% include base code here %%%%

plot(Xaverage, Yaverage, 'r.');
title('Family of force curves over different air gaps');
ylabel('Force (N)');
xlabel('Current (A)');
```

D.3 Averaging Hysteresis Curves

File: `x0_mean_final.m`
This script determines the xO constant in the force equation $F = C(i/x + x0)^2$. It uses a mean average fit for the hysteresis curves.

```
%%% include base code here %%%

%fill variables for a plot of current versus position
force = [0.6 0.61; 1.2 1.21; 2 2.01; 3 3.01];
    %%pick out x,i for F=0.6, F=1.2, F=2, F=3

for j=1:4  %%for each force level, plot the current vs. position
   count =1;
   y = [];
   t = [];
   for n=1:lt;
      if ((yy(n) >= force(j, 1)) & (yy(n) <= force(j, 2)))
         y(count) = xx(n);
         t(count) = x(n)+.26;
         %%offset factor in micrometer measurement
         %%(i.e. zero on micrometer is not zero gap)
         count = count +1;
      end
    end

%%%%%%%%%%%%%%%%%%%%%%%%%%%%%%%%%%%%%%%%%%%%%%%%%%%%%%%%%%%%%%%%%%%%%
%use linear best fit to draw family of curves and determine x0

    l = length(t);
    Xmean = sum(t)/l;
    Ymean = sum(y)/l;

    Mxy = sum((t-Xmean).*(y-Ymean));
    Mxx = sum((t-Xmean).^2);
    m = Mxy/Mxx;
    b = Ymean-m*Xmean;
    tlong = (-8:.1:t(l)); %%extend the x-axis because curves
                          %%will intersect at x<0
    Ytheo=m*tlong +b;  %%this is just y=mx+b
   plot(t,y,'r.');  %%plot actual points
   plot(tlong,Ytheo,'b.');  %%overlay with linear best-fit line
   xv0(j) = -b/m;  %%vector of x0 constants at each force level
   %%gtext([num2str(force(j, 1)),'N']);
   %%uncomment this if you want to label each force
```

```
end

x0 = (xv0(1) + xv0(2) + xv0(3) + xv0(4))/4;  %%average x0 constants
title(['Determining finite reluctance offset x0=',num2str(x0/1000),
         'm'])
xlabel('X gap in mm');
ylabel('Current (A)');
```

D.4 Determining the C constant

File: `C_constant_final.m`
Code determines the C constant in the force equation $F = C(i/x)^2$ - uses a mean average fit for the hysteresis curves.

```
%%% include base code here %%%

%fill variables for a plot of current versus position
force = [2.8 2.802];  %%picks out values for a fixed F=2.8
   count =1;
   y = [];
   t = [];
   for n=1:lt;
      if ((yy(n) >= force(1)) & (yy(n) <= force(2)))
%%must give range because number in data are carried out a
%%number of decimal places; yy(n)=force will return false otherwise
         y(count) = xx(n);   %%current
         t(count) = (x(n)+.26)./1000;
         %%offset factor in micrometer measurement
         %%(i.e. zero on micrometer is not zero gap)
         count = count +1;
      end
    end

%%%%%%%%%%%%%%%%%%%%%%%%%%%%%%%%%%%%%%%%%%%%%%%%%%%%%%%%%%%%%%%%%%
%%calculation of C value
c = (((t+.00364).^2)./(y.^2)).*force(1);  %%% c = f*x^2/i^2;

%%plots a linear best-fit based on c values
l = length(y);
Xmean = sum(y)/l;
Ymean = sum(c)/l;

Mxy = sum((y-Xmean).*(c-Ymean));
Mxx = sum((y-Xmean).^2);
m = Mxy/Mxx;
b = Ymean-m*Xmean;
Ytheo=m*y +b;
plot(y,c, 'r.',y,Ytheo);

title(['C values at f=2.8N Cave=', num2str(mean(c)*10000),
         'x 10^-4 NA^2/m^2']);
xlabel('X gap in cm');
ylabel('C constant');
```

D.5 Voltage and Position Calibration

File: `sensor_final.m`
This script generates a plot of voltage vs. position data points. It interpolates with a linear best-fit.

```
%input data points of voltage measurements & form position vector
v=-1*[.26 .49 .70 .99 1.36 1.73 2.10 2.51 2.97 3.44 3.91 4.4 4.87
        5.33 5.78 6.25 6.70 7.16 7.52];
xg = [0:1:18];
%normalize to meter units and add on offset to micrometer reading
xg = 0.001*(xg+1.44);

%linear best-fit
n = length(xg);
Xmean = sum(xg)/n;
Ymean = sum(v)/n;

Mxy = sum((xg-Xmean).*(v-Ymean));
Mxx = sum((xg-Xmean).^2);
m = Mxy/Mxx;
b = Ymean-m*Xmean;
Ytheo=m*xg +b;

%plot best fit y = mx + b
plot(xg, v, 'mo', xg, Ytheo);
title(['y = ', num2str(m), 'x + ', num2str(b)]);
xlabel('Position X (m)');
ylabel('Voltage V (volts)');
```

D.6 Comparing Empirical Transformation to Actual Data

File: `curve_fit_final.m`
Plots current vs. force data points and then overlays it with a curve based on the empirical formula. This aids in empirically determining the transformation equation allowing comparison to see how well the equation fits.

```
%load the 10mm air gap file
load('10mm');
x = .01;

%store data points in variables
i= trace_y(1,1:49);
f = trace_y(2,1:49);

%determined values from data - see chapter 3 on force measurement
C = -.0032133*x + .00065236;
x0 = .0025;

%things start to fall apart with x < .002m - equation does not hold
y = (x + x0)*sqrt(f/C) + (0.0195*exp((x-.002)/.006) -
        3.5*(x-0.007))*f + 450*(x-.0014)^2*f.^2;

plot(f, i, 'r.', f, y);
title('Force vs Current gap = 10mm');
ylabel('Current (A)');
xlabel('Force (N)');
```

Appendix E

Vendors

Amphenol Military/Aerospace Industrial Operations
40-60 Delaware Avenue
Sidney, NY 13838-1395
Telephone — (800) 678-0141
Web address — http://www.amphenol-aerospace.com
Products used:MS3106F-10SL-3S, MS3106F-16S-1S connector plugs, MS3102R-10SL03P, MS3102R-16S-1P receptacles

Bud Industries, Inc.
4605 East 355th Street
Willoughby, Ohio 44094
Telephone — (440) 946-3200
Web address — http://www.budind.com
Product used: 7.25” x 12.25” x 7.75” enclosure

Condor DC Power Supplies Inc.
2311 Statham Pkwy.
Oxnard, CA 93033
Telephone — (805) 486-4565
Web address — http://www.condorpower.com
Products used: ±15 V linear power supply, GLM65-28 28 V switching supply

dSPACE Inc.
28700 Cabot Drive – Suite 1100
Novi, MI 48377
Telephone — (248) 567-1300
Web address — http://www.dspaceinc.com/index.htm
Product used: ControlDesk, DS1102 controller board, expansion box, I/O panel

The MathWorks, Inc.
3 Apple Hill Dr.
Natick, MA 01760-2098
Telephone — (508) 647-7000
Web address — http://www.mathworks.com
Products used: MATLAB, Simulink

Bibliography

[1] J. Eric Corban, Anthony J. Calise, J.V.R. Prasad, Jeong Hur, and Nakwan Kim. Flight evaluation of adaptive high-bandwidth control methods for unmanned helicopters. *AIAA Guidance, Navigation, and Control Conference and Exhibit*, 2002.

[2] H. A. Haus and J.R. Melcher. *Electromagnetic Fields and Energy.* Prentice Hall, 1989.

[3] B. Kadmiry, P. Bergsten, and D. Driankov. Autonomous helicopter control using fuzzy gain scheduling. *Proc. of the IEEE Int. Conf. on Robotic and Automation(ICRA)*, 2001.

[4] A.S. Krupadanam, A.M. Annaswamy, and R.S. Mangoubi. A multivariable adaptive control design with applications to autonomous helicopters. *AIAA Journal of Guidance, Navigation, and Control*, 2002.

[5] K.A. Lilienkamp and D.L. Trumper. *Dynamic Signal Analyzer for dSPACE.* Precision Motion Control Lab, MIT, 77 Mass. Ave; Rm. 35-030.

[6] Toru Namerikawa, Masayhuki Fujita, and Roy S. Smith. H_∞ control attenuating initial state uncertainties and its application to the magnetic suspension system. *Proceedings of the Eight International Symposium on Magnetic Bearings*, 2002.

[7] Zhihua Qu. *Robust Control of Nonlinear Uncertain Systems.* John Wiley and Sons, 1998.

[8] Jean-Jacques E. Slotine and Weiping Li. *Applied Nonlinear Control.* Prentice-Hall, 1991.

[9] D.L. Trumper. *Magnetic Suspension Techniques for Precision Motion Control.* PhD thesis, Massachusetts Institute of Technology, 1990.

[10] D.L. Trumper. Nonlinear compensation techniques for magnetic suspension systems. *NASA Workshop on Aerospace Applications of Magnetic Suspension Technology*, 1990.

[11] D.L. Trumper, J.C. Sanders, T. H. Nguyen, and M.A. Queen. Experimental results in nonlinear compensation of a one-degree-of-freedom magnetic suspension. *International Symposium on Magnetic Suspension Technology*, 1991.

[12] M.C. Weng. *Magnetic Suspension and Vibration Control of Flexible Structures for Non-contact Processing.* PhD thesis, Massachusetts Institute of Technology, 2000.

[13] H.H. Woodson and J.R. Melcher. *Electromechanical Dynamics - Part I.* John Wiley and Sons, 1968.